Anisotropy of the Plastic Deformation and Fracture Processes in a Dynamically Loaded Crystallite

K. P. Zol'nikov, T. Yu. Uvarov, and S. G. Psakh'e

Institute of Strength Physics and Materials Science, Siberian Division, Russian Academy of Sciences,
Tomsk, 634055 Russia

e-mail: uvarov@ispms.tsc.ru

Received October 11, 2000

Abstract—The influence of anisotropic dynamic loading on the character of plastic deformation and fracture processes in a crystallite near the free surface was studied by methods of molecular dynamics. It was established that there are threshold deformation levels determining the opening of a seeding crack (notch) and the subsequent crack stop. The simulation results show that loading in the [100] direction leads to the crack stop due to the formation of a disordered material region at the crack tip. © *2001 MAIK "Nauka/Interperiodica"*.

An important point in the study of dynamics of the plastic deformation and fracture processes in heterogeneous materials is to elucidate the elementary processes involved in the nucleation and growth of dislocations and cracks. On the microscopic (atomic) level, this task is frequently solved by methods of molecular dynamics. For example, Dienes and Paskin [1] simulated the propagation of microcracks in two-dimensional crystal structures and studied dependence of the results of modeling on the type of the interatomic interaction potential, determined the distribution of microstresses at the vertices of microcracks, evaluated the critical values of loading for the crack opening, etc. The simulation was performed for microcracks of various shapes. Based on a quasicontinuum model, Miller *et al.* [2] studied the process of crack nucleation and propagation in the presence of grain boundaries and calculated the coefficient of the critical loading intensity leading to either a brittle fracture of the material or a dislocation emission from the crack vertex. It was pointed out that an important role in description of the dislocation formation at the crack tip belongs to the nonlinearity effects. It should be noted that investigations of this type usually ignore the role of the free surface. However, it was demonstrated [3, 4] that the presence of interfaces (in particular, of the free surface) significantly influences the plastic deformation and fracture processes.

In this context, we have used the method of molecular dynamics to study the behavior of a crystallite possessing free surfaces and containing regions of incommensurate deformation under the dynamic loading conditions. Special attention was paid to determining anisotropy of the sample response, for which purpose a uniaxial tension was simulated along the crystallographic directions [100] and [110]. The sample modeled had the shape of a parallelepiped comprising three

regions, two of which modeled the regions of contact with undeformable inclusions (see Fig. 1, where these regions are painted black). One of these undeformable regions (referred to below as the clamp) moved at a constant velocity, while the other (substrate) was immobile. The other two directions in the crystallite were used to simulate various boundary conditions and free surfaces. Using this model, it is possible to study on a microscopic level the behavior of fragments in composite materials with hard inclusions. The sample stretching velocity was varied in the range from 10 to 100 m/s.

Simulations were performed for a copper crystal containing more than 8000 atoms. The nucleation and propagation of cracks arising under the uniaxial tension conditions were studied in a sample with a seeding crack (notch) on one of the free surfaces (Fig. 1). The notch had the shape of a triangular groove passing across the free crystal face. The interatomic interaction was described
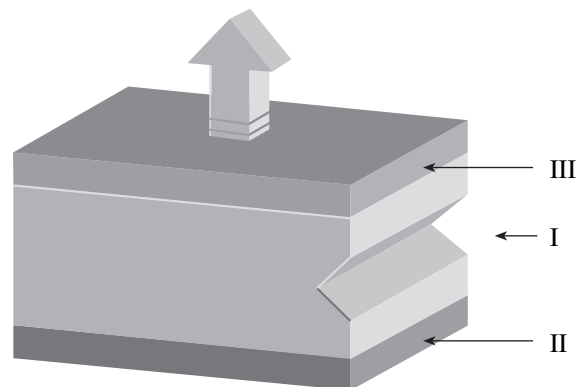

Fig. 1. A diagram illustrating the scheme of sample loading. Regions I, II, and III correspond to the notch, substrate, and clamp, respectively.
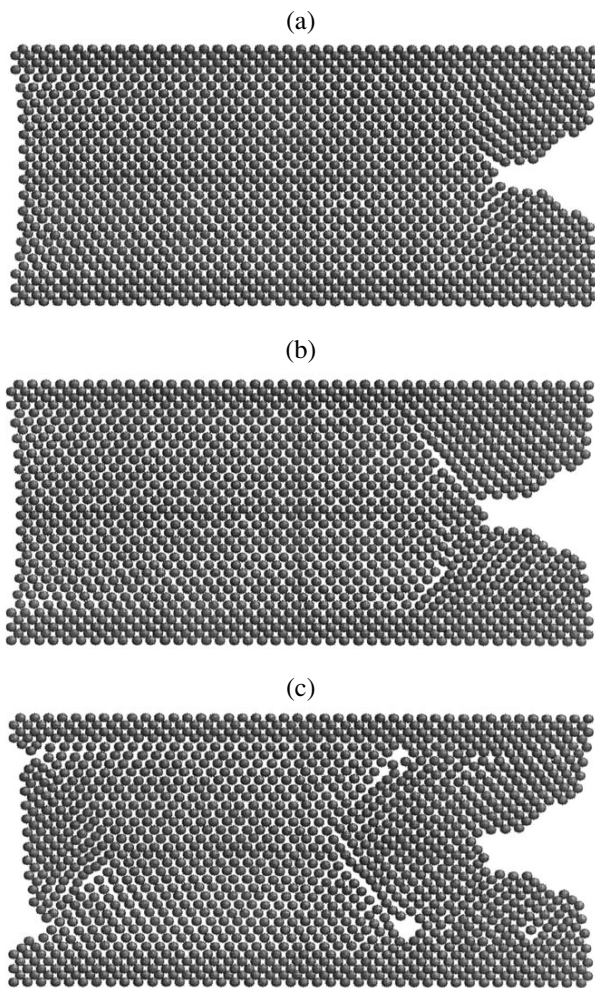
(a)

(b)

(c)

Fig. 2. Evolution of the model crystallite structure on loading in the [110] direction at a velocity of 100 m/s.

using multiparticle potentials calculated within the framework of the embedded atom model [5, 6]. Using these potentials, it is possible to study various structural, mechanical, and energetic properties of both bulk and free surfaces of a material.

Previously [7, 8], we demonstrated that a dynamic tension along the crystallographic direction [100] leads to fragmentation of the crystallite studied. The subsequent analysis showed that the formation of blocks is preceded by the appearance of a vortexlike atomic motion in the boundary regions with incommensurate deformation. The vortex diameter is about ten lattice parameters. Note that it is the vortex motion that accounts for the intense atomic displacements at the free surface. Thus, the sample fragmentation begins in the subsurface region and may proceed either by means of the boundary atoms matching to the structure of a fragment nucleated or by the fragment growth and coalescence. It was established [7, 8] that the fragment misorientation angles may reach up to several tens of degrees.

An analysis of the system evolution showed that opening of a seeding crack in the crystallite stretched in the [100] direction ceases when the crack strikes one of the blocks representing a crystalline region rotated relative to the initial orientation. Subsequently, a disordered material region is formed at the site of contact of the crack tip and the block boundary.

A principally different character of the material response was observed on simulating the crystallite tension in the [110] direction. In particular, the model crystal exhibited no fragmentation. The simulation results showed that the initial moment of the crack opening, as well as the crack stop, is weakly dependent on the loading rate and is determined to a considerable degree by the extent of deformation of the model crystallite. For the given loading direction and sample geometry, the crack opening begins at a relative deformation of 8.5% and the crack stops on attaining a deformation threshold of 11.5% (Fig. 2a). Subsequent accommodation of the material proceeds at the expense of dislocations emitted from the crack vertex (Fig. 2b). The emitted dislocations spread at an angle of 45° relative to the direction of loading. This results in the formation of microscopic pores near the boundaries of the regions with incommensurate deformation (Fig. 2c).

Although the deformation rate weakly influences the crack opening onset and stop moments, this parameter significantly affects the crack propagation velocity. For example, an increase in the sample stretching velocity from 1 to 100 m/s leads to an almost threefold increase in the maximum crack propagation velocity (200 to 600 m/s). Since the threshold values of deformation at which the crack starts and stops are almost independent of the stretching velocity, the crack penetration depth at various loading rates is determined by the ratio $\Delta V_{av}/\Delta V_1$, where ΔV_{av} is the average change in the crack propagation velocity corresponding to the stretching velocity increased by V_1. When this ratio is close to unity, the crack penetration depth does not increase with the deformation rate; once the ratio is smaller than unity, the penetration depth would tend to decrease. The smaller the ratio, the more pronounced the decrease in the cracking depth.

In our case, an increase in the sample stretching velocity from 1 to 100 m/s changes the crack propagation velocity from 200 to 600 m/s, which implies that the above ratio is 0.03. Note that determining the average crack propagation velocity is a rather difficult task, because this motion is very nonuniform and characterized by considerable temporal accelerations. In our case, the crack penetration depth decreases with an increasing deformation rate (as is clearly revealed by a comparison of Figs. 2c and 3). Note that the seeding crack propagation across the whole sample (at a given deformation) is hindered by perturbations arising at the opposite free surface.

Thus, the results of our model calculations showed that the effect of the free surface on the seeding crack
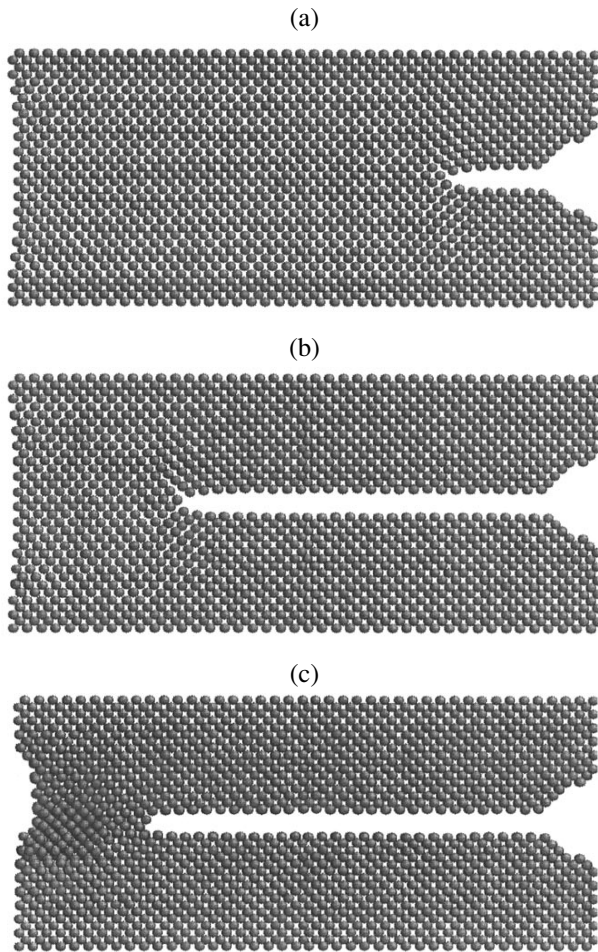
(a)

(b)

(c)

Fig. 3. Crack opening in the model crystallite structure loaded in the [110] direction at a velocity of 10 m/s.

propagation has a pronounced anisotropic character. Structural rearrangements arise in the regions close to the free surface of boundaries between the regions with incommensurate deformation. In a material loaded in the [100] direction, these rearrangements lead to the process of dynamic fragmentation. As was demonstrated, the cracks (in the samples laded along the [100] direction) stop due to the formation of a disordered region at the site of the crack vertex collision with one of the fragments. On loading the sample in the [110] direction, the crack propagation velocity and the depth of its penetration into the material are determined both by the parameters of loading and by the critical deformation at which dislocations are emitted from the crack vertex. This may lead to a characteristic brittle fracture. It should be noted that the effects related to the presence of the free surface are most pronounced in the case of loading in the [100] direction; in the sample loaded in the [110] direction, the effect of the free surface becomes significant as the crack approaches this boundary.

REFERENCES

1. G. P. Dienes and A. Paskin, J. Phys. Chem. Solids **48** (11), 1015 (1987).

2. R. Miller, M. Ortiz, R. Phillips, *et al.*, Eng. Fract. Mech. **48**, 427 (1998).

3. *Physical Mesomechanics and Computer Design of Materials*, Ed. by V. E. Panin (Nauka, Novosibirsk, 1995), Vols. 1, 2.

4. V. E. Panin, Fiz. Mezomekh. **2** (6), 5 (1999).

5. S. M. Foiles, M. I. Baskes, and M. S. Daw, Phys. Rev. B **33** (12), 7983 (1986).

6. A. V. Berch, A. G. Lipnitskiĭ, and E. V. Chulkov, Poverkhnost, No. 6, 23 (1994).

7. S. G. Psakh'e, T. Yu. Uvarov, and K. P. Zol'nikov, Fiz. Mezomekh. **3** (3), 69 (2000).

8. S. G. Psakh'e, T. Yu. Uvarov, K. P. Zol'nikov, *et al.*, Fiz. Mezomekh. **3** (4), 29 (2000).

Translated by P. Pozdeev

Highly Efficient Relativistic SHF Gyrotron with a Microsecond Pulse Width

N. I. Zaĭtsev, N. S. Ginzburg, N. A. Zavol'skiĭ, V. E. Zapevalov, E. V. Ilyakov, I. S. Kulagin, A. N. Kuftin, V. K. Lygin, M. A. Moiseev, Yu. V. Novozhilova, R. M. Rozental', and V. I. Tsalolikhin

Institute of Applied Physics, Russian Academy of Sciences, Nizhni Novgorod, Russia
Received October 19, 2000

Abstract—Based on extensive theoretical and experimental investigations, a new relativistic gyrotron is created with an efficiency of 45% and an output power of up to 7 MW at an SHF pulse width of up to 6 µs. Under optimum conditions, the gyrotron operates in a single-mode regime featuring excitation of the electrically strong TE_{01} mode at a frequency of 9.2 GHz. © *2001 MAIK "Nauka/Interperiodica".*

Introduction. At present, gyrotrons are the most effective sources of high-power radiation in the millimetric wavelength (EHF) range. For example, Gol'denberg *et al.* [1] reported on an ≈2 MW power at a pulse length of 30 µs for a radiation wavelength of $\lambda = 3$ mm. However, the high potentialities of gyrotrons are exhausted with respect to neither radiant power level nor frequency range in which these devices may compete quite well with other generator systems.

Evidently, an increase in the radiant power can be achieved only based on the increase in working currents and voltages, including the passage to relativistic energies. A theoretical analysis performed in [2] within the framework of an approximate model based on reduction of the equations of motion for relativistic particles to the wave equations for nonisochronous oscillators employed in the theory of weakly relativistic gyrotrons showed that the efficiency of a gyrotron may remain on a sufficiently high level in the moderately relativistic energy region (200–500 keV). In order to attain the gyrotron efficiency on a level of 20–30%, it is expedient to reduce the length of the interaction space, thus expanding the cyclotron resonance bandwidth. These theoretical predictions are confirmed in experiment. For example, relativistic gyrotrons described in [3, 4] were operating on the TE_{13} working mode with a wavelength of 3 cm and 8 mm and ensured an efficiency of 20 and 6% at a particle energy of 300 and 900 keV, respectively. However, these devices employed a relativistic electron beam formed with the aid of an explosive emission cathode; the SHF pulse width of these gyrotrons did not exceed several tens of nanoseconds.

In the next stage of investigations, a relativistic gyrotron was modeled based on the relativistic equations of motion and the set of inhomogeneous string equations determining a selfconsistent field profile [5].

The results of this modeling showed that a drop in the gyrotron efficiency upon the passage to the relativistic energy range is considerably lower than that predicted by the approximate asymptotic theory [2]. Moreover, it was established that an additional optimization of the resonator profile may increase the gyrotron efficiency up to 50% [6]. These modeling results served as a base for the development of a new highly efficient relativistic SHF gyrotron operating on the TE_{01} mode at a working frequency of 9.2 GHz.

Resonator optimization. Optimization of the resonator profile was based on a stationary model of the relativistic gyrotron with selfconsistent unfixed field structure. Stability of the working mode excitation under the conditions of competition with parasitic modes was evaluated using a nonstationary model. The following characteristics were used as the working parameters: wrings mode, TE_{01}; wavelength, $\lambda \cong 3.25$ cm ($f = 9.2$ GHz); radius of the homogeneous resonator region, $R_0 = 2$ cm; radius of the electron beam injection into the interaction space, $R_b = 0.75$ cm; accelerating voltage, $U = 280$ kV; beam current, $I = 60$ A; pitch factor, $g = 1.3$; relative scatter of the transverse electron velocity, $\delta v_\perp \approx 30\%$. Figure 1 shows an optimum resonator configuration with a homogeneous region length of 11 cm (thick solid curve) and the corresponding longitudinal profiles of the working mode amplitude and phase in the optimum operation regime.

Figure 2 shows the plots of the gyrotron efficiency versus magnetic field strength for various acceleration voltages increasing in the course of the gyrotron switching on. The values of currents and pitch factors corresponding to each accelerating voltage were selected based on the results of modeling of the screw beam formation in the magnetron injector gun. As seen from Fig. 2, the maximum efficiency (48%) is attained on curve *3* at a magnetic field strength of 4.25–4.3 kOe,
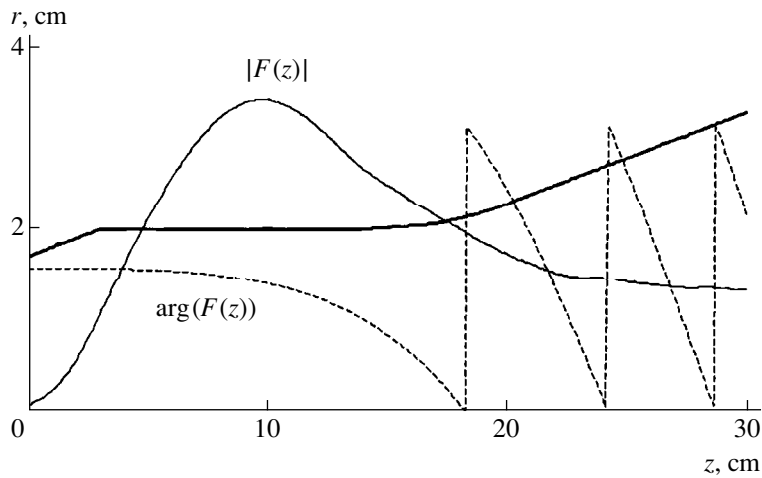
Fig. 1. Optimized gyrotron resonator configuration diagrams showing geometry of the interaction space (thick solid curve), and the corresponding selfconsistent longitudinal profiles of the working mode amplitude $|F(z)|$ (thin solid curve) and phase $\arg[F(z)]$ (dashed curve) in the optimum operation regime.
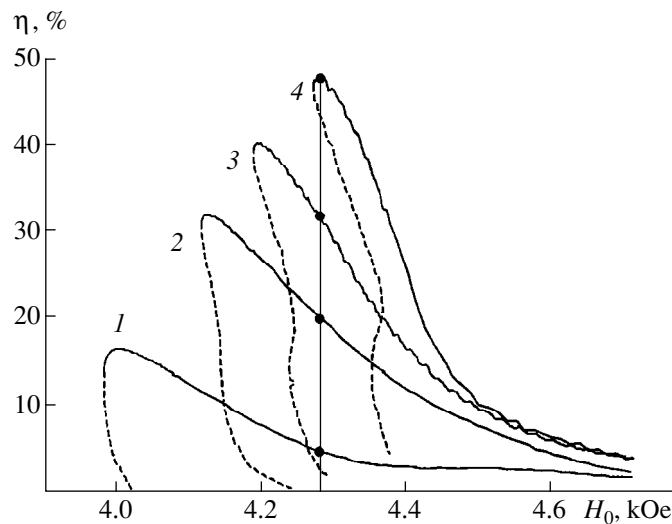

Fig. 2. The plots of gyrotron efficiency η versus magnetic field strength H_0 for various sets of the acceleration voltage and the corresponding values of currents and pitch factors (unstable generation branches are plotted by dashed lines): (*1*) $U = 180$ kV, $I = 48$ A, $g = 0.82$; (*2*) $U = 230$ kV, $I = 54$ A, $g = 1.03$; (*3*) $U = 255$ kV, $I = 57$ A, $g = 1.13$; (*4*) $U = 280$ kV, $I = 60$ A, $g = 1.3$.

which corresponds to a rigid self-excitation regime. However, the regime of excitation at lower voltages (curves *1* and *2*) and the same magnetic field strength is soft, which implies that this branch of the stationary self-oscillation regime is attained for low values of the initial perturbations. As a result, attaining the high-efficiency generation regime in a resonator with the optimum profile is possible at the leading front of the accelerating pulse. In this case, the working mode starts in the soft regime with a relatively low efficiency; as the accelerating voltage grows, the working point adiabatically shifts to the stable branch of curve *3* corresponding to a high-efficiency operation.

Figure 3 shows the plots of start current versus magnetic field strength for the working mode TE_{01} and the

most dangerous parasitic mode TE_{21} constructed for three values of the accelerating voltage. When the accelerating voltage is below 230 kV, the start current of the parasitic mode exceeds that of the working mode in the working range of magnetic fields ($H_0 \approx 4.3$ kOe). However, as the accelerating voltage increases more, the start current of the working mode increases and that of the parasitic mode decreases. The modeling results showed that an adiabatic increase in the accelerating voltage and beam current leads, by virtue of a nonlinear competition mechanism, to suppression of the TE_{21} mode generation and establishing of a single-mode regime of the TE_{01} wave generation. This point needs special thorough investigation, since the characteristic transient times for establishing of the oscillation
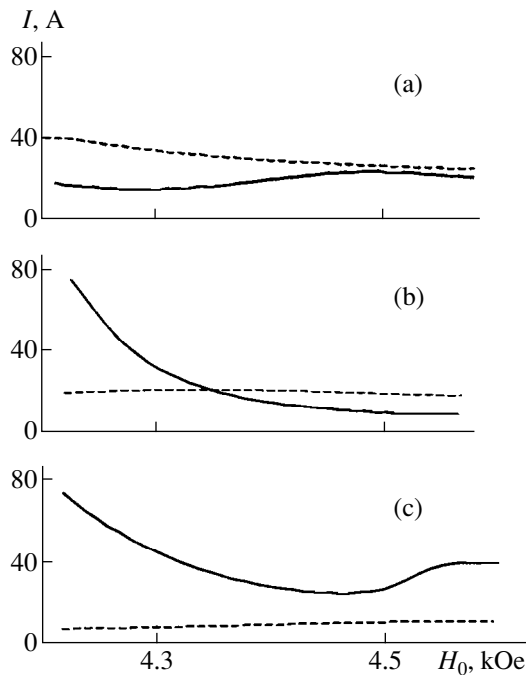
Fig. 3. The plots of start current I versus magnetic field strength H_0 for the working mode TE_{01} (solid curves) and the most dangerous parasitic mode TE_{21} (dashed curves) at various values of the accelerating voltage: (a) 180, (b) 230, (c) 280 kV.

regimes are comparable with the leading front duration of the accelerating voltage pulse.

Working regime simulation. An additional analysis and modeling of the operating regime dynamics

were performed with the aid of a two-dimensional version of the KARAT PIC-code. This code directly models the Maxwell equations in combination with the equations of motion for macroparticles moving in the three-dimensional space in an axisymmetric system. In addition, the KARAT code allows the accelerating voltage and the beam current to be set as functions of time, thus providing for the possibility of modeling the switch-on regime under conditions close to experiment.

Upon instantaneously switching the current and accelerating voltage, the system does not generate the working TE_{01} mode, which confirms a rigid character of the working regime excitation. The high-efficiency working regime was attained by monotonically increasing the accelerating voltage within a few hundreds of nanoseconds. Figure 4 shows experimental oscillograms of the accelerating voltage and output power pulses in comparison to the analogous curves obtained by modeling for the regions corresponding to a high-efficiency operation ($H_0 > 4.3$ kOe) and to a breakdown of this regime ($H_0 < 4.3$ kOe). As seen from these data, the character of the transient process observed for the working TE_{01} mode agrees well with the modeling results.

Experimental results and discussion. Experimental investigation of the relativistic SHF gyrotron were performed using a Saturn accelerator at the Institute of Applied Physics (Nizhni Novgorod) [7]. Using this facility, it was possible to produce single pulses of accelerating voltage with a length of the flat pulse portion (corresponding to the relative voltage variation not exceeding 3%) up to 6 μs and an amplitude of up to 300 kV. A screw relativistic electron beam was
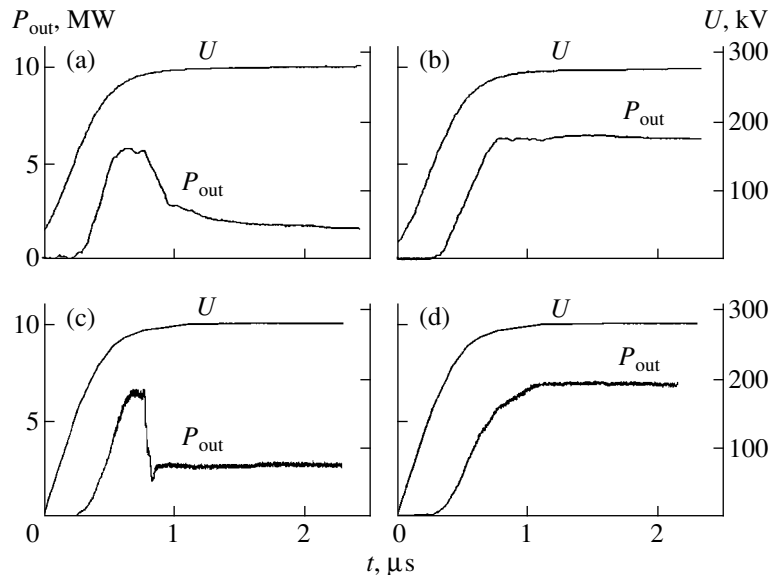

Fig. 4. (a, b) Experimental oscillograms of the accelerating voltage U and output power pulses P_{out} in comparison to (c, d) analogous curves obtained by KARAT PIC-code modeling for the region of parameters corresponding to (a, c) unstable regime ($H_0 < 4.3$ kOe) and (b, d) high-efficiency operation ($H_0 \approx 4.35$ kOe).
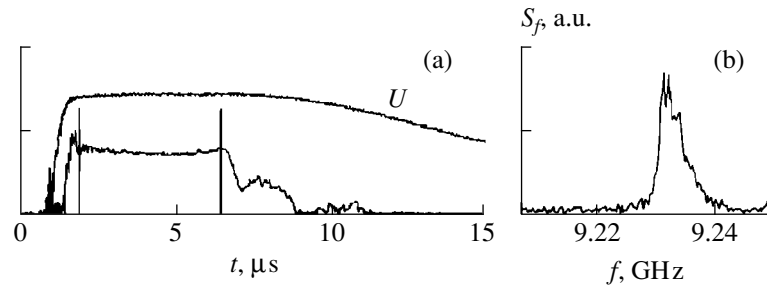
Fig. 5. (a) Oscillograms of the accelerated voltage pulse and the output power measured in the working generation regime; (b) the output radiation spectrum for a stationary generation in the optimum regime (indicated by vertical bars in part (a)).
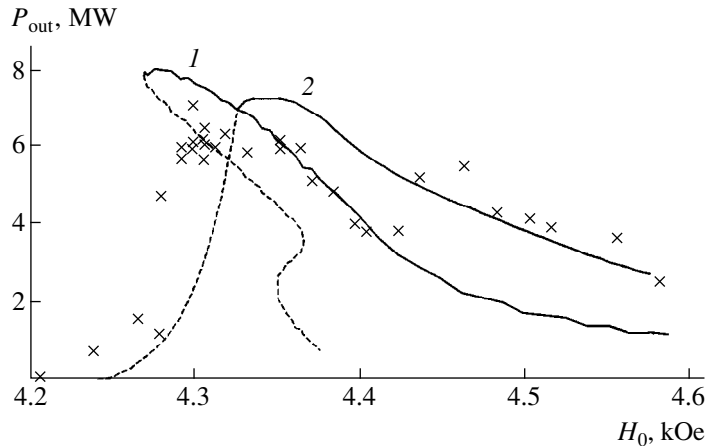

Fig. 6. Plots of the output radiation power P_{out} versus resonance magnetic field strength H_0: (1) a stationary unfixed field structure model; (2) KARAT PIC-code, ($\times$) experimental points.

obtained with the aid of three-electrode electron gum of the magnetron injector type with thermionic cathode developed based on the EPOS program [8]. In this experiment, the gun operated in the regime of space-charge-limited injection current (ρ-regime) to form a tubular electron beam with a median diameter of 15 mm, a maximum current of 55 A, and a pitch factor of 1.3.

The maximum gyrotron radiant power was 7 MW at a pulse width of up to 6 μs and an efficiency of 45%. Figure 5a shows oscillograms of the accelerated voltage pulse and the output power measured in the working generation regime. Figure 5b presents the output radiation spectrum for the stationary generation region, in which the bandwidth does not exceed 5 MHz. Figure 6 shows plots of the output radiation power versus the resonance magnetic field strength in comparison to the theoretical curves constructed by data calculated within the framework of a stationary unfixed field structure theory and by the results of modeling using the KARAT code. A difference between the optimum magnetic field strengths according to the stationary model calculations and the KARAT code modeling can be explained by the fact that the latter approach more adequately takes into account factors such as the space charge of the electron beam, finite thickness of the beam wall, electron velocity scatter, etc.

It should be noted that the SHF pulse width in the optimum generation regime coincides with the length of the flat portion of the accelerating voltage pulse (Fig. 5). It must be emphasized that the magnetic field strength deviation from the optimum value (accompanied by the TE_{21} mode generation) led to a sharp decrease in the pulse width (to several hundreds of nanoseconds). This fact shows advantage of using the azimuthally-symmetric TE_{0n} modes as the working modes: the absence of normal electric field components on the walls of the electrodynamic system reduces the SHF breakdown probability.

Conclusion. The results of theoretical and experimental investigations confirmed the possibility of constructing a relativistic gyrotron with a high (up to 45%) efficiency. Under the optimum operation conditions, the system is operating in a single-mode regime featuring excitation of the electrically strong TE_{01} mode at a frequency of 9.2 GHz with an output power of up to 7 MW and an SHF pulse width of up to 6 μs. Experimental data on the output radiant power as a function of the resonance magnetic field strength agree with the results of calculations based on a stationary theory with

unfixed field structure and on the results of modeling using the KARAT PIC-code.

REFERENCES

1. A. L. Gol'denberg, G. G. Denisov, V. E. Zapevalov, *et al.*, Izv. Vyssh. Uchebn. Zaved., Radiofiz. **39** (6), 635 (1996).

2. V. L. Bratman, N. S. Ginzburg, G. S. Nusinovich, *et al.*, Int. J. Electron. **51** (4), 541 (1981).

3. N. S. Ginzburg, V. I. Krementsov, M. I. Petelin, *et al.*, Zh. Tekh. Fiz. **49** (2), 378 (1979) [Sov. Phys. Tech. Phys. **24**, 218 (1979)].

4. S. H. Gold, A. W. Fliflet, W. M. Manheimer, *et al.*, IEEE Trans. Plasma Sci. **16** (2), 142 (1988).

5. M. A. Moiseev, L. L. Nemirovskaya, V. E. Zapevalov, and N. A. Zavolsky, Int. J. Infrared Millim. Waves **18** (11), 2117 (1997).

6. N. A. Zavol'skiǐ, V. E. Zapevalov, and M. A. Moiseev, Izv. Vyssh. Uchebn. Zaved., Radiofiz. (2001) (in press).

7. N. I. Zaǐtsev, E. V. Ilyakov, G. S. Korablev, *et al.*, Prib. Tekh. Éksp., No. 3, 138 (1995).

8. V. K. Lygin, V. N. Manuilov, and Sh. E. Tsimring, Élektron. Tekh., Ser. 1: Élektron. SVCh **7**, 36 (1987).

Translated by P. Pozdeev

Waveguide Spectroscopy of Thin Films

A. V. Khomchenko

Institute of Applied Optics, National Academy of Sciences of Belarus, Mogilev, Belarus
e-mail: ipo@physics.belpak.mogilev.by
Received June 19, 2000; in final form, November 13, 2000

Abstract—A waveguide method of measurement of the absorption spectra of thin films in the range of their transparency is considered. The absorption spectra obtained by this method for the thin films of tin oxide and zinc oxide in a wavelength range from 400 to 800 nm are presented. The error of measurement of the absorption spectrum did not exceed 5% for an ~0.1-μm-thick film with an absorption coefficient of ~50 cm^{-1}. Possibilities and limitations of the method are discussed. © *2001 MAIK "Nauka/Interperiodica".*

The electrical and optical properties of semiconductor and dielectric thin-film structures are determined to a considerable extent by the characteristics and distribution of electron states in the forbidden band. For polycrystalline and amorphous films prepared under nonequilibrium conditions, the properties of which depend on the features of the deposition process, these data can be obtained only in experiment. Certain information in this respect is provided by the optical spectroscopy measurements in the region of frequencies below the fundamental absorption edge, However, the existing optical methods are difficult to employ for measuring the absorption spectra of thin films with the absorption coefficients $\alpha < 10$ cm^{-1}. This is related to the fact that a direct measurement of the absorption for $\alpha d \ll 1$, where d is the film thickness, becomes uncertain. The photoconductivity techniques, which allow the material parameters to be determined for $\alpha \approx 1$ cm^{-1} in semiconductor materials, are poorly applicable to dielectric films. For this reason, a considerable effort by researchers is devoted to the development of better methods for the study of thin films [1].

A high-precision method for the diagnostics of thin films is offered by the waveguide techniques. An advantage of these techniques is a high resolution and the ability of directly determining the refractive index of thin films with thicknesses from a few tenths of a micron to several tens of microns. Attempts at determining the spectral dependence of the absorption coefficient of thin films were undertaken within the framework of the surface electromagnetic wave spectroscopy [2], which allowed the vibrational spectra of monomolecular layers and natural oxide films on the surface of metals to be studied. This method has proved to be rather effective in the IR spectral range. In the visible range, it was suggested to study the spectra of absorbing films using the optical waveguide modes [3]. For this purpose, the sample films were placed on the waveguide surface, so that the radiation intensity attenuation in the waveguide was modified by the absorption in the film

due to the waveguide mode field penetration into the adjacent medium. This method gave satisfactory results for ultrathin films (with a thickness of 10–15 Å). The spectral dependence of the absorption coefficient of thin films was also studied by directly measuring the real h' and imaginary h'' parts of the propagation constant h of the waveguide modes in a two-prism geometry [4]. Unfortunately, the need for an additional adjustment of the prismatic coupling device depending on the incident radiation frequency and the dependence of h'' on the prism–waveguide coupling efficiency restricts the applicability of this method.

All the above problems can be eliminated to a certain extent using the method of waveguide spectroscopy described below. The proposed approach to measurements of the spectral dependence of the absorption coefficient of thin films is essentially a development of the method used previously [5, 6], representing an extension of these measurements to the case of non-monochromatic radiation. The measurements involve registration of the spatial Fourier spectrum of a light beam reflected from a prismatic coupling device upon a waveguide mode excitation in the thin-film structure studied. An analysis of the experimental results showed that the error of determination of the waveguide mode propagation constant relative to the h'' value measured at a laser radiation frequency did not exceed 1%, provided that the spectral bandwidth of the probing radiation was restricted to below 60 nm and an appropriate optical scheme is employed. Evidently, the effect of the degree of coherency on the accuracy of restoration of the waveguide mode parameters requires additional investigation, because the formation of an intensity distribution pattern in the reflected beam cross section is related to the interference of light fields. However, the results of our measurements showed that the proposed method actually allows the spectral dependence of the absorption coefficient of thin films to be determined in a sufficiently broad range of wavelength, the more so that the prismatic element used for the optical
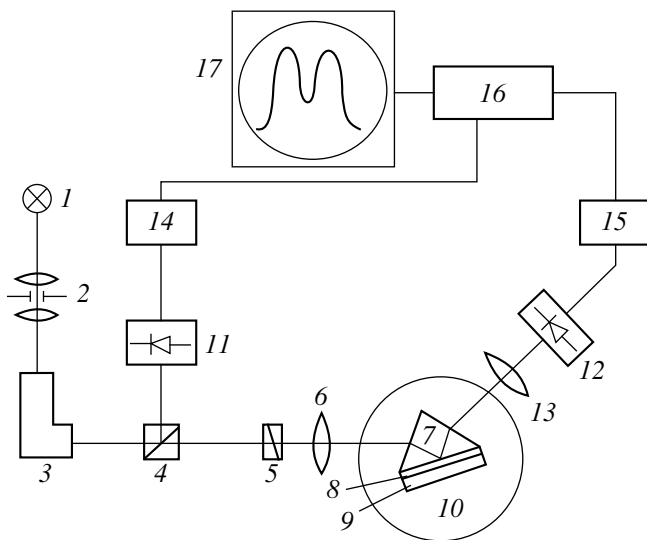
Fig. 1. A schematic diagram of the experimental setup: (*1*) frequency-tunable radiation source with controlled intensity; (*2*) collimator; (*3*) monochromator; (*4*) beam splitting cube; (*5*) polarizer; (*6*) focusing device; (*7*) prismatic coupling device; (*8*) thin-film waveguide (sample); (*9*) substrate; (*10*) rotary table; (*11*, *12*) photodetectors; (*13*) optical Fourier converter; (*14*, *15*) intensity-measuring units; (*16*) analog-to-digital converter; (*17*) computer.

waveguide excitation restricts the spectral bandwidth to 10–40 nm [7].

Upon the waveguide mode excitation, the display shows a series of dark *m*-lines. Each line considered separately exhibits a spatial intensity distribution of its own observed in the reflected light [5]. By properly selecting the exciting beam parameters, this pattern can be readily recorded. These measurements were performed in a specially designed computer-controlled setup, a schematic diagram of which is presented in Fig. 1. The setup measures the intensity of a beam reflected (at a fixed incidence angle) from a prismatic coupling device. A confined light beam from a frequency-tunable radiation source is incident onto a prismatic coupling device *7*. This device represents an equilateral measuring prism mounted on a rotary table *10*. The incident light beam excites a waveguide mode in a sample film *8* on substrate *9*. The complex propagation constant *h* of this mode depends on the optical parameters and thickness of the film. The prism was made of an optical glass (TD12 grade) with a refractive index of 1.77905 at a wavelength of 0.6328 µm. The measurements can be performed using various polarizations of the incident light. It was also possible to control the light beam radius from 15 to 150 µm. The transverse beam size was measured for an intensity level of $I = I_0 e^{-1}$, where I_0 is the light intensity at the beam axis.

The measured sample on substrate *9* was pressed against the coupling prism surface so as to provide for the optimum conditions of the optical mode excitation. A spatial distribution of the intensity of the reflected light

beam was measured using a photodetector array *12*. The axis of rotation of the detector array coincides with that of the rotary table, while the working detector area is situated in the focal plane of the objective lens *13* transmitting the reflected beam. The incident light intensity was measured with photodetector *11*. The output signal was digitized and transferred via interface to the computer memory. The instrumental error of determination was 2×10^{-5} for the optical mode excitation angle and 0.1% for the light intensity.

As the probing radiation frequency is varied during the measurements, the pattern of the intensity distribution exhibits a transformation. Using the gradient descent method (the applicability of which to restoring the mode parameters was justified in [6]), it is possible the determine the real *h'* and imaginary *h"* parts of the complex propagation constant *h* for an asymmetric curve of the reflected beam intensity distribution. The index of refraction, absorption coefficient, and thickness of the sample film can be determined using the *h* values determined for various modes [6]. It should be emphasized that the approach proposed for determining the propagation constant allows the effect of the prismatic coupling device to be taken into account, thus giving the values of parameters independent of the prism–waveguide coupling efficiency. Note that the method does not involve absolute measurements of the light intensity. Use of a wide (in the wavevector space) light beam and application of the gradient descent method for determining *h* eliminates the need for any additional adjustment of the prismatic coupling device depending on the incident radiation frequency. As a result, the measurements reflect a variation of the absorption coefficient of a sample thin film in a preset spectral interval and allow the refractive index *n* and thickness of the sample to be determined. The film thickness determination can be used for verification of the waveguide spectroscopy data by comparing this value to a thickness determined by an independent technique such as the multibeam interference or profilography.

In this experiment, the measurements were performed for a series of thin films prepared by the RF sputtering of a ZnO ceramic target onto a quartz glass substrate at $T = 300$ K. The film had a thickness of 1.5 µm and could transmit five waveguide modes. Figure 2 shows the results of measurements of the $h"(\lambda)$ spectrum using a third-order waveguide mode with TE polarization. The same figure shows the plots of $n(\lambda)$ and $k(\lambda)$ values determined from the waveguide measurements, where *k* is related to the absorption coefficient by the relationship $\alpha = 4\pi k/\lambda$. The average sample film thickness is $d = 1.50 \pm 0.01$ µm; the film thickness determined on a profilometer was 1.50 ± 0.02 µm. As seen from the curves in Fig. 2, the spectral dependence of the absorption coefficient of the films studied is well described by the $h"(\lambda)$ curve. This result indicates that the measurement of the $h"(\lambda)$ value is sufficient for

determining the absorption coefficient of the film material.

Analogous measurements were also performed for the films of $SnO_2:Sb_2O_5$, $SnO_2:Al_2O_3$, and $SnO_2:WO_3$ deposited by the same method onto quartz glass substrates at 420 K. The $SnO_2:Sb_2O_5$ film had a thickness of 0.7 μm and could transmit two TE-polarized waveguide modes. Figure 3 shows the $h''(\lambda)$ curves for the $SnO_2:Sb_2O_5$ films doped with antimony to various degrees as well as the curves for $SnO_2:Al_2O_3$ and $SnO_2:WO_3$ (measured using the TE-polarized fundamental mode). As seen from these spectral data, a modification of the film composition is manifested by changes in the structure and positions of the absorption bands in the spectral range of transparency.

A sensitivity of the proposed method can be demonstrated by the following experimental results. As is known, the films of tin dioxide are widely used in the active elements of gas sensors [8]. The electrical properties of these films significantly change already upon adsorption of a single monolayer of gas molecules. It was natural to expect that the spectral parameters of such films would exhibit adsorption-induced changes as well. Figure 3 shows the spectral dependence $h''(\lambda)$ for a $SnO_2:Sb_2O_5$ film measured in pure air and in a mixture of air with ammonia vapors (curves 5 and 6, respectively). As seen, the presence of ammonia at a concentration of 0.01 mg/l produces a noticeable change in the film parameters, which is revealed by the absorption spectrum measured.

A total relative error of the determination of $k(\lambda)$ with an allowance for the systematic uncertainty did not exceed 0.03. The spectral interval of measurements was limited by the available equipment. Realization of the waveguide spectroscopy method encounters problems in determining the $k(\lambda)$ values below 10^{-5}, which is explained by restrictions of the waveguide measurements related to a "leak" of the waveguide mode energy in the prismatic coupling device [6]. This circumstance should be taken into account during the measurements of parameters of weakly absorbing films: the method is applicable to the films with thicknesses below 1 μm, provided that the absorption coefficient is ~ 1 cm^{-1} ($k = 2 \times 10^{-6}$). For sufficiently thick semiconductor films ($d \sim 1$ μm), the experimental procedure is simplified because $k \approx h''$ [9] and it is sufficient to measure only h'' in order to determine the absorption coefficient of the film material.

The condition that guided modes must exist in the structure studied is not necessary, provided that the film is applied onto a weakly absorbing substrate (i.e., when the absorption coefficient of the substrate is significantly smaller than the k value of the film studied). In this case, the refractive index of the substrate can be even greater than that of the film. The film parameters can be determined from data on the propagation constant of the outgoing modes [6].
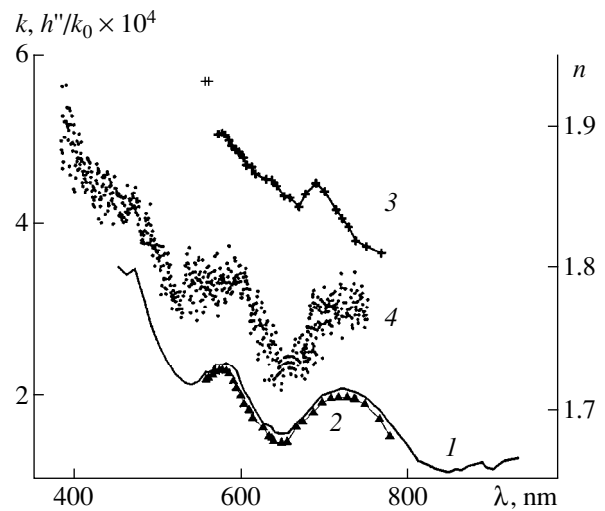
$k, h''/k_0 \times 10^4$

Fig. 2. Waveguide spectra of (1) h'', absorption coefficient $k(\lambda)$ (2), and (3) refractive index $n(\lambda)$ of a ZnO film. Curve 4 shows a $k(\lambda)$ curve measured by the transmission spectroscopy method.
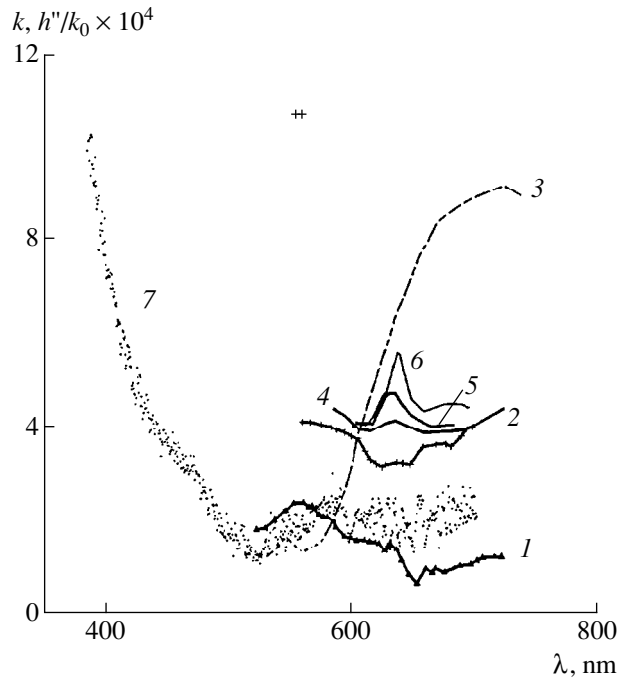

$k, h''/k_0 \times 10^4$

Fig. 3. Waveguide spectra of SnO_2 films with various dopants: (1, 4, 5) $SnO_2:Sb_2O_5$ (with various Sb concentrations, $C_1 < C_2 < C_3$, respectively); (2) $SnO_2:Al_2O_3$, and (3) $SnO_2:WO_3$. Spectra 5 and 6 were measured for the same $SnO_2:Sb_2O_5$ sample in pure air and in air with ammonia vapors, respectively. Curve 7 shows a $h''(\lambda)$ curve for $SnO_2:WO_3$ measured by the transmission spectroscopy method.

For the comparison, the spectral dependence of the absorption coefficient of thin films was also measured by the transmission spectroscopy. Figure 2 (curve 4) shows the corresponding spectrum of $k(\lambda)$ for a zinc oxide film; Fig. 3 (curve 7) shows the optical transmis-

sion data for a SnO_2:WO_3 film. As seen, the shapes of the spectra obtained by the two methods exhibit good correlation. A maximum discrepancy between $k(\lambda)$ and $h''(\lambda)$ cures was observed for thin films in the long-wavelength spectral region (Fig. 3). This can be explained from the standpoint of the waveguide mode theory [9]. Indeed, an increase in the radiation wavelength leads to a decrease in the effective film thickness; however, the SnO_2:WO_3 film thickness was only 0.3 μm and the $h''(\lambda)$ value was not equal to $k(\lambda)$.

The results presented above indicate that the method of waveguide spectroscopy can be used for determining the spectral parameters and optical properties of thin films in the range of their transparency.

REFERENCES

1. M. A. Bukhshtab, *Measurements of Small Optical Losses* (Énergoatomizdat, Leningrad, 1988).

2. P. I. Nikitin, Sens. Sist. **12** (1), 69 (1998).

3. V. A. Yakovlev, V. A. Sychugov, and A. V. Tishchenko, Pis'ma Zh. Tekh. Fiz. **8** (11), 665 (1982) [Sov. Tech. Phys. Lett. **8**, 289 (1982)].

4. M. Oliver, J.-C. Peuzin, and J.-S. Danel, Appl. Phys. Lett. **38** (2), 79 (1981).

5. V. P. Red'ko, A. A. Romanenko, A. B. Sotskiĭ, and A. V. Khomchenko, Pis'ma Zh. Tekh. Fiz. **18** (3), 14 (1992) [Sov. Tech. Phys. Lett. **18**, 100 (1992)].

6. A. B. Sotskiĭ, A. A. Romanenko, A. V. Khomchenko, and I. U. Primak, Radiotekh. Élektron. (Moscow) **44** (5), 1 (1999).

7. S. B. Mendes, L. Li, J. J. Burke, *et al.*, Appl. Opt. **34** (27), 6180 (1995).

8. V. V. Kisin, V. V. Sysoev, and S. A. Voroshilov, Pis'ma Zh. Tekh. Fiz. **25** (16), 54 (1999) [Tech. Phys. Lett. **25**, 657 (1999)].

9. A. M. Goncharenko and V. A. Karpenko, *Foundations of the Theory of Optical Waveguides* (Nauka i Tekhnika, Minsk, 1983).

Translated by P. Pozdeev

Experimental Investigation
of a Light-Controlled Nonlinear Scatterer

A. V. Kashin, A. L. Umnov, and V. A. Yashnov

Research Institute of Measuring Systems, Nizhni Novgorod, Russia
Nizhni Novgorod State University, Nizhni Novgorod, Russia
Received November 9, 2000

Abstract—It is demonstrated that the spectrum of a high-frequency signal reradiated by a nonlinear scatterer can be controlled using optical radiation. The scatterer is a monopole antenna with a nonlinear element (phototransistor). By illuminating the phototransistor, it is possible to change its nonlinear conductance and capacitance and thereby the spectrum of the scattered signal. The low-frequency (LF) modulation of parameters of the nonlinear element caused by the modulated optical radiation results in modulation of the scattered signal both at the base frequency and the combination frequencies produced by the nonlinear conversion. The proposed scatterer can be used as a feederless sensor of the electric field whose output signal can be readily separated from interferences due to the LF modulation. © 2001 MAIK "Nauka/Interperiodica".

An interesting trend in the modern antenna engineering is the use of nonlinear scatterers. The nonlinear scatterers (passive antennas) serve as markers enabling the identification of the marked object by the spectrum of the reradiated signal. In addition, these scatterers can be used as feederless sensors of the electromagnetic field which allow recording the field parameters with minimum distortions in the field structure [1–6].

One of the basic problems that must be solved when we use nonlinear scatterers is the problem of separating the signal reradiated by the chosen scatterer from interfering signals [7, 8]. This problem becomes especially topical when we simultaneously use a large number of identical scatterers which may form an array. The problem of identification of a particular scatterer can be solved by individualizing spectral characteristics of the signal reradiated by this scatterer. This can be done, for example, by varying some parameters of the chosen scatterer in a certain manner, which causes modulation of the reradiated signal. The modulation thus imposed on the detected signal substantially alleviates the separation of this signal from interferences generated by the other array elements.

This study is devoted to the experimental investigation of the feasibility of remote control over parameters of a passive nonlinear scatterer with the help of the laser beam.

The layout of the experiment is shown in Fig. 1. The experiments were conducted in a laboratory room with dimensions of $15 \times 8 \times 2.5$ m. No special measures were taken to reduce the reflection of electromagnetic waves from the room walls. The scatterer under study is monopole *7* representing an extension of the inner conductor of a feeder whose outer conductor (armor) is connected to a metal plate. A nonlinear element *10* is connected to sides of an open gap in the monopole conductor at a 10-cm distance from the plate. The nonlinear element used in the series of experiments described is a phototransistor of the FT-1K type. The length of the monopole can be smoothly varied from 10 cm to 2 m. The metal plate dimensions are 50×50 cm. The nonlinear element can be illuminated by the beam of a helium–neon laser *8*. The intensity of the light flux created by the laser can be controlled with the help of polarizer *9*. The experimental setup also contains two transmitting (*1* and *2*) and one receiving (*5*) antenna. The transmitting antennas are connected via coaxial cables to a high-frequency (HF) pumping generator *4* and a signal generator *3*. The receiving antenna *5* is connected to the input of a spectrum analyzer *6*. The inner conductors of the coaxial cables are connected to antennas and the outer ones, to metal plates.

The design of the receiving and transmitting antennas is similar to that of the scatterer except for the nonlinear element, which is only present in the scatterer. In all the experiments, the level of the output signal from the pumping generator *4* was substantially lower than that of the signal from the reference generator *3*. The lengths of antennas *1* and *2* were initially chosen so as to maximize the response at the receiver output (the spectrum analyzer *6*) for chosen frequencies of the base and pumping signal. The length of antenna *5* was tuned so as to provide for the maximum signal at the reception frequency (either the base or the combination frequency). Both the arrangement of all the antennas and their mutual distances can be varied. In the course of experiments, we recorded the signal reradiated by the scatterer *7* at frequencies of the second harmonics of these generators and at the combination (sum) frequency.
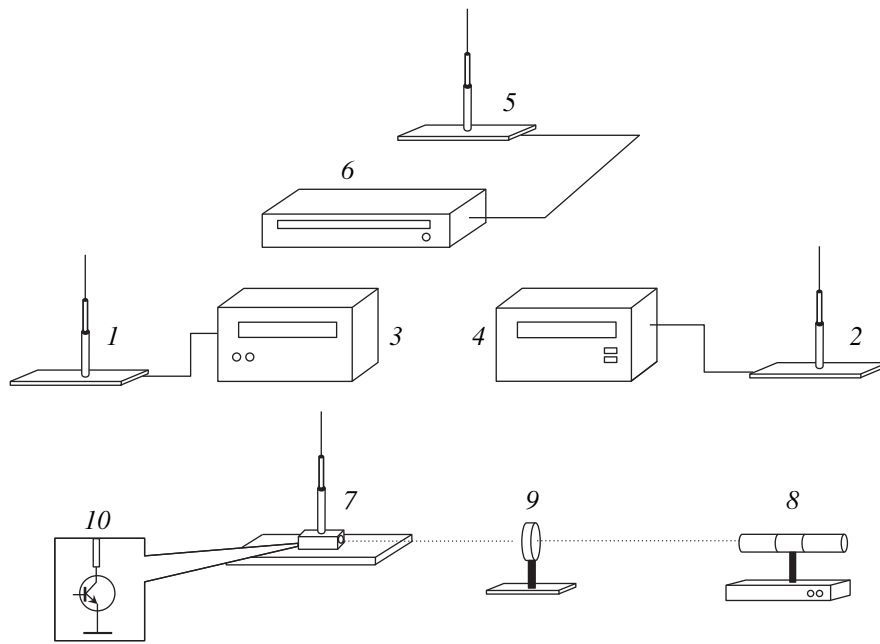
Fig. 1. Layout of the experiment: (*1*) antenna radiating the signal; (*2*) antenna creating the pumping field; (*3*) U4-158 signal generator; (*4*) G3-19F pumping generator; (*5*) receiving antenna; (*6*) S4-27 spectrum analyzer; (*7*) nonlinear scatterer; (*8*) OKG-13 helium-neon laser; (*9*) polarizer; (*10*) phototransistor (connection diagram).

The results of these experiments are presented in Fig. 2. A typical spectrum of the signals received by antenna *5* at the second harmonics of the reference generator *3* ($2f_s$) and the pumping generator *4* ($2f_p$), as well as at the combination frequency ($f_s + f_p$) lying between the harmonics, is shown in Fig. 2a. Dark bars refer to the amplitudes of these signals measured with out laser illumination and the light bars, to the signals received in the presence of the laser beam. In this experiment, $f_s = 76.9$ MHz and $f_p = 77.3$ MHz. This histogram shows that the laser illumination of the phototransistor may substantially change the spectrum.

In order to establish the laws describing operation of the nonlinear scatterer, we studied amplitudes of the signals received at the combination frequency and the second harmonics as functions of the levels of the output signals of the reference and pumping generators, depending on the mutual arrangement of transmitting antennas, scatterer, and receiving antenna. Figure 2b presents amplitudes of signals received at the combination frequency and the second harmonic of the pumping generator (the lower and upper curves, respectively). As seen from the figure, it is possible to change the relationship between amplitudes of the spectral components by varying the laser radiation power. Variations depicted in the figure are nonmonotonic. It should be noted that, changing the mutual arrangement of the antennas used in the experimental setup, it was possible to transform the second-harmonic amplitude minimum into a maximum. The amplitude of the signal scattered at the combination frequency and at the second harmonic of the reference generator depends almost linearly on amplitudes of the signals entering antennas *1* and *2*.

A qualitative explanation of the obtained experimental results can be given by considering the phototransistor as an equivalent nonlinear lossy capacitor whose capacitance is changed by laser radiation. The light incident onto the *p–n* junction region of this phototransistor induces a photoemf and changes the junction thickness. Figure 3 presents the measured dc collector–emitter voltage of the phototransistor used in the experiments as function of the laser radiation power. Evidently, the region of an abrupt change of the voltage generated by the phototransistor corresponds to a change in the *p–n* junction thickness and, as a result, in an equivalent capacitance of the phototransistor.

A nonlinear character of the capacitance and resistance of the *p–n* junction causes generation of the harmonics of incident signals and their combination frequencies in the scatterer circuit. Parameters of this nonlinearity depend on the level of the light signal incident on the phototransistor. The light-induced change in the capacitance of the nonlinear element connected into the monopole scatterer causes detuning from the combination frequency and the second harmonic of the pumping generator and changes the power reradiated by the scatterer at these frequencies, as demonstrated by a resonance character of the curves presented in Fig. 2b. Note that the interval of power levels of the laser radiation in which we observe a substantial variation of signal amplitudes at the harmonic and combination frequency corresponds to the interval of power levels which cause an abrupt change in the photoemf (Figs. 2b and 3).
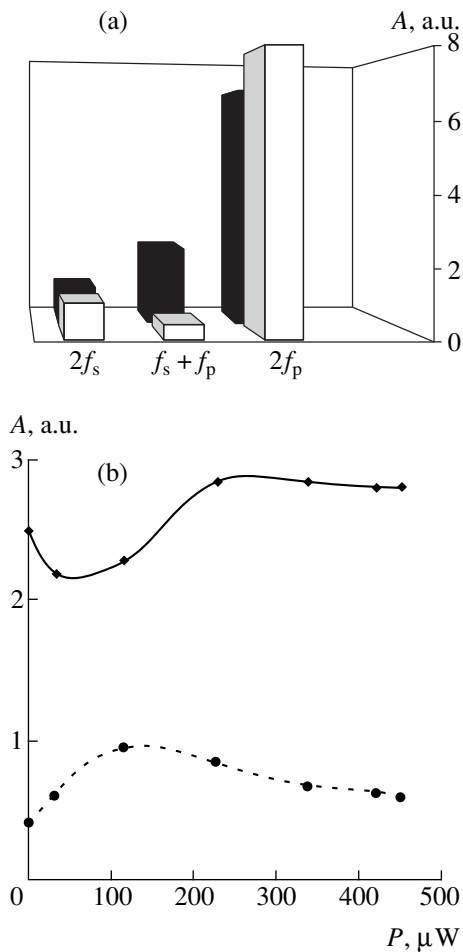
Fig. 2. (a) A histogram of signal amplitudes at the combination frequency and frequencies of the second harmonics measured with and without the laser-induced modulation (dark and light bars, respectively) and (b) diagrams of the signal amplitude at the frequencies $f_s + f_p$ (bottom curve) and $2f_p$ (top curve) vs. laser radiation power.
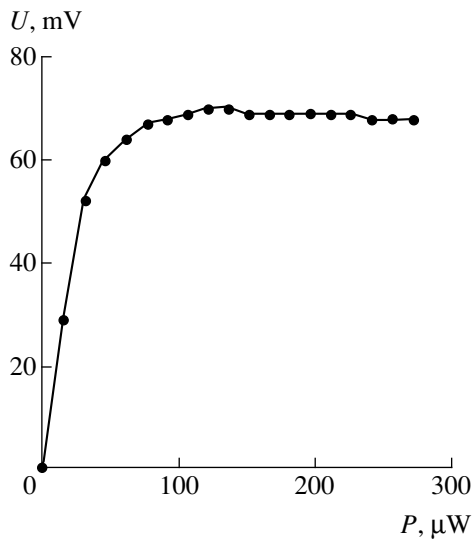
To clarify the behavior of the effective capacitance of the phototransistor as a function of the laser radiation power, we performed an experiment in which the phototransistor was inserted directly into the antenna connected to the output of the HF generator *4*. The results of this experiment are presented in Fig. 4. Behavior of the amplitude of the received signal depends on the ratio of the antenna length *L* to the generator wavelength λ. For a "long" antenna ($L > \lambda/4$, the imaginary part of the input impedance is inductive), the light incident onto the phototransistor lowers the amplitude of the received signal (curve *1*); for a "short" antenna ($L < \lambda/4$, the imaginary part of the input impedance is capacitive), the signal amplitude increases (curve *3*); and for the intermediate antenna length ($L \approx \lambda/4$, resonance region), we have a function with a wide maximum (curve *2*). The revealed behavior of the signal amplitude indicates that illumination of the phototransistor increases its equivalent capacitance.

In the course of the experiment, we observed the following effect: the amplitude of the second harmonic of the pumping generator may be either decreasing or increasing function, depending on the mutual arrangement of antennas *2* and *7*. This effect is apparently caused by the interference of two signals arriving at the receiving antenna. The first is the direct signal from the pumping generator, and the second signal is created by the nonlinear scatterer. Depending on the phase shift between these signals (which is determined by a distance between the antennas), the sum signal at the output of the receiving antenna may change in amplitude.

Note that the idea of tuning antennas using semiconductor devices with varied capacitance is not new [9]. However, a scheme with the *p–n* junction controlling the capacitance of a nonlinear antenna with the help of the light from a quantum generator was not implemented.

Fig. 3. A plot of the phototransistor dc emitter–collector voltage vs. laser radiation power.
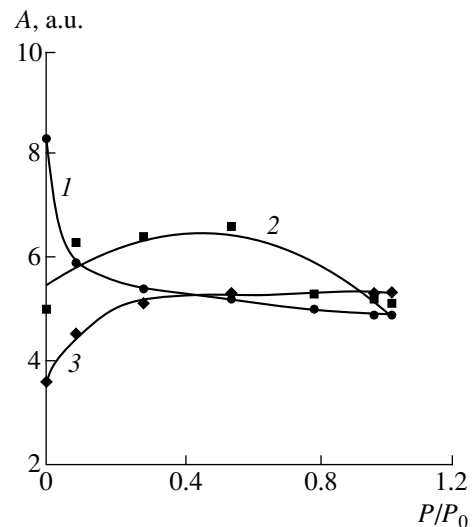

Fig. 4. Plots of the signal amplitude at 99.5 MHz vs. normalized laser radiation power for different lengths *L* of the antenna arm $L = 111$ (*1*), 82 (*2*), and 72 (*3*) cm; $P_0 = 500\ \mu W$.

Thus, in this work we experimentally demonstrated the feasibility of remote control over the spectrum of the HF signal reradiated by a nonlinear scatterer with the help of an optical radiation. The light-controlled nonlinear scatterer can be used, for example, as a feederless field sensor whose signal can be readily separated from interferences due to the HF modulation. Elimination of the metal feeder minimizes distortions in the investigated field arising in the course of measurements, which is especially important when the sensor is used as the element of an array antenna.

REFERENCES

1. A. S. Kuznetsov and G. I. Kutin, Zarubezhn. Radioélektron., No. 4, 41 (1985).

2. P. M. Musabekov and S. N. Panychev, Zarubezhn. Radioélektron. Usp. Sovrem. Radioélektron., No. 5, 54 (2000).

3. A. A. Gorbachev and T. M. Zaboronkova, Radiotekh. Élektron. (Moscow), No. 10, 89 (1988).

4. Ya. S. Shifrin, Zarubezhn. Radioélektron. Usp. Sovrem. Radioélektron., No. 4, 33 (1997).

5. N. S. Vernigorov, Radiotekh. Élektron. (Moscow) **42** (10), 1181 (1997).

6. G. Franceschetti and I. Pinto, *Non-Linear Electromagnetics*, Ed. by P. Uslenghi (Academic, New York, 1980; Mir, Moscow, 1983), pp. 228–240.

7. A. A. Gorbachev, S. V. Lartsov, S. P. Tarakankov, and E. P. Chigin, Radiotekh. Élektron. (Moscow) **43**, 72 (1998).

8. A. A. Gorbachev, Radiotekh. Élektron. (Moscow) **44** (10), 1164 (1999).

9. D. Lamensdorf, Proc. Inst. Electr. Eng. **122** (4), 353 (1975).

Translated by A. Kondrat'ev

Pulsed Magnetic Field Processing of Silicon Substrates Prior to Thermal Spray Film Deposition

M. N. Levin, V. N. Semenov, and A. V. Naumov

Voronezh State University, Voronezh, Russia

e-mail: levin@lev.vsu.ru

Received October 23, 2000

Abstract—Prior to depositing thin metal sulfide films by spraying aqueous solutions of thiocarbamide complexes of the corresponding metals onto heated silicon substrates, the semiconductor substrates were subjected to a pulsed magnetic field treatment. This additional processing considerably decreases hydrophobicity of the silicon wafer surface, thus favoring the subsequent formation of high-quality homogeneous sulfide films with good adhesion to the substrate. © *2001 MAIK "Nauka/Interperiodica".*

At present, the method of thin film deposition by spraying solutions containing the film components onto heated substrates (thermal spray coating technique) is intensively developed and widely applied [1, 2].

We have successfully used the spraying of solutions of thiocarbamide metal complexes for obtaining luminescent films of various metal sulfides on quartz glass plates and oxidized silicon wafers [3, 4]. The films were characterized by high adhesion to both quartz substrates and silicon wafers with a silicon dioxide surface layer. At the same time, we failed to obtain high-quality metal sulfide films on the surface of unoxidized silicon wafers because this surface is highly hydrophobic. This led to poor wetting of the silicon surface with sprayed solutions, which hindered the primary metal sulfide nucleation—a necessary point in thin film formation by the thermal spray deposition method.

Below, we will demonstrate that hydrophobicity of the crystal silicon surface can be reduced by treating the silicon wafers in a pulsed magnetic field. The wafers upon such pretreatment can be used for obtaining thin metal sulfide films by spraying aqueous solutions of the corresponding metal complexes.

The magnetic pretreatment of silicon wafers was effected by single-polarity triangular magnetic field pulses with an amplitude of $B = 0.6$ T, a duration of $\tau = 2 \times 10^{-5}$ s, and a repetition frequency of $t_0 = 2 \times 10^{-2}$ s. The experiments were performed with Czochralski grown silicon (Cz–Si) wafers pretreated in air at room temperature 48 h before the metal sulfide film deposition by the thermal spray coating method.

Thin films of metal sulfides (CdS, ZnS, and $Cd_xZn_{1-x}S$), both undoped and doped with luminescence activators (Cu, Ag, and Mn), were obtained by spraying aqueous solutions of neutral thiocarbamide complexes $Cd(N_2H_4CS)_2Cl_2$ and $Zn(N_2H_4CS)_2Cl_2$ (with or without additives of copper, silver, and manganese salts) onto magnetically pretreated silicon wafers. The substrate temperature during deposition was $T = 600$ K.

A comparison of the micrographs presented in Fig. 1 shows that the preliminary treatment of Cz–Si wafers in a pulsed magnetic field favors the formation
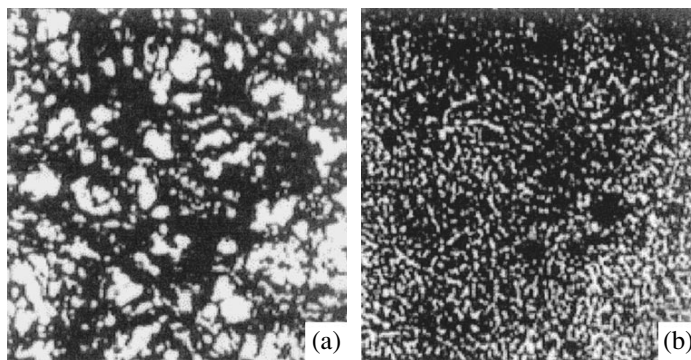

(a) (b)

Fig. 1. Micrographs of the initial stage of a CdS film formation on the surface of a silicon wafer (a) not treated in a magnetic field and (b) pretreated in a pulsed magnetic field 48 h before thermal spray coating application (magnification, ×5000).
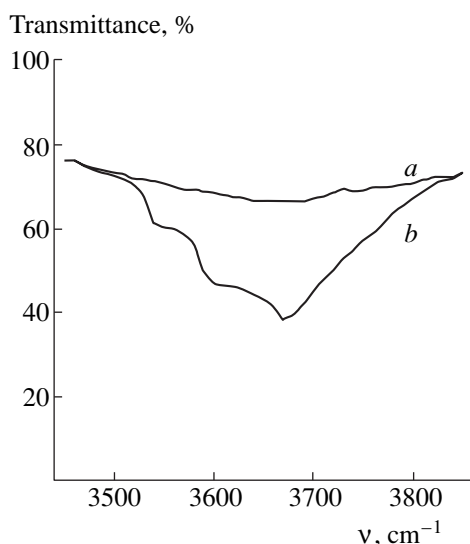
Transmittance, %

Fig. 2. IR absorption spectra of a silicon wafer (*a*) before and (*b*) 48 h after treatment in a pulsed magnetic field.
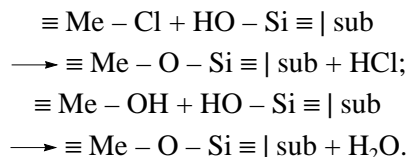
of more homogeneous films. This result can be explained by the increasing density of the primary metal sulfide nucleation centers on the Cz–Si crystal surface treated by the pulsed magnetic field.

Figure 2 shows the IR absorption spectra of silicon wafers, which demonstrate an increase in the intensity of light absorption in the spectral range from 3500 to 3800 cm^{-1}. As is known, the IR absorption in this region can be assigned to the surface hydroxyl (OH) groups [5]. This fact suggests that the observed variation in the IR absorption spectrum is related to an increase in the concentration of surface hydroxyl groups as a result of the atmospheric water adsorption on silicon enhanced by the pulsed magnetic field treatment. The increase in the adsorption properties of Cz–Si crystals treated by pulsed magnetic field can be explained as follows.

As is known, even short-time (a few seconds) exposure to relatively weak ($B < 1$ T) pulsed magnetic fields may induce long-term (hundreds of hours) changes in the microstructure of Cz–Si crystals, which are accompanied by structural rearrangements in the surface layers [6]. According to [6, 7], the effect of a pulsed magnetic field on the Cz–Si crystal microstructure is related to excitation of the Si–O bonds with interstitial oxygen, which results in that a certain fraction of these oxygen atoms leave their interstitial positions to form mobile oxygen–vacancy (O–V) centers. The deficit of vacancies in the bulk of silicon is compensated by the production of additional vacancies at the surface. The latter process is unavoidably accompanied by activation of

the adsorption processes. This may lead to a significant change in the physicochemical properties (including the wettability) of the surface of a silicon wafer treated in a pulsed magnetic field.

In accordance with the concepts developed in [8], the surface siloxane groups HO–Si $\equiv$ | sub ("sub" denotes the substrate) can be considered as the active centers for nucleation of the films deposited by thermal spraying of the aqueous solutions of metal thiocarbamide complexes. These solutions always contain mixed chloride and hydroxyl complexes responsible for the interaction with siloxane groups and for the subsequent growth of metal sulfide grains on the substrate surface according to the scheme

$$\equiv Me - Cl + HO - Si \equiv | \text{ sub}$$
$$\longrightarrow \equiv Me - O - Si \equiv | \text{ sub} + HCl;$$
$$\equiv Me - OH + HO - Si \equiv | \text{ sub}$$
$$\longrightarrow \equiv Me - O - Si \equiv | \text{ sub} + H_2O.$$

The oxygen bridges Me–O–Si formed in these reactions provide for a good adhesion of the sulfide film to a hydrophobic silicon substrate.

Thus, the pulsed magnetic field treatment of a Cz–Si crystal wafer leads to an increase in hydrophobicity of the silicon surface and allows a high-quality metal sulfide film to be obtained by spraying the corresponding aqueous solution. The effect of the semiconductor surface activation by a pulsed magnetic field considerably increases possibilities for obtaining various thin films by method of thermal spray coating.

REFERENCES

1. L. Pawlowski, *The Science and Engineering of Thermal Spray Coatings* (Wiley, Chichester, 1995).
2. H. Herman, S. Sampath, and R. McCune, MRS Bull. **25** (7), 17 (2000).
3. V. N. Semenov, V. G. Klyuev, M. A. Kushnir, *et al.*, Zh. Prikl. Spektrosk. **59** (1–2), 114 (1993).
4. V. N. Semenov, O. V. Ostapenko, and A. N. Lukin, Neorg. Mater. **36** (2), 160 (2000).
5. A. V. Kiselev and V. I. Lygin, *Infrared Spectra of Surface Compounds and Adsorbed Substances* (Nauka, Moscow, 1972).
6. M. N. Levin and B. A. Zon, Zh. Éksp. Teor. Fiz. **111** (4), 1373 (1997) [JETP **84**, 760 (1997)].
7. M. N. Levin and B. A. Zon, Phys. Lett. A **260**, 386 (1999).
8. V. N. Semenov and A. V. Naumov, Kondens. Sredy Mezhfazn. Gran. **1** (2), 176 (1999).

Translated by P. Pozdeev

Limiting Degree of Polarization of a Nonmonochromatic Radiation Propagating in a Fiber Guide with Random Inhomogeneities

G. B. Malykin, V. I. Pozdnyakova, and I. A. Shereshevskiĭ

Institute of Applied Physics, Russian Academy of Sciences, Nizhni Novgorod, Russia

Received July 12, 2000

Abstract—It is shown that the mean degree of polarization of a nonmonochromatic radiation propagating in a fiber guide with random inhomogeneities tends to zero as the fiber length tends to infinity. © *2001 MAIK "Nauka/Interperiodica"*.

The problem of evaluating the degree of polarization of a nonmonochromatic radiation propagating in a single-mode fiber guide is very important because optical fibers are finding an increasing application in various promising fields. The degree of polarization of a nonmonochromatic radiation accounts for the polarization sensitivity of interferometric fiber sensors used for the monitoring of various physical parameters. Examples are offered by ring fiber interferometers [1–6], in which the zero-level drift of the output interference signal is determined by the degree of polarization of a nonmonochromatic radiation. A difference of this characteristic from zero also leads to some undesirable phenomena in long fiber communication lines [7].

Different, sometimes rather contradictory assumptions concerning the limiting degree of polarization were made by various researchers [8–12]. The purpose of this study was to demonstrate that the mean degree of polarization of a nonmonochromatic radiation propagating in a fiber guide with random inhomogeneities tends to zero as the fiber length tends to infinity. The analysis is performed within the framework of a mathematical model of random inhomogeneities in a fiber guide, which was proposed in [12].

The mean square value of the degree of polarization of a nonmonochromatic radiation propagating in a fiber guide with random inhomogeneities is calculated based on the results obtained in [13], where it was demonstrated that the problem of finding the fiber-ensemble-mean value of the degree of polarization reduces to the problem of determining distributions (both individual and combined) of the random vectors $\mathbf{E}(\lambda, z)$ for the complex electric field amplitudes of the light wave for various wavelengths λ and for the case when the fiber length z tends to infinity. Note that, besides the random vector $\mathbf{E}(\lambda, z)$ describing the complex electric field amplitude at a point z in the fiber, we may also consider a random vector $\mathbf{E}_N(\lambda)$ describing the field at the output of a fiber composed of N random segments. It is natu-

rally assumed that the statistics of $\mathbf{E}_N(\lambda)$ for large N is close to the statistics of $\mathbf{E}(\lambda, N\langle l \rangle)$, where $\langle l \rangle$ is the mean length of the random fiber segments into which the total fiber is divided according to our model [12] (it should be noted that the rotation of anisotropy axes within each segment is constant).

A transition from the random vector $\mathbf{E}(\lambda, z)$ to $\mathbf{E}_N(\lambda)$ markedly simplifies the analysis. Validity of this transition was confirmed by a numerical experiment described in [15]. As was proved in [13], the distribution of a random complex vector $\mathbf{E}_N(\lambda)$ is uniform on a three-dimensional sphere as $N \longrightarrow \infty$ and the limiting combined distribution of two vectors $\mathbf{E}_N(\lambda_1)$ and $\mathbf{E}_N(\lambda_2)$ is completely determined by the individual distributions of each vector (because these vectors with $\lambda_1 \neq \lambda_2$ are independent). Below, we will demonstrate that a corollary of these two statements is the mean square value of the degree of polarization (and, hence, of the degree of polarization proper) for $N \longrightarrow \infty$ is zero.

The mean square value of the degree of polarization of a nonmonochromatic radiation propagating in a fiber guide is calculated by the formula [14]

$$\langle p_N^2 \rangle = 1 - \left\langle \frac{4 \det J_N}{\mathrm{tr}^2 J_N} \right\rangle. \tag{1}$$

Here, J_N is the coherency matrix of the nonmonochromatic radiation at the output of the fiber composed of N random segments:

$$J_N = \int J_N(\lambda) d\lambda = \int \mathbf{E}_N(\lambda) \mathbf{E}_N^\dagger(\lambda) d\lambda, \tag{2}$$

where † denotes Hermitian conjugate.

Let a nonmonochromatic radiation $\mathbf{E}_0(\lambda)$ entering the fiber be characterized by a spectral density function $B(\lambda) = \mathbf{E}_0^\dagger(\lambda) \mathbf{E}_0(\lambda)$. We will consider the case of no-loss fibers, for which the total radiation energy equal to

$\int B(\lambda)d\lambda$ is retained when the radiation is propagating in the fiber, so that we may take $\int B(\lambda)d\lambda = 1$. Within the framework of the model developed in [12], the radiation vectors at the input and output of the fiber composed of N random segments obey the relationship

$$\mathbf{E}_N(\lambda) = U_N(\lambda)\mathbf{E}_0(\lambda), \qquad (3)$$

where $U_N(\lambda)$ is a 2×2 unitary matrix (also called the Jones matrix). Using relationship, we may rewrite expression (2) as

$$J_N = \int U_N(\lambda)\mathbf{E}_0(\lambda)\mathbf{E}_0^\dagger(\lambda)U_N^\dagger(\lambda)d\lambda. \qquad (4)$$

Taking into account that the trace of the product of two matrices is independent of the factor order and that the matrix $U_N(\lambda)$ is unitary, we obtain from expression (4)

$$\begin{aligned} \mathrm{tr}J_N &= \int \mathrm{tr}(\mathbf{E}_0^\dagger(\lambda)U_N^\dagger(\lambda)U_N(\lambda)\mathbf{E}_0(\dot{\lambda}))d\lambda \\ &= \int B(\lambda)d\lambda = 1. \end{aligned} \qquad (5)$$

Thus, the trace of the coherency matrix at any point of the fiber is unity, irrespective of a particular distribution of inhomogeneities. Therefore, in order to determine the limiting mean square value of the degree of polarization of the nonmonochromatic radiation defined by formula (1), it is sufficient to calculate the mean determinant of the matrix J_N for $N \longrightarrow \infty$.

Let $\{\mathbf{e}_1, \mathbf{e}_2\}$ be an orthonormal basis set in the space of two-dimensional complex vectors. The trace and determinant of the matrix J_N can be written as

$$\mathrm{tr}J_N = (J_N\mathbf{e}_1, \mathbf{e}_1) + (J_N\mathbf{e}_2, \mathbf{e}_2), \qquad (6)$$

$$\det J_N = (J_N\mathbf{e}_1, \mathbf{e}_1)(J_N\mathbf{e}_2, \mathbf{e}_2) - |(J_N\mathbf{e}_2, \mathbf{e}_1)|^2. \qquad (7)$$

Evidently, the mean determinant $\langle \det J_N \rangle$ can be calculated if the $\langle (J_N\mathbf{s}, \mathbf{r})(J_N\mathbf{u}, \mathbf{v}) \rangle$ values are known for arbitrary vectors $\mathbf{s}, \mathbf{r}, \mathbf{u},$ and $\mathbf{v}$. Let us consider a bilinear form

$$(J_N\mathbf{s}, \mathbf{r}) = \int (\mathbf{s}, \mathbf{E}_N(\lambda))(\overline{\mathbf{r}, \mathbf{E}_N(\lambda)})d\lambda,$$

and find the corresponding limiting value.

By virtue of the $\mathbf{E}_N(\lambda)$ vector having a uniform distribution on a three-dimensional sphere with a radius $B(\lambda)$ for $N \longrightarrow \infty$, we obtain

$$\langle (J_\infty\mathbf{s}, \mathbf{r}) \rangle = \int B(\lambda)d\lambda \int_{s^3} (\mathbf{s}, \mathbf{v})(\overline{\mathbf{r}, \mathbf{v}})d\mathbf{v} = f(\mathbf{s}, \mathbf{r}),$$

where s^3 is the three-dimensional sphere of unit radius and f is some function of two vector arguments. As can readily be shown, the function f is invariant relative to an arbitrary rotation determined by the unitary matrix V, which implies that $f(V\mathbf{s}, V\mathbf{r}) = f(\mathbf{s}, \mathbf{r})$. It is also easy to show that the function f is linear with respect to the first

argument and antilinear with respect to the second argument.

Now we will show that $f(\mathbf{s}, \mathbf{r}) = \alpha(\mathbf{s}, \mathbf{r})$, where $\alpha = \mathrm{const}$. Fixing the first argument of the function f and using the property of linearity, we may write $f(\mathbf{s}, \mathbf{r}) = (g(\mathbf{s}), \mathbf{r})$, where $g(\mathbf{s})$ is a linear function represented by a square matrix $g(\mathbf{s}) = G\mathbf{s}$ in a vector space of finite dimensionality. Thus, $f(\mathbf{s}, \mathbf{r}) = (G\mathbf{s}, \mathbf{r})$. Using the property of invariance of the function f relative to a rotation determined by a unitary matrix V, we obtain $(GV\mathbf{s}, V\mathbf{r}) = (V^\dagger GV\mathbf{s}, \mathbf{r}) = (G\mathbf{s}, \mathbf{r})$, so that $G = V^\dagger GV$ for any unitary matrix V. By virtue of the Schur lemma [16], all eigenvalues of the matrix G possessing this property are the same, so that $G = \alpha E$, where E is the unit matrix. Thus, we have proved that $\langle (J_\infty\mathbf{s}, \mathbf{r}) \rangle = \alpha(\mathbf{s}, \mathbf{r})$, where $\alpha = \mathrm{const}$. In order to determine this constant, let us calculate the limiting mean value of the trace of the coherence matrix. Using formula (6), we obtain $\langle \mathrm{tr}J_\infty \rangle = 2\alpha$; at the same time, Eq. (5) yields $\mathrm{tr}J_\infty = \mathrm{tr}J_0 = 1$. Comparing these results, we find $\alpha = 1/2$ and

$$\langle (J_\infty\mathbf{s}, \mathbf{r}) \rangle = \frac{1}{2}(\mathbf{s}, \mathbf{r}). \qquad (8)$$

Now let us determine the limiting value $\langle (J_\infty\mathbf{s}, \mathbf{r})(J_\infty\mathbf{u}, \mathbf{v}) \rangle$. The product of two bilinear forms is

$$\begin{aligned} (J_N\mathbf{s}, \mathbf{r})(J_N\mathbf{u}, \mathbf{v}) &= \iint (\mathbf{s}, \mathbf{E}_N(\lambda_1))(\overline{\mathbf{r}, \mathbf{E}_N(\lambda_1)}) \\ &\times (\mathbf{u}, \mathbf{E}_N(\lambda_2))(\overline{\mathbf{v}, \mathbf{E}_N(\lambda_2)})d\lambda_1 d\lambda_2. \end{aligned}$$

Since the vectors $\mathbf{E}_N(\lambda_1)$ and $\mathbf{E}_N(\lambda_2)$ are independent for $N \longrightarrow \infty$ and their limiting distributions are uniform, we obtain

$$\langle (J_\infty\mathbf{s}, \mathbf{r})(J_\infty\mathbf{u}, \mathbf{v}) \rangle = \iint B(\lambda_1)B(\lambda_2)d\lambda_1 d\lambda_2$$

$$\times \iint_{s^3 s^3} (\mathbf{s}, \mathbf{v})(\overline{\mathbf{r}, \mathbf{v}})(\mathbf{u}, \boldsymbol{\eta})(\overline{\mathbf{u}, \boldsymbol{\eta}})d\mathbf{v}d\boldsymbol{\eta} = \left(\int B(\lambda)d\lambda\right)^2$$

$$\times \int_{s^3} (\mathbf{s}, \mathbf{v})(\overline{\mathbf{r}, \mathbf{v}})d\mathbf{v} \int_{s^3} (\mathbf{u}, \mathbf{v})(\overline{\mathbf{v}, \mathbf{v}})d\mathbf{v} = \frac{1}{4}(\mathbf{s}, \mathbf{r})(\mathbf{u}, \mathbf{v}).$$

Substituting this result into Eq. (7) and taking into account that the vectors $\mathbf{e}_1, \mathbf{e}_2$ are orthonormal, we obtain $\langle \det J_\infty \rangle = 1/4$. Thus, Eq. (1) yields $\langle p_\infty^2 \rangle = 0$; since $\langle p_\infty \rangle \leq \sqrt{\langle p_\infty^2 \rangle}$, it is necessary that $\langle p_\infty \rangle = 0$ as well.

A more thorough analysis [13, 17] shows that the tendency of the mean square degree of polarization to zero at large fiber lengths z is well approximated by the asymptotic formula

$$\langle p^2(z) \rangle \approx \frac{\mathrm{const}}{\sqrt{z}}.$$

Unfortunately, the residual term of this formula (depending on the fiber parameters) cannot be described by a simple analytical expression.

REFERENCES

1. W. K. Burns and R. P. Moeller, J. Lightwave Technol. **LT-2** (4), 430 (1984).

2. S. M. Kozel, V. N. Listvin, S. V. Shatalin, and R. V. Yush-kaĭtis, Opt. Spektrosk. **61** (6), 1259 (1986) [Opt. Spectrosc. **61**, 814 (1986)].

3. G. B. Malykin, Izv. Vyssh. Uchebn. Zaved., Radiofiz. **34** (7), 817 (1991).

4. G. B. Malykin, I. M. Nefedov, and I. A. Shereshevskiĭ, Izv. Vyssh. Uchebn. Zaved., Radiofiz. **37** (11), 1437 (1994).

5. G. B. Malykin and V. I. Pozdnyakova, Opt. Spektrosk. **84** (1), 145 (1998) [Opt. Spectrosc. **84**, 131 (1998)].

6. G. B. Malykin and V. I. Pozdnyakova, Opt. Spektrosk. **86** (3), 513 (1999) [Opt. Spectrosc. **86**, 451 (1999)].

7. C. D. Poole, Opt. Lett. **13** (8), 687 (1988).

8. W. K. Burns, R. P. Moeller, and C. L. Chen, J. Lightwave Technol. **LT-1** (1), 44 (1983).

9. A. N. Zalogin, S. M. Kozel, and V. N. Listvin, Izv. Vyssh. Uchebn. Zaved., Radiofiz. **29** (2), 243 (1986).

10. G. B. Malykin, Izv. Vyssh. Uchebn. Zaved., Radiofiz. **35** (11–12), 993 (1992).

11. G. B. Malykin, I. M. Nefedov, and I. A. Shereshevskiĭ, Izv. Vyssh. Uchebn. Zaved., Radiofiz. **37** (10), 1311 (1994).

12. G. B. Malykin, V. I. Pozdnyakova, and I. A. Shereshevskiĭ, Opt. Spektrosk. **83** (5), 843 (1997) [Opt. Spectrosc. **83**, 780 (1997)].

13. G. B. Malykin, V. I. Pozdnyakova, and I. A. Shereshevskiĭ, Preprint No. 528, IPF RAN (Institute of Applied Physics, Russian Academy of Sciences, Nizhni Novgorod, 2000).

14. L. Mandel and E. Wolf, *Optical Coherence and Quantum Optics* (Cambridge Univ. Press, Cambridge, 1995).

15. G. B. Malykin, V. I. Pozdnyakova, and I. A. Shereshevskiĭ, Opt. Spektrosk. **88** (3), 477 (2000) [Opt. Spectrosc. **88**, 427 (2000)].

16. A. Barut and R. Raczka, *Theory of Group Representations and Applications* (PWN–Polish Scientific Publishers, Warsaw, 1977; Mir, Moscow, 1980), Vols. 1, 2.

17. S. C. Rashleigh, J. Lightwave Technol. **LT-1** (2), 312 (1983).

Translated by P. Pozdeev

A Physical Model of the Short Glow Discharge
in Plasma Display Panels

A. A. Kudryavtsev* and L. D. Tsendin**

* St. Petersburg State University, St. Petersburg, Russia
e-mail: akud@ak2138.spb.edu
** St. Petersburg State Technical University, St. Petersburg, Russia
Received November 15, 2000

Abstract—It is shown that plasma display panel (PDP) cells are usually featuring a short glow discharge without positive column. An adequate description of this discharge must be consistently kinetic, taking into account the nonlocal effects for both fast and plasma electrons. Models combining elements of different precision, for example, local field approximation for fast electrons and various hydrodynamic (fluid) models for slow plasma electrons, cannot provide for a correct analysis of the discharge processes in PDPs. © *2001 MAIK "Nauka/Interperiodica".*

An important, still comparatively new technological application of gas discharges is related to plasma display panels (PDPs), offering a most promising means of creating the next generation of high-resolution flat monitors [1].

The interelectrode gap in every unit cell of a PDP is separated by two parallel glass plates with a characteristic distance of 100 μm. In order to increase the secondary electron emission coefficient, the electrodes are coated with a dielectric layer of MgO. The gas mixture contained in the cells at a pressure p of about 500 Torr comprises a buffer gas (He or Ne) facilitating the breakdown with a small additive (a few percent) of Xe producing the useful UV radiation. Upon application of the voltage pulses with an amplitude of 150–400 V and a frequency of 50–100 kHz, the PDP cells are featuring microdischarges with a characteristic duration of 100 ns. Small unit cell dimensions and a short lifetime of the active discharge stage makes the discharge diagnostics an in this system an extremely difficult task. The main effort of researchers is devoted to elucidating the principal mechanisms responsible for excitation of the radiative states and developing simple and effective methods for calculating the PDP parameters depending on the particular conditions [2–11].

At present, the radiation efficiency of discharge achieved in the unit cells of PDPs is rather low, not exceeding several percent. This is the main factor restricting the wide use of PDPs. A certain ground for optimism is provided by the fact that the pL values for microdischarges in PDPs are typical of the glow discharge [12], which implies a profound analogy with discharges in luminescent tubes where the efficiency exceeds 10% [13].

As is known (see, e.g., [12]), a glow discharge contains two principal luminescent regions: positive column (PC) and negative glow (NG). In the PC region, which is independent of the electrode processes, the excitation and ionization is produced by the local electric field. This circumstance allows most of the power supplied to PC to be converted into radiation, provided that the discharge conditions are properly selected [12, 13]. In contrast, the NG plasma is related to the cathode discharge region and is formed by an "external" ionizing factor—the electron beam coming from the cathode fall (CF) region. The efficiency of the existing luminescent lamps employing NG usually does not exceed η = 10–15% [13], which is smaller than the efficiency of the lamps with PC but still higher than that of the existing PDPs. The physical mechanisms involved in the formation of PC and NG (and, hence, the models used for their description) are essentially different. Therefore, an analysis of the PDP operation and a search for the ways of optimization of its parameters must begin with elucidating the type of the principal emitting region.

Below, we will demonstrate that a microdischarge in PDP represents a short glow discharge without positive column, the description of which must be consistently kinetic, taking into account the nonlocal effects for both fast and plasma electrons. In the estimates, we will use data for helium, which is better characterized as the buffer gas. However, all conclusions are applicable to neon as well.

Since the pL in PDPs is about 5 cm Torr, the breakdown voltage corresponds to the right-hand branch of the Paschen curve (near its minimum). In the luminescence stage, this voltage corresponds to the normal cathode fall values and is typically within the interval from 150 to 400 V. The emission takes place in the glow discharge stage, the spatial structure of which comprises the following regions [12]. A strong electric field

drops linearly in the cathode fall (CF) region, a typical length of which for helium is 1.3–1.4 cm Torr. This region is sharply separated from the region of negative glow (NG) plasma gradually passing to the Faraday dark space (FDS). This region is followed by a homogeneous or striated positive column (PC).

A quasineutral plasma region includes PC, FDS, and partly the NG and anode regions. The electric field strength, which is homogeneous in PC (in the absence of striations), decreases (and even changes sign) in the NG region. The field sign in the anode region may vary. The cathode region (responsible for the independent discharge) includes all the aforementioned regions except PC and extends up to the anode in the case of a short glow discharge (where PC is missing). It should be emphasized that PC is not a necessary part of the discharge: this region exists independently of the others and appears only provided that the interelectrode gap is long enough to accommodate all the above regions.

The length of the NG region, in which excitation of the electron states takes place, is determined by the range l_N of fastest electrons possessing an energy equal to the cathode potential fall value eU_k [14, 16]:

$$l_N = \int_0^{eU_k} dw/(NF(w)), \qquad (1)$$

where w is the kinetic energy and $NF(w)$ is the stopping power (loss function). Using an approximation $F(w) = F_0 = 1.5 \times 10^{-15}$ eV cm^2 proposed for the discharge in helium [14], we obtain from Eq. (1) an estimate $pl_N = 0.02eU_k$ (cm Torr for U_k expressed in volts). It was shown that these estimates are consistent with experiments [14, 17]. Thus, the characteristic values of $pl_N = $ 3–6 cm Torr obtained for a typical cathode potential fall of $U_k = 150$–300 V indicate that the NG length is comparable with the PDP unit cell size.

The plasma density profile, corresponding to slow plasma electrons, is determined by the ambipolar diffusion equation

$$D_a \Delta n + Z(x) - \beta n^2 = 0, \qquad (2)$$

where D_a is the ambipolar diffusion coefficient, β is the recombination coefficient, and $Z(x)$ is the nonlocal ionization source profile. The point with $x = x_1 \approx l_N$ corresponding to the maximum density n_m is close to the boundary between NG and FDS regions.

The region with $x > l_N$ corresponds to FDS where $Z(x) = 0$ and the plasma density in PC drops sharply (because of the ion loss) to the value $n_c \ll n_m$. According to Eq. (2), a characteristic FDS length is $l_F = \sqrt{6D_a/\beta n_c}$ [14, 17]. The diffusion coefficients of He$_2^+$ and Xe$_2^+$ ions in He are close and can be estimated as $D_a \approx 325T_e/pT$ (cm^2/s), where T_e is the electron temperature; the dissociative recombination coefficient for

Xe$_2$ is $\beta \approx 10^{-6}(T/T_e)^{1/2}$ (cm^3/s) [12]. Using these values, we obtain the following estimate for the He–Xe gas mixture: $pl_F \approx 10^{-4}(T_e/T)^{1/4}(N/n_c)^{1/2}$ (cm Torr), where N is the gas density. Since the plasma density in PC is one–two orders of magnitude lower than that in NG (see, e.g., [12]), the degree of ionization in PC under typical PDP conditions is $n_c/N < 10^{-6}$–10^{-8}. This yields an estimate of $pl_F \sim 1$ cm Torr, so that the total effective length of NG and FDS is $pl_N + pl_F \sim pL$.

Taking into account that, in the field corresponding to PC, electrons acquire an energy exceeding the ionization potential only upon traveling a distance equal to the energy relaxation length λ_ε (see Eq. (5) below), we may conclude that the PDP discharge length is insufficient for the PC formation. Based on a detailed analysis of the short glow discharge without PC, which was performed in [14] (see also [15–17]), we may note the following important features.

Ionization in the cathode region exhibits a nonlocal character, since a considerable fraction of the ionization events is performed by fast electrons in the plasma, where the field is virtually absent. Therefore, the local field approximation (LFA) and the Townsend ionization coefficient $\alpha(E/p)$ are inapplicable. These approximations are essentially incapable of correctly describing the ionization in NG and determining the NG length [14–20]. The behavior of fast electrons in the plasma region must be described by the Monte Carlo method or in terms of nonlocal kinetic models.

Let us turn to considering slow electrons. Within the framework of the hydrodynamic (fluid) approximation, the total field in an inhomogeneous plasma is described by the following relationship [12]:

$$E = \frac{j}{en\mu_e} - \frac{T_e}{e}\frac{\nabla n}{n} - \frac{D_{Te}}{\mu_e}\nabla T_e, \qquad (3)$$

where D_{Te} is the electron thermodiffusion coefficient; the ion contribution to the total current is negligible. In other words, the quasilinearity of the inhomogeneous plasma with current is maintained by the field of two types: a current field ensuring the charge transport and a diffusion field compensating for the diffusion and thermodiffusion electron fluxes (two last terms in the right-hand part of Eq. (3)). If the current field dominates, the work performed by this field heats the electrons. When the field strength is sufficiently large and determines the average electron energy, the electron energy relaxation length is $T_e/(eE)$.

If the inhomogeneity scale is smaller than the energy relaxation length $T_e/(eE)$, the potential profile is determined by the condition of compensation of the electron diffusion and thermodiffusion. In the case of a spatially homogeneous T_e, the potential profile corresponds to the Boltzmann electron distribution

$$e\varphi(x) = -T_e \ln(n/n_m). \qquad (4)$$

This field does not heat electrons, and there is no relationship between the electron temperature and the field strength. The field retarding the electron flow even "cools" the electrons. If the density gradient in this region is sufficiently large, which is typical of NG and FDS, the resulting current is described by a difference of two large terms in the right-hand part of Eq (3).

The position of the point $x_1 \approx l_N$ is close to the boundary between NG and FDS regions and to the maximum of electron density n_m. At this point, the diffusion field strength given by Eq. (4) changes sign in order to compensate for the electron diffusion. Ions formed in the region of $x > x_1$ move toward the anode, while those formed at $x < x_1$ return to the cathode. Since the T_e value is small (see below), from Eq. (4) follows a sharp boundary (narrow transition region) between the NG plasma and the CF layer [14]. The reversal of the electric field vector at $x = x_1$ corresponds to the formation of a potential well for electrons. At $x = x_2$, where the plasma density according to Eq. (2) decreases to n_c, the diffusion loss of plasma has to be compensated by the ionization and the field vector has to be directed toward the cathode again. Therefore, the second point of the field reversal appears, which roughly corresponds to the beginning of PC.

Thus, in order to calculate the field strength profiles and determine the reversal points, it is necessary to know the spatial distribution $Z(x)$ of nonlocal ionization sources and the electron temperature profile $T_e(x)$. This, in turn, requires the knowledge of the nonlocal distribution of fast electrons in the cathode region, which cannot be determined within the framework of the LFA [14, 15]. Should it be possible to describe the electrons within the framework of the hydrodynamic (fluid) model assigning them a common density, directed velocity, and temperature (average energy), then we would complement this system by an equation for $T_e(x)$ and a relationship between the ionization rate and $T_e(x)$ to obtain a closed system of equations describing the discharge. However, this can be done only provided that there is an intense energy exchange (mixing), primarily between electrons trapped in the well and the transit electrons.

As was demonstrated in [14, 15], the applicability criterion of the fluid model demands the spatial and temporal scales of the problem to exceed the energy relaxation length λ_ε and time τ_ε:

$$\lambda_\varepsilon = \sqrt{2D\tau_\varepsilon}, \quad \tau_\varepsilon = 1/(\nu_e + \delta\nu_a), \qquad (5)$$

where ν_e and ν_a are the frequencies of the electron–electron and elastic electron–atom collisions, respectively; $D = V\lambda/3$ is the coefficient of free electron diffusion; and $\delta = 2m/M$. Under the typical PDP operation conditions, the degree of ionization is $nN < 10^{-5}$, so that $\nu_e < \delta\nu_a$ and $\lambda_\varepsilon = \lambda/\sqrt{\delta} \approx 100\lambda$. Taking the estimate from above, we conclude that for helium (and the more so for neon) $\lambda_\varepsilon p > pL$, which implies that the discharge

gap length in PDP is small as compared to the energy relaxation length of the plasma electron for quasielastic collisions. In this case, the plasma electron distribution function is also nonlocal and depends on their total energy $\varepsilon = w + e\varphi(x)$. Thus, the description for these electrons, as well as for the fast ones, must be kinetic. Since the electrons with a given energy ε obeying relationships (5) behave virtually independently of all others (this requires that the electron–electron collisions are rare, $\nu_e < \delta\nu_a$), it is convenient to separate the plasma electrons into two groups, including intermediate and slow (trapped) electrons [14, 15].

The total energy of the intermediate electrons ($\varepsilon_1 > \varepsilon > e\varphi_t$, where φ_t is the potential of the anode or the second field reversal point x_2) which transfer the electron current in FDS is conserved over a length equal to λ_ε. If the λ_ε value for the intermediate electrons is greater than the interelectrode distance L (or than x_2), these electrons freely reach the anode (or the second field reversal point x_2, in which case they produce ionization in PC [14, 15]). The distribution function of the intermediate electrons is determined by their production described by the source function $Q(x, \varepsilon)$ and by the loss as a result of the spatial diffusion and inelastic collisions [14, 20]. The intermediate electron density n_s and the current density j_s can be evaluated by the formulas

$$n_s(x) \sim Q(x)\tau_f, \quad j_s \sim D(\varepsilon_s)dn_s/dx, \qquad (6)$$

where $\tau_f \sim L^2/D$. The source Q is determined by the ionization, superelastic collisions, and Penning ionization [14, 21].

The slow electrons with $\varepsilon < e\varphi_t$ are trapped in the potential well and can move only within the corresponding limits. Since these electrons do not participate in the current transfer, they are not heated by field due to the Joule mechanism. A strong electron–electron interaction at thermal energies results in the establishing of a Maxwell–Boltzmann distribution (see Eq. (4)), whereby the slow electron density varies with the coordinate as

$$n(x) = n_m[\exp(-e\varphi(x)/T_e) - \exp(-e\varphi_t/T_e)] \quad (7)$$

and is zero for $x > x_2$. The temperature T_e of the trapped electrons is small, spatially homogeneous, and dependent on the integral energy balance determined by heating in collisions with intermediate electrons (possessing a characteristic energy $\sim\varepsilon_1$) and cooling in collisions with neutral particles.

The knowledge of T_e is important for calculating the potential profile and the rates of ambipolar diffusion, recombination, stepwise excitation, and some other important processes. In the balance equation for T_e, a term corresponding to the heating can be approximated by $H_Q = Q\varepsilon_{\text{eff}}$, where ε_{eff} is the effective energy transferred to the slow electrons during their collisions with the intermediate ones (formed as a result of oper-

ation of the source Q). This effective energy can be estimated as

$$\varepsilon_{\text{eff}} \sim \varepsilon_1 \nu_e / (\nu_e + \delta\nu_a + 1/\tau_f) \qquad (8)$$

(for details, see [21, 22]). As seen from this relationship, the ε_{eff} value may vary within broad limits depending on the particular conditions: from $\varepsilon_{\text{eff}} \sim \varepsilon_1$ in a local regime (for $\nu_e > \delta\nu_a$) to very small values $\varepsilon_{\text{eff}} \ll \varepsilon_1$ in a nonlocal case. Accordingly, the temperature T_e of the trapped electrons varies in a wide range as well, from a few electronvolts to room temperature. Since the H_Q determination requires the knowledge of the distribution of fast and intermediate electrons, the calculation of T_e is a kinetic problem.

The $T_e(x)$ profiles obtained within the framework of the hydrodynamic (fluid) model calculation based on the integral energy balance for all intermediate and fast electrons may lead to the densities and the excitation rates of spectral lies absolutely different from real values. However, a comparison of the parameters determined from the integral balance using the known characteristics may create an illusion of satisfactory agreement. A well-known example is offered by PC, in which the ionization rate is equal to the rate of ambipolar diffusion loss known to a sufficiently good precision. Using this relationship, we may evaluate T_e for any electron distribution—including the definitely inadequate cases, for example, of the Maxwell distribution. However, an attempt at using this "electron temperature" and the Maxwell distribution function to calculate the other parameters, such as the excitation rates of various levels, will lead to very large errors.

The electron current in the CF region is transferred by fast electrons. In the NG plasma, the fast-electron current is transformed (over a distance of $d < x < x_1$) into the current j_s (see Eq. (6)) of intermediate electrons, the concentration of which is markedly greater than that of the fast electrons [14, 15]. The electron density in the NG plasma and FDS is determined primarily by the Maxwell–Boltzmann distribution of trapped electrons (given by Eq. (7)) with low T_e, which do not contribute to the current. For this reason, the NG and FDS regions obey the Boltzmann relationship between the potential and the temperature of the trapped electrons. In the traditional hydrodynamic (fluid) approximation, the current of slow electrons is separated into diffusion and drift components (see Eq. (3)). However, the average energies and densities of the trapped and transit intermediate electrons vary along the NG and FDS regions in the absolutely different manner (see Eqs. (6) and (7), for more details see [14, 15]).

In FDS, where neither ionization sources nor the sources of intermediate electrons are present, the densities of both trapped and intermediate electrons fall monotonically but in accordance with different laws. The electron current, which is transferred only by inter-

mediate electrons, principally cannot be expressed through the total electron concentration and its derivative. Any attempts at introducing the thermodiffusion component and/or variable electron temperature (average energy) cannot improve the situation either [14]. We also cannot expect any success from the hybrid models combining elements of different precision, for example, LFA approximation for fast electrons and hydrodynamic (fluid) model for nonlocal slow plasma electrons. This may only give rise to an illusion of accuracy, while the final error is determined by that of the least known quantity.

When the FDS length l_F becomes comparable with the energy relaxation length λ_ε for the intermediate electrons, the nonlocal character of their distribution function may lead to the following effects [14]. The energy of the moving intermediate electrons, which decreases as a result of degradation by elastic collisions, may become considerable lower than ε_1 in the region of the second field reversal point. In this case, the pattern of ionization in the transition region between FDS and PC will be periodic with respect to the potential $e\varphi$, with the period equal to ε_1. This spatially periodic ionization source may give rise to oscillations in the electric field strength and electron density distributions and, hence, lead to the PC striations. It was pointed out [14] that this effect is also possible for $\lambda_\varepsilon \gg l_F$, since the source Q of the intermediate electrons is energetically inhomogeneous. Note that discharge striations were in fact observed in some experiments with PDPs [23]. We believe that this effect is related to the nonlocal properties of electrons in FDS and in the region of discharge transition to PC [14, 15].

It should be recalled that the electric field strength E in the discharge plasma always varies so as to provide that the electroneutrality condition would be fulfilled during the motion of charged particles (the electroneutrality condition is used for determining E). Using the Poisson equation, which is automatically satisfied, we can determine (if necessary) the small difference $\Delta n = n_i - n_e \sim n(r_D/L)^2$. Taking into account this small term in the equations for ions and electrons, we may establish that the additional (to the quasineutral value E) field is on the order of $\Delta E \sim E(\Delta n/n)$, while the accuracy of the field strength determination in the plasma approximation is $\sim (r_D/L)^4$. Therefore, the Poisson equation can be used for determining the field in the plasma only provided that the computational facilities allow this accuracy to be improved for the other elements as well. In other words, use of the Poisson equation instead of the usual plasma approximation is only expedient when all the other characteristics can be calculated to within the uncertainty smaller than $(r_D/L)^4$. This means that the calculation scheme must be "equiprecision": as noted above, the reliability of the results is eventually determined by the least known parameter; otherwise, we have only an illusion of accuracy.

Thus, the PDP features a short glow discharge without positive column and, hence, the ways to optimization of the luminescence characteristics are determined primarily by the behavior of fast electrons. A correct description of such a discharge must be consistently kinetic, taking into account the nonlocal effects for both fast and plasma electrons. We believe that an adequate physical model of this discharge must include (for details, see [14]) the following points: (i) determination of a sharp boundary between various spatial and energy regions controlled by different processes; (ii) subdivision of the discharge space into electrode layer and plasma and use of the Poisson equation only for determining the field in the cathode and anode layers; (iii) a hydrodynamic (fluid) description of ions and the self-consistent field profile determination in the plasma; and (iv) a kinetic description of electrons subdivided (in accordance with their functions) into three groups: fast, intermediate, and trapped. The fast electrons are expediently described by the Monte Carlo method of in terms of nonlocal kinetic models; the intermediate electrons obey a kinetic equation in a two-term approximation; and the trapped electrons conform to the Maxwell–Boltzmann distribution, with the temperature determined by kinetic methods.

REFERENCES

1. A. Sobel, IEEE Trans. Plasma Sci. **19**, 1032 (1991).

2. R. B. Campbell, R. Veerasingam, and R. T. McGrath, IEEE Trans. Plasma Sci. **23**, 698 (1995).

3. R. Veerasingam, R. B. Campbell, and R. T. McGrath, Plasma Sources Sci. Technol. **6**, 157 (1997).

4. P. J. Drallos, V. P. Nagorny, and W. Williamson, Plasma Sources Sci. Technol. **4**, 576 (1995).

5. J. Meunier, Ph. Belenguer, and J. P. Boeuf, J. Appl. Phys. **78**, 731 (1995).

6. J. P. Boeuf, C. Punset, A. Hirech, and H. Doyeux, J. Phys. IV **7**, C4-3 (1997).

7. Th. Callegari, R. Ganter, and J. P. Boeuf, J. Appl. Phys. **88**, 3905 (2000).

8. A. Oda, Y. Sakai, H. Akashi, and H. Sugawara, J. Phys. D **32**, 2726 (1999).

9. H. S. Jeong, B. J. Shin, and K. W. Whang, IEEE Trans. Plasma Sci. **27**, 171 (1999).

10. Y. Ikeda, J. P. Verboncoeur, P. J. Christenson, and C. K. Birdsall, J. Appl. Phys. **86**, 2431 (1999).

11. S. Rauf and M. J. Kushner, J. Appl. Phys. **85**, 3460 (1999).

12. Yu. Raizer, *Gas Discharge Physics* (Springer-Verlag, Berlin, 1991).

13. J. E. Waymouth, *Electric Discharge Lamps* (MIT Press, Cambridge, 1971).

14. V. I. Kolobov and L. D. Tsendin, Phys. Rev. A **46**, 7837 (1992).

15. L. D. Tsendin, Plasma Sources Sci. Technol. **4**, 200 (1995).

16. Yu. P. Raĭzer and M. N. Shneĭder, Teplofiz. Vys. Temp. **29**, 1041 (1991).

17. Yu. P. Raĭzer and M. N. Shneĭder, Teplofiz. Vys. Temp. **35**, 19 (1997).

18. T. J. Sommerer, W. N. G. Hitchon, and J. E. Lawler, Phys. Rev. A **39**, 6356 (1989).

19. J. P. Boeuf, *Physics and Applications of Pseudosparks,* Ed. by M. A. Gunderson and G. Shaefer (Plenum, New York, 1989), p. 255.

20. M. Surendra, D. B. Graves, and G. M. Jellum, Phys. Rev. A **41**, 1112 (1990).

21. R. R. Arslanbekov and A. A. Kudryavtsev, *Electron Kinetics and Applications of Glow Discharges*, Ed. by U. Kortshagen and L. D. Tsendin (Plenum, New York, 1998), p. 161.

22. R. R. Arslanbekov and A. A. Kudryavtsev, Phys. Plasmas **6**, 1003 (1999).

23. G. Cho, E. H. Choi, V. G. Kim, and D. Kim, J. Appl. Phys. **87**, 4113 (2000).

Translated by P. Pozdeev

An S-Band Vircator with Premodulated Electron Beam Based on a Compact Generator with Inductive Energy Storage

A. M. Efremov, A. A. Zherlitsyn, S. A. Kitsanov, A. I. Klimov,
S. D. Korovin, B. M. Koval'chuk, I. K. Kurkan, O. P. Kutenkov,
S. V. Loginov, I. V. Pegel', and S. D. Polevin

Institute of High Current Electronics, Siberian Division, Russian Academy of Sciences, Tomsk, Russia
e-mail: polevin@lfe.hcei.tsc.ru
Received October 20, 2000

Abstract—An experimental S-band vircator with premodulated electron beam based on a compact generator with inductive energy storage is described. The vircator radiation power was 300 MW at a power efficiency of about 5% and a pulse duration of 50 ns. The oscillation frequency, determined by the electrodynamic system parameters, remained unchanged during the pulse. © *2001 MAIK "Nauka/Interperiodica".*

The idea of combining the electrodynamic feedback with virtual cathode was suggested in the 1970s [1]. Subsequent investigations showed [2, 3] that a vircator with feedback and premodulated electron beam can effectively operate at a current exceeding the critical level only by 20–30%. This system, in contrast to the usual vircators operating at a current exceeding the critical value by a factor of 2–3, ensures a higher efficiency of generation, the possibility of operating in a single-mode regime, a higher frequency stability, and the feasibility of controlling the frequency by changing the resonator parameters. The results of a three-dimensional modeling performed using a completely electromagnetic KARAT PIC-code confirmed the possibility of implementing an S-band vircator with premodulated electron beam possessing the efficiency above 10% and a possibility of the relative frequency band variation within 20% at half maximum power.

Below, we report on the results of experimental investigation of an S-band vircator with premodulated electron beam developed within the framework of this concept. Until now, the experiments with vircators [4] were carried out for the most part using cumbersome and expensive accelerators based on the Marx generator. The purpose of our work was to construct an experimental S-band vircator based on a compact generator with inductive energy storage.

Figure 1 shows a schematic diagram of the experimental S-band vircator with premodulated electron beam. The electron beam was generated in a planar vacuum diode *1* without external focusing magnetic field and transported through a modulator *2* and energy take-off *3* sections provided with tungsten grid windows (geometric transparency, about 0.95). Sections *2* and *3* represented rectangular waveguide segments electrodynamically coupled by a rectangular coupling hole. By changing the position and size of the coupling hole and the position of plunger *4*, it was possible to adjust the electrodynamic system of the vircator to an optimum regime and to a desired working frequency. By the results of numerical modeling, the optimum length of the modulator and energy take-off sections were
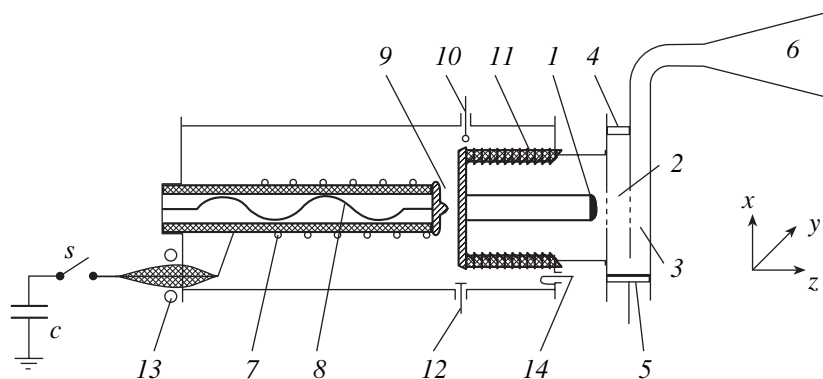

Fig. 1. A schematic diagram of the experimental S-band vircator with premodulated electron beam. See the text for explanations.
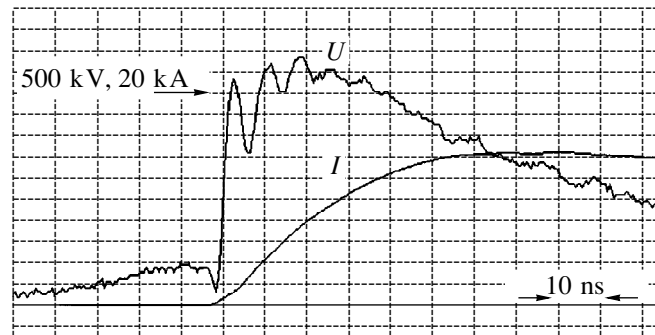
Fig. 2. Typical oscillograms of the cathode voltage and beam current in the vircator.

$\approx \lambda/5$ and $\approx \lambda/2$, respectively, where λ is the radiation wavelength.

A maximum power was achieved at a diode current 20–30% above the critical value for the energy take-off section. Upon the virtual cathode formation, a lowest TE_{10} mode of the rectangular waveguide was excited in the electrodynamic system and radiated to the free space via a rectangular horn antenna *6*. The vircator radiation power was either determined by summing over the radiation pattern with the aid of calibrated dipoles or measured with the aid of a 60-dB coupler built into the output waveguide tract of the vircator. The signals from the antenna and the coupler were registered by a fast oscilloscope of the HP54720D type.

The electron beam was formed with the aid of a metal–dielectric explosive emission cathode possessing an emitting surface diameter of 55 mm. The voltage was applied to the diode from a generator with an inductive energy storage and an electrically exploded wire current opening switch [5]. The generator (Fig. 1), mounted in the chamber filled with a mixture of nitrogen and elegas to a total pressure of 6 atm, comprised a storage inductance *7*, current opening switch *8*, sharpening *9* and cutting *10* dischargers, and a sectioned feedthrough insulator *11*. The current opening switch was composed of 36 parallel copper conductors, each with a diameter of 71 μm and a length of 80 cm. The working medium in the opening switch was air at atmospheric pressure. The output pulse shape could be corrected by changing gap widths in the sharpening and crowbar switch.

The storage capacitor with a capacitance of $C \approx 4\ \mu F$ was charged up to 70 kV and then switched, with the aid of a multigap five-channel gas switch *S* [6], to serially connected inductance $L \approx 4.6\ \mu H$ and the current opening switch. The amplitude of the short-circuit current in the generator was ~65 kA at a quarter-period of oscillations ~6.6 μs. The opening switch operated ~4.5 μs after the current flow onset. The rising voltage (~500 kV) produced breakdown in the peaking switch, which connected the storage inductance to the vacuum diode. The cathode voltage was monitored by a capacitive probe *12* [7], and currents in the storage inductance and diode were measured using the Rogowski coil *13* and the magnetic loop *14*, respectively.

In our experiments, the vircator was tuned to the maximum efficiency regime and adjusted at a desired frequency by changing the distance between anode and cathode and the electrodynamic system parameters. For an anode–cathode spacing of 15 mm, the microwave output power reached 300 MW at a frequency of 2.65 GHz. The generator power efficiency was about 5% and the microwave pulse duration at the half maximum power level was about 50 ns. The electrodynamic system parameters in this regime were as follows: distances from plungers *4* and *5* to the beam axis, $\sim 3\lambda_w/4$; coupling hole size along the *X*-axis, $\sim \lambda_w/30$ (λ_w is the wavelength in the waveguide). The observed radiation pattern corresponded rather well to the TE_{10} wave radiated from the rectangular horn *6*.

Figures 2 and 3 show typical patterns of the cathode voltage and beam current, RF signal, and microwave spectrum. During the current pulse, the cathode voltage decreased from 520 to 300 kV and the beam current increased from 9 to 14 kA, so that the vacuum diode impedance dropped by a factor of about 3. The impedance drop during the pulse could be related both to an increase in the number and size of the emission centers on the cathode surface [8] and to the cathode plasma motion. Nevertheless, the shape of the oscillograms indicates that the vircator radiation frequency remained unchanged during the pulse and was determined by parameters of the electrodynamic system. The radiation frequency could be varied by changing positions of the coupling hole and plunger *4*. The range of the relative radiation frequency variation was about 20% at the half maximum power.

Thus, we have experimentally implemented the concept of S-band vircator with premodulated electron beam based on a compact generator with inductive energy storage. The vircator radiation power was 300 MW at a power efficiency of about 5%. Advantages of this microwave device include the absence of external focusing magnetic fields, radiation frequency stability during the pulse, the possibility of mechanically adjusting the radiation frequency by changing the
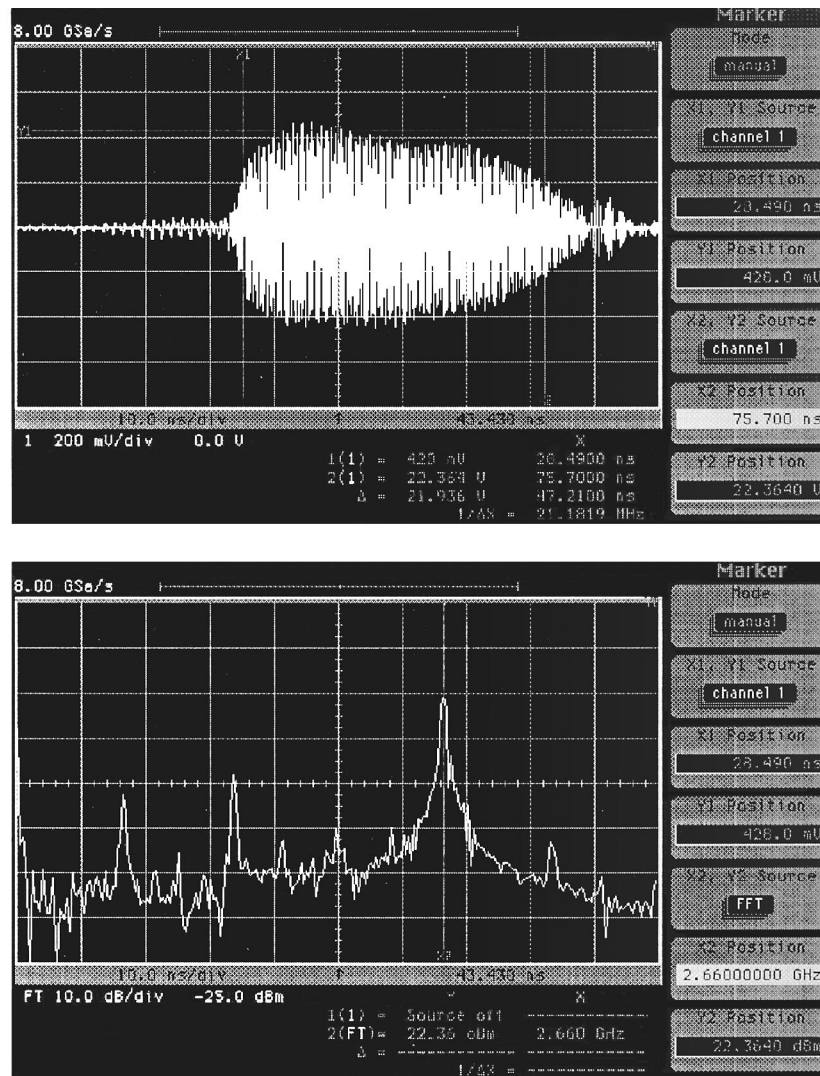
Fig. 3. Typical patterns of the RF signal and microwave spectrum of the vircator.

electrodynamic system parameters, adaptation to a change in the vacuum diode impedance, and a single-mode radiation spectrum composition.

REFERENCES

1. V. I. Kurilko and Ya. V. Faĭnberg, Pis'ma Zh. Tekh. Fiz. **2**, 397 (1976) [Sov. Tech. Phys. Lett. **2**, 154 (1976)].

2. N. P. Gadetskiĭ, I. I. Magda, S. I. Naĭsteter, *et al.*, Fiz. Plazmy **19** (4), 530 (1993).

3. S. D. Korovin, I. V. Pegel, S. D. Polevin, and V. P. Tarakanov, in *Proceedings of the 11th International Pulsed Power Conference, Baltimore, 1997*, p. 736.

4. A. A. Rukhadze, S. D. Stolbetsov, and V. P. Tarakanov, Radiotekh. Élektron. (Moscow) **37** (3), 385 (1992).

5. A. M. Efremov, B. M. Kovalchuk, S. V. Loginov, and A. A. Zherlitsin, in *Proceedings of the 12th Symposium on High Current Electronics, Tomsk, 2000*, p. 363.

6. A. N. Bastrikov, A. A. Kim, B. M. Koval'chuk, *et al.*, Izv. Vyssh. Uchebn. Zaved., Fiz., No. 12, 5 (1997).

7. C. A. Ekdahl, Rev. Sci. Instrum. **51** (12), 1645 (1980).

8. S. Ya. Belomyttsev, S. D. Korovin, and I. V. Pegel', Zh. Tekh. Fiz. **69** (6), 97 (1999) [Tech. Phys. **44**, 695 (1999)].

Translated by P. Pozdeev

Anomalous Pulsed Conductivity of Silver Bromide

B. P. Aduev, É. D. Aluker, V. M. Fomchenko, and V. N. Shvaĭko

Kemerovo State University, Kemerovo, Russia

e-mail: lira@kemsu.ru

Received September 4, 2000; in final form, November 8, 2000

Abstract—The first experimental results on the room-temperature pulsed conductivity of silver bromide excited in a pulsed mode by the X-ray bremsstrahlung radiation are reported. The data indicate that photosensitive materials are probably featuring the process of charge carrier multiplication during a time on the order of 10^{-9} s. The concentration of electrons in the conduction band of AgBr is estimated. The experimental concentration of the conduction electrons is about ten times greater than the concentration of electron–hole pairs created by the exciting radiation pulse. © *2001 MAIK "Nauka/Interperiodica".*

The problem of explaining anomalously high photographic sensitivity of silver halides (in particular, silver bromide) attracts the attention of researchers for more than 70 years [1]. It is commonly accepted that the quantum yield of atomic silver entering into the latent image centers (LICs) is very high (up to 0.5–1) [1]. A more thorough analysis of the problem shows that this value may even reach 2–3 [2], which makes the problem still more difficult.

It was demonstrated [3, 4] that the LIC formation takes a very short time, probably not exceeding 10^{-9} s. Times on this scale are usually characteristic of processes occurring in the electron subsystem of crystals [5]. Therefore, it would be natural to suggest that investigations of the pulsed conductivity of silver halides at a sufficiently high time resolution, providing information about the kinetics of relaxation processes in the electron subsystem, may reveal certain anomalies distinguishing these crystals from systems (sufficiently well studied) not possessing significant photographic sensitivity such as alkali-halide crystals and α-Al_2O_3 [6]. In this context, the task of our experiments was to study the pulsed-radiation-induced conductivity of silver bromide.

The experiments were performed with samples cut from an AgBr single crystal grown by the Stockbarger method from commercial silver bromide (special purity grade) preliminarily refined by zone melting (50 passages). The samples cut from the single crystal were thinned by polishing to a final thickness of 100–130 μm.

The electrodes were formed on the AgBr sample surface by the development technique, which ensures obtaining a homogeneous silver film on the crystal. The samples were excited by the bremsstrahlung radiation pulses generated in a copper foil upon absorption of a pulse of electrons extracted from an electron accelerator (electron energy, 200 keV; beam current density, 10^4 A/cm^2; pulse duration, 50 ps) [6]. The voltage applied to the sample had the shape of rectangular pulses (amplitude, 10–100 V; pulse duration, 1 ms), which allowed us to avoid the effect of sample electrolysis on the results of conductivity measurements. The channel of monitoring of the sample conductivity pulses ensured a time resolution of not worse than 150 ps [6].

We have studied a series of 20 silver bromide samples. Figure 1a shows typical oscillograms of the current pulses induced in AgBr by the bremsstrahlung radiation. The amplitudes and shapes of oscillograms observed in various samples differed by no more than 10% from each other, which falls within the error limits of the experimental procedure employed and which are related to instability of the excitation pulses and uncertainty of the oscillographic measurements. The results observed with multiply repeated irradiation shots (up to 100 pulses) on the same sample showed that both amplitude and form of the conductivity pulses remain unchanged, which is evidence for the absence of accumulation effects.

There are two principal distinctions of the conductivity pulses in AgBr from analogous pulses observed previously in alkali-halide crystals studied under similar conditions [6]:

1. A difference in the leading front kinetics of the conductivity pulse (Fig. 1a). A maximum of the conductivity pulse in alkali-halide crystals (AHCs) is attained during the excitation pulse (with an allowance for the instrumental function), while the maximum conductivity in AgBr is reached more than 1 ns after termination of the excitation pulse. This is evidence that the concentration of electrons (holes) keeps increasing even after termination of the excitation. The same situation was observed in AgN$_3$ and interpreted in

terms of the chain multiplication of the electron excitations [7].

2. A difference in the pulse amplitudes. Under conditions used for the conductivity measurements in AgBr (excited by the bremsstrahlung radiation pulse), the sensitivity of the measuring system was insufficient for detecting the conductivity pulse in AHCs. In the latter case, the pulses of close amplitude were observed only upon excitation of a sample directly by the electron pulse; that is, for the excitation density exceeding by at least three orders of magnitude that provided by the bremsstrahlung radiation [6]. Since the mobilities of the conduction band electrons in AgBr ($\mu \sim 50$ cm^2/(V s) [1]) and AHCs ($\mu \sim 10$ cm^2/(V s) [6]) are comparable, the difference in pulse amplitudes reflects a sharp difference in the electron concentrations in the two cases.

This difference is probably also related to the process of multiplication of the band carriers in AgBr, which is manifested by the conductivity buildup upon termination of the excitation pulse (Fig. 1a). In this context, it was very important to compare the concentrations of electrons in the conduction band generated by the excitation pulse and those detected in the sample conductivity pulse. The electron concentration in the conductivity pulse was calculated by the conventional formula $\sigma = en\mu$ with $\sigma = 4 \times 10^{-3}$ Ω^{-1} cm^{-1} (see Fig. 1b) and $\mu \approx 50$ cm^2/(V s) [6], which yields $n \approx 5 \times 10^{14}$ cm^{-3}.

In order to calculate the concentration of conduction electrons generated by the exciting radiation pulse, it is necessary to evaluate the bulk energy density E_v absorbed in the sample. The E_v value can be determined using the well-known relationship $E_v = D_0\rho_0$, where D_0 is the absorbed radiation dose and ρ_0 is the sample density. The absorbed dose was measured using several calibrated SiO$_2$ thermoluminescent detectors (TLD-K type) and a calibrated radiation dose meter (DTU-01 type). The D_0 value averaged over the readings of ten detectors was 10 mGy (measuring accuracy, 20%), which corresponds (with an allowance for the sample geometry) to an absorbed energy density of $E_v \approx 5 \times 10^{14}$ eV/cm^3.

The concentration of the electron–hole pair generated by the exciting radiation pulse can be estimated as $n = E_v/\varepsilon$, where ε is the mean energy required for the electron–hole pair production [8]. As is known, sufficiently good results are provided by estimates relating the ε value to the thermal bandgap width E_g. For materials with a band structure analogous to that of AgBr, $\varepsilon \sim (2–4)E_g$ [8]. Taking the thermal bandgap width for AgBr equal to $E_g \sim 3$ eV [1], we can readily determine that the exciting radiation pulse generates an electron–hole pair concentration n in the samples studied not exceeding 5×10^{13} cm^{-3}. Thus, the concentration of
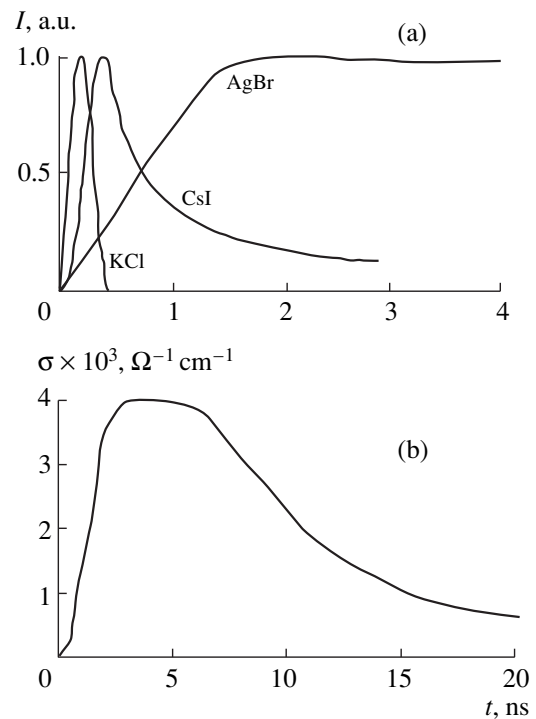

Fig. 1. Typical oscillograms of the radiation-stimulated conductivity in AgBr (bremsstrahlung excitation) and alkali-halide crystals (KCl and CsI, excited by pulsed high-energy electron beams) at $T = 300$ K: (a) current pulses (normalized to maximum); (b) total conductivity pulse in AgBr.

electrons generated by the excitation pulse is at least ten times lower than that detected in the conductivity pulse, which is convincing evidence to confirm the assumption concerning the electron multiplication upon the excitation pulse termination.

Therefore, both anomalies observed in the pulsed conductivity of AgBr give evidence for the process of electron excitation multiplication proceeding in this material, probably, by the chain mechanism analogous to tat in AgN$_3$ [7]. If the hypothesis about the chain multiplication of electrons in AgBr is valid, this concept may lead to serious consequences from the standpoint of explaining the anomalously high yield of atomic silver and the mechanism of the latent photographic image formation.

REFERENCES

1. P. V. Meĭklyar, *Physical Processes Involved in the Formation of Latent Photographic Image* (Nauka, Moscow, 1972).

2. A. L. Kortuzhanskiĭ, T. É. Kekhva, B. T. Plachenov, *et al.*, Izv. Sib. Otd. Akad. Nauk SSSR, Ser. Khim. Nauk **6**, 22 (1982).

3. I. O. Starobogatov, A. G. Belyaev, S. V. Vinogradov, *et al.*, Pis'ma Zh. Éksp. Teor. Fiz. **46** (4), 153 (1987) [JETP Lett. **46**, 192 (1987)].

4. V. N. Mikhaĭlov, V. N. Krylov, D. I. Stasel'ko, *et al.*, Opt. Spektrosk. **79** (4), 665 (1995) [Opt. Spectrosc. **79**, 613 (1995)].

5. A. S. Davydov, *Theory of Solid States* (Nauka, Moscow, 1976).

6. B. P. Aduev, E. D. Aluker, G. M. Belokurov, *et al.*, Phys. Status Solidi B **208**, 137 (1998).

7. B. P. Aduev, É. D. Aluker, G. M. Belokurov, *et al.*, Zh. Éksp. Teor. Fiz. **116** (5), 1676 (1999) [JETP **89**, 906 (1999)].

8. É. D. Aluker, D. Yu. Lusis, and S. A. Chernov, *Electron Excitations and Radioluminescence in Alkali-Halide Crystals* (Zinatne, Riga, 1979).

Translated by P. Pozdeev

Electron States of Europium Atoms on the Oxidized Tungsten Surface

S. Yu. Davydov

St. Petersburg State Electrotechnical University, St. Petersburg, Russia

Received November 9, 2000

Abstract—The charge state of europium (Eu) atoms adsorbed on the oxidized tungsten surface is evaluated. An energy band diagram of the adsorption system is proposed for large and small Eu coverages. The adsorption energy of Eu atoms is estimated. © *2001 MAIK "Nauka/Interperiodica".*

Recently, Ageev and Kuznetsov [1] studied on the electron-stimulated desorption (ESD) of europium atoms from a tungsten surface covered by a monolayer of oxygen (O/W). It was established that, in contrast to the well-known ESD of alkali metals from the substrate [2, 3], the ESD yield q of europium atoms as a function of the energy E_e of bombarding electrons exhibits a pronounced resonance character. In order to explain the observed ESD features, it is necessary first of all to construct an energy band diagram of the adsorption system studied in cases of small and large coverage Θ of Eu atoms occurring in the ground state (not excited by external electrons). The task of this study was to construct such a diagram. The proposed model will be checked using the results reported in [4] on the ESD of europium in Eu–O/W system. The results of these measurements showed, in particular, that the energy E_{des} required for the ESD of europium at low coverages is 4.2 ± 0.2 eV.

A monolayer of oxygen adsorbed on the surface of tungsten forms a quasi-two-dimensional system. The adsorption is determined primarily by the vacant p orbitals oriented perpendicularly to the substrate surface. These orbitals interact with each other (π interaction) to form an antibonding π energy band. According to the Harrison theory [5], the matrix element of this interaction is equal to $V_{pp\pi} = -0.63(\hbar^2/md^2)$, where m is the electron mass, d is the distance between nearest neighbors (for an adsorbed monolayer, this distance is taken equal to the tungsten crystal lattice constant, $d = 3.16$ Å [6]), and $\hbar$ is the reduced Planck constant. Since the energy band width in the tight binding approximation is $W_B = 2z|V_{pp\pi}|$ (where $z = 4$ is the number of nearest neighbors in the monolayer), we obtain $W_B \cong 3.85$ eV. Therefore, the band is sufficiently narrow and the states can be considered as localized. Naturally, there is an additional band broadening (and the corresponding delocalization of states) related to the hybridization of oxygen orbitals with those of the metal substrate, but this factor does not principally change the pattern. The energy band under consideration is due to

the level of electron affinity A being shifted as a result of the Coulomb interaction with the metal [7]:

$$A' = A + e^2/4r, \tag{1}$$

where r is the length of the adsorption bond.

Let us estimate the charge of oxygen ions in a monolayer adsorbed on a tungsten ribbon using a formula describing a change $\Delta\phi$ in the electron work function of the adsorption system [8]:

$$\Delta\phi = 4\pi e^2 N_{ML} n r, \tag{2}$$

where e is the electron charge (absolute value), N_{ML} is the concentration of oxygen atoms in the adsorbed monolayer (assumed to be 10^{15} cm^{-2}), and n is the occupation number for a quasilevel of adsorbed oxygen; the adsorption bond length is taken equal to 1 Å. Textured tungsten ribbons are characterized by the crystal face (100) predominantly emerging at the surface, for which the electron work function is 4.65 eV [9]; the value for an oxidized tungsten surface is assumed to be approximately 1 eV greater [10]. With an allowance for all these assumptions, we obtain an estimate for the occupation number (and, hence, for the oxygen ion charge) $n(O) = -Z(O) \approx 0.1$. This implies that the adsorbed oxygen ion possesses a rather small negative charge, which is generally typical of gases adsorbed on refractory metals [8]. Thus, the energy band of adsorbed oxygen is narrow and virtually empty.

Now let us consider the case of europium atoms adsorbed on a tungsten surface covered with a multilayer adsorbed oxygen film. Following Nikulin and Potekhina [11] and considering the adsorption of rare-earth metal atoms on the surface of tungsten and rhenium, we will assume that the adsorption of europium in the O/W system is accompanied by one $6s$ electron passing to the $5d$ state to participate in the adsorption interaction.

For small europium coverages ($\Theta \sim 0$), when Eu adatoms do not interact with each other, the occupation number n_0 of a one-electron d level of an adatom can be
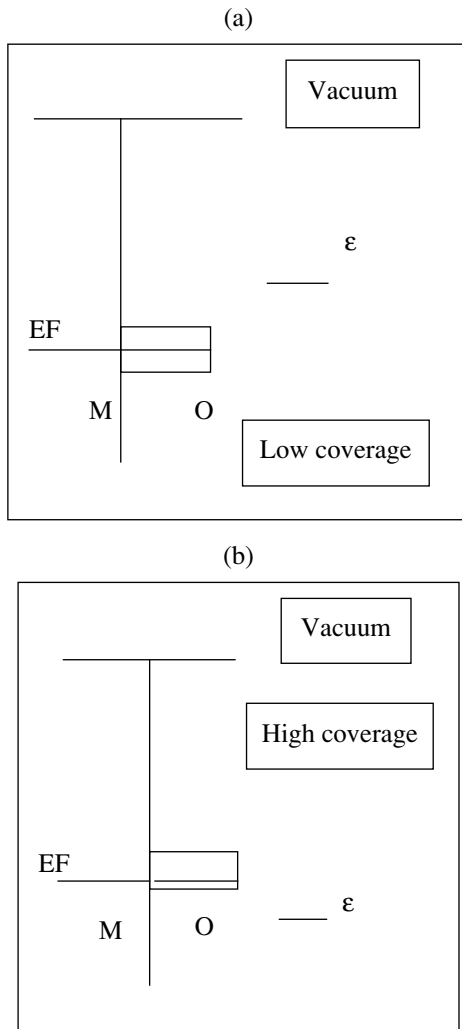
Fig. 1. A model energy band diagram of the Eu–O/W system for (a) low and (b) high adsorption coverages of europium: EF, Fermi energy level; M, metal (tungsten); O, two-dimensional (surface) band formed by oxygen; ε, center of a quasilevel (1a) or a two-dimensional band of europium.

evaluated using a theory based on the Anderson Hamiltonian [7, 8]

$$n_0 = \pi^{-1}\operatorname{arccot}(\varepsilon/\Gamma), \quad \varepsilon = -I + \phi + e^2/4a. \quad (3)$$

Here, Γ is the halfwidth of the Eu s quasilevel (we take $n = 1$ eV, which is a typical value [7, 8]); a is the sum of the atomic radii of europium and oxygen (these values are taken from [12]); and $I = 5.67$ eV is the ionization energy of europium [12] (for our rough estimates, this energy is assumed to coincide with the d level energy). In this approximation, we obtain $n_0(\text{Eu}) = 0.25$ ($Z_0(\text{Eu}) = 0.75$).

The estimates obtained within the framework of the Anderson theory show that europium is adsorbed on the oxidized tungsten surface in the form of positive ions with a charge close to unity. Let us assume that the

charge transferred from the Eu atom is localized on the oxygen atom situated immediately beneath the Eu adatom (for simplicity, we consider the case of atop-adsorption whereby adatom is situated above the substrate atom). Thus, the oxygen ion charge is $\tilde{Z}_0(\text{O}) \sim -1$.

In the case of large coverages ($\Theta \geq 0.5$), we assume that the depolarization effect makes the charge on a Eu adatom close to zero ($Z_1(\text{Eu}) \sim 0$). Therefore, the charge of an oxygen atom occurring under the Eu adlayer is the same as in the O/W system: $\tilde{Z}_1(\text{O}) \sim 0$.

Figure 1 shows the energy band diagrams for the cases of small (diagram a) and large (diagram b) Eu coverages Θ. For oxygen, the diagrams show the position of a local part of the band corresponding to an ion situated immediately beneath the Eu adatom (for europium, we indicate only the centers of gravity ε of the hybridized d states).

Finally, let us estimate the binding energy for a europium ion adsorbed on the O/W surface, which is equal to the desorption energy E_{des} corresponding to negligibly small (zero) coverages. The ion component of the binding energy $\mathscr{E}_{\text{ion}}$ can be estimated as the energy of interaction of a europium ion with the mirror image charge, assuming the mirror plane to pass through the "centers" of oxygen atoms:

$$\mathscr{E}_{\text{ion}} = \frac{Z_0(\text{Eu})e^2}{4a}, \quad (4)$$

which yields $\mathscr{E}_{\text{ion}} = 0.26$ eV.

In order to estimate the covalent component $\mathscr{E}_{\text{cov}}$ of the binding energy, we will use the matrix elements $W_2 = -(V_{pd\sigma} + V_{sd\sigma})/\sqrt{2}$ proposed by Harrison for perovskites [13]. For a single $d(\text{Eu})–sp(\text{O})$ bond, this yields $\mathscr{E}_{\text{cov}}^{(1)} = 2W_2 = 2.63$ eV. Assuming that, by analogy with rare-earth metal oxides of the M_2O_3 type, one metal atom in our system is also "bound" to one and a half oxygen atoms, we obtain for the covalent component $\mathscr{E}_{\text{cov}} = 3.94$ eV. Thus, the total binding energy is 4.20 eV, which coincides with the value obtained in [4] (of course, this complete coincidence of estimates is rather accidental).

REFERENCES

1. V. N. Ageev and Yu. A. Kuznetsov, Pis'ma Zh. Tekh. Fiz. **26** (13), 86 (2000) [Tech. Phys. Lett. **26**, 579 (2000)].

2. V. N. Ageev, O. P. Burmistrova, and Yu. A. Kuznetsov, Usp. Fiz. Nauk **158** (3), 389 (1989) [Sov. Phys. Usp. **32**, 588 (1989)].

3. V. N. Ageev, Prog. Surf. Sci. **47** (1/2), 55 (1994).

4. V. N. Ageev and E. Yu. Afanas'eva, Fiz. Tverd. Tela (St. Petersburg) **43**, 739 (2001) [Phys. Solid State **43**, 772 (2001)].

5. W. A. Harrison, Phys. Rev. B **27** (6), 3592 (1983).

6. C. Kittel, *Introduction to Solid State Physics* (Wiley, New York, 1976; Nauka, Moscow, 1978).

7. O. M. Braun and V. K. Medvedev, Usp. Fiz. Nauk **157** (4), 631 (1989) [Sov. Phys. Usp. **32**, 328 (1989)].

8. L. A. Bol'shov, A. P. Napartovich, A. G. Naumovets, and A. G. Fedorus, Usp. Fiz. Nauk **122** (1), 125 (1977) [Sov. Phys. Usp. **20**, 432 (1977)].

9. V. N. Ageev, O. P. Burmistrova, A. M. Magomedov, and B. V. Yakshinskiĭ, Fiz. Tverd. Tela (Leningrad) **32** (3), 801 (1990) [Sov. Phys. Solid State **32**, 472 (1990)].

10. E. V. Klimenko and A. G. Naumovets, Zh. Tekh. Fiz. **49** (6), 1282 (1979) [Sov. Phys. Tech. Phys. **24**, 710 (1979)].

11. V. K. Nikulin and N. D. Potekhina, Fiz. Tverd. Tela (Leningrad) **20** (11), 3354 (1978) [Sov. Phys. Solid State **20**, 1936 (1978)].

12. *Physical Quantities. Handbook*, Ed. by I. S. Grigor'ev and E. Z. Meĭlikhov (Énergoizdat, Moscow, 1991).

13. W. A. Harrison, *Electronic Structure and the Properties of Solids: The Physics of the Chemical Bond* (Freeman, San Francisco, 1980; Mir, Moscow, 1983), Vol. 2, Chap. 19.

Translated by P. Pozdeev

Nitrogen Oxides Removed from Flue Gases with Sulfur Dioxide under the Action of Pulsed Electron Beams

G. V. Denisov, Yu. N. Novoselov, and R. M. Tkachenko

Institute of Electrophysics, Ural Division, Russian Academy of Sciences, Yekaterinburg, Russia

Received July 25, 2000

Abstract—The process of a model flue gas mixture purification from nitrogen oxides by microsecond-pulsed electron beam ionization in the presence of sulfur dioxide (SO_2) was experimentally studied. In mixtures with a small SO_2 content, interaction of this component with nitrogen oxides leads to a considerable increase in the specific energy consumption required for the gas purification (~80 eV per NO molecule). In a gas mixture with approximately equal concentrations of SO_2 and NO, the energy consumption for NO removal decreases to a level close to that in the mixture free of sulfur dioxide. © *2001 MAIK "Nauka/Interperiodica".*

Purification of the flue gases of thermal power plants from sulfur and nitrogen oxides is an important ecological task that can be solved by various methods. One of these is based on irradiating the gas by pulsed electron beams. Kuznetsov *et al.* [1, 2] reported on the results of investigations of the process of sulfur dioxide (SO_2) removal from a model gas mixture by pulsed electron beams. It was demonstrated that use of a beam with optimum parameters provides for the SO_2 removal by means of a plasmachemical chain mechanism. Analogous experiments devoted to the removal of NO_x were reported in [3, 4]. However, the experiments described in [1–4] were carried out with model flue gas mixtures containing nitrogen, oxygen, and a single admixture (SO_2 or NO_x) taken in certain proportions. Below, we present the results of experiments aimed at determining the laws of NO_x removal by pulsed electron beams from gas mixtures modeling the real flue gases (i.e., also containing SO_2).

The experiments were performed using an electron accelerator analogous to that described in [5]. The electron beam produced by the accelerator had a 10×100 cm cross section, an energy of 200 keV, a pulse width at the half maximum of 5 μs, and a beam current density varied within $(4.5–12.5) \times 10^{-3}$ A/cm^2. The irradiated gas volume was 12 dm^3. A model gas mixture was prepared in a special mixer and then admitted into a plasmachemical chamber, which was preliminary evacuated and doubly washed with pure nitrogen. The model gas mixture was pumped through the chamber so as to move in a closed loop during the whole experiment. The experiments on the nitrogen oxide removal from gas mixtures containing various amounts of sulfur dioxide. The model mixture contained 90 vol % of nitrogen, 10 vol % of oxygen and admixtures of SO_2 and NO_x oxides varied from 0 to 1000 ppm. The gas mixture composition was monitored qualitatively and quantitatively using a TESTO-350 gas analyzer. The error of measurements did not exceed 3%.

During the experiment, we determined a change in the absolute concentration of nitrogen oxides, the degree of purification η, and the specific energy consumption ε per molecule of a toxic component. The η and ε values were calculated by the formulas

$$\eta = \Delta[\text{NO}]/[\text{NO}]_0,$$

$$\varepsilon = Wn/e\Delta[\text{NO}](\text{eV/mol}),$$

where $\Delta[\text{NO}]$ is a change in the concentration of nitrogen oxides during a series of electron pulses (in cm^{-3}); $[\text{NO}]_0$ is the initial impurity concentration in the model mixture (cm^{-3}); W is the beam energy absorbed in the gas per pulse (J/cm^3); n is the number of pulses in the series; and e is the electron charge (in Coulombs).

The results of our experiments showed that an increase in the beam current density leads, other conditions being equal, to a decrease in the degree η of the gas mixture purification from NO_x and to an increase in the energy consumption ε. Once this was established, subsequent experiments were performed at a beam current density $j = 4.5 \times 10^{-3}$ A/cm^2, which was the minimum possible for the accelerator employed.

Figure 1a shows a typical kinetics of decrease in the nitric oxide concentration [NO] with increasing number of irradiation pulses (beam shots) for the model gas mixtures with various SO_2 content. The initial concentration in these experiments was $[\text{NO}]_0 = 260–295$ ppm. As seen, the nitric oxide concentration drops with the number of shots. It should be noted that the character of this variation was approximately the same for various electron beam current densities. Another point of importance is the effect of the content of sulfur dioxide in the mixture on the [NO] kinetics. The most pronounced decrease in the nitric oxide concentration was observed in the absence of sulfur dioxide (Fig. 1a, curve *4*).

Small SO_2 additives ([SO_2] = 100–200 ppm) considerably decrease the rate of nitric oxide elimination from the gas mixture (curve *1*). However, an increase in the SO_2 content in the mixture up to 500 ppm and above intensifies the process again (curve *3*). Figure 1b shows variation of the concentration of various nitrogen oxides (NO_x, NO, and NO_2) and SO_2 with increasing number of the electron beam shots in a mixture with the initial SO_2 content of 150 ppm. Here, behavior of the [NO], [NO_2], and [NO_x] = [NO] + [NO_2] values is generally analogous to that observed in the absence of SO_2 [3]. The concentration of SO_2 also gradually decreases, in agreement with the behavior reported previously [2].

The effect of the SO_2 admixture on the removal of nitrogen oxides from flue gases is best revealed by determining the specific energy consumption ε per NO molecule. Figure 2 shows the plots of ε versus the initial NO concentration in mixtures with different SO_2 content. The minimum energy consumption (ε = 5–20 eV per NO molecule) is observed in the absence of SO_2 for the gas mixtures containing [NO] = 100–300 ppm (Fig. 2, curve *4*). A 200-ppm sulfur dioxide additive considerably increases the ε value, which reaches up to 80 eV per NO molecule (curve *1*). As the SO_2 content keeps increasing (curves *2* and *3*), the specific energy consumption decreases to 8–20 eV per NO molecule. A similar pattern is observed on plotting the degree of purification η versus [NO] for the mixtures with different SO_2 concentrations.

The observed variation of the gas purification parameters is explained by the interaction of nitrogen oxides with sulfur dioxide in the medium (air) ionized by the electron beam. The experimental data show that a small amount of SO_2 molecules reduces the rate of NO removal. Reactions responsible for this effect can be as follows [6]:

$$SO_2 + NO_2 \longrightarrow SO_3 + NO, \qquad (1)$$

$$2NO + O_2 \longrightarrow 2NO_2. \qquad (2)$$
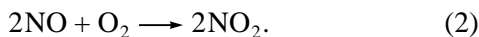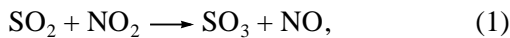
As the content of sulfur dioxide in the initial mixture increases, SO_2 molecules more significantly interact with other components of the ionized gas mixture. This interaction apparently favors the removal of sulfur dioxide together with nitrogen oxides [2]. In order to establish a particular mechanism of the SO_2 effect on the process, it is necessary to carry out additional investigation including numerical modeling of the process kinetics in ionized N_2–O_2–NO_x–SO_2 mixtures.

Thus, we demonstrated that SO_2 admixtures present in real flue gases significantly affect the process of the gas mixture purification from nitrogen oxides. Refine-
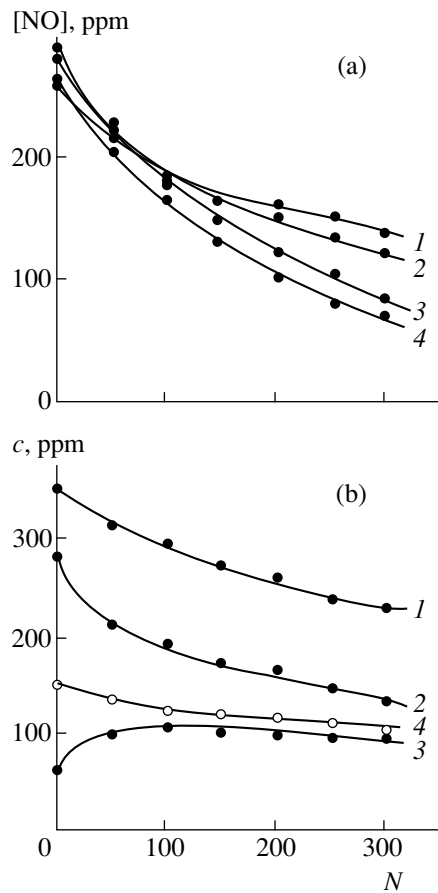

Fig. 1. Variation of the gas mixture composition with increasing number *N* of electron beam shots: (a) the kinetics of [NO] in model gas mixtures with various initial sulfur dioxide concentrations [SO_2]$_0$ = 100 (*1*), 300 (*2*), 500 ppm (*3*) and in the absence of SO_2 (*4*); (b) the kinetics of (*1*) [NO_x] = [NO] + [NO_2], (*2*) [NO], (*3*) [NO_2], and (*4*) [SO_2] in the model mixture with [SO_2]$_0$ = 150 ppm.

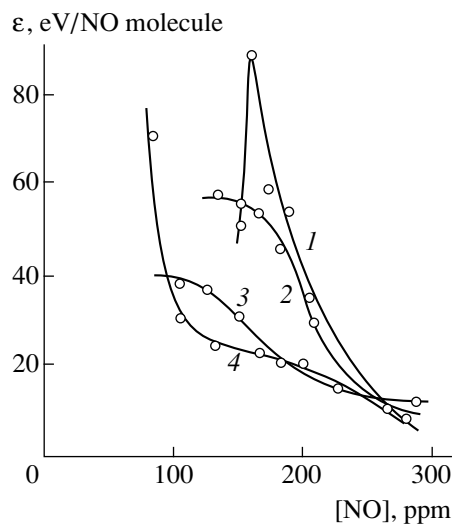**Fig. 2.** Plots of the specific energy consumption ε per NO molecule versus the initial nitric oxide concentration in mixtures with various initial SO_2 content [SO_2]$_0$ = 200 (*1*), 300 (*2*), 400 ppm (*3*), and in the absence of SO_2 (*4*).

ment of the mechanism of this effect requires additional investigations of this complex plasmachemical process.

REFERENCES

1. D. L. Kuznetsov, G. A. Mesyats, and Yu. N. Novoselov, Proc. SPIE **2374**, 142 (1995).

2. D. L. Kuznetsov, G. A. Mesyats, and Yu. N. Novoselov, Teplofiz. Vys. Temp. **34** (6), 845 (1996).

3. G. V. Denisov, Yu. N. Novoselov, and R. M. Tkachenko, Pis'ma Zh. Tekh. Fiz. **24** (4), 52 (1998) [Tech. Phys. Lett. **24**, 146 (1998)].

4. Y. Nakagawa and H. Kawauchi, Jpn. J. Appl. Phys. **37**, L91 (1998).

5. K. A. Garusov, D. L. Kuznetsov, Yu. N. Novoselov, and V. V. Uvarin, Prib. Tekh. Éksp., No. 3, 180 (1992).

6. V. N. Kondrat'ev, *Gas-Phase Reaction Rate Constants* (Nauka, Moscow, 1970).

Translated by P. Pozdeev

Determining the Order Parameter
for the Morphological Analysis of Two-Dimensional Structures

E. M. Sal'nikova and L. M. Martyushev

Institute of Industrial Ecology, Ural Division, Russian Academy of Sciences, Yekaterinburg, Russia
e-mail: mlm@ecko.uran.ru
Received November 20, 2000

Abstract—Problems encountered in determining the order parameter for two-dimensional structures are considered. The task is solved using two approaches, which are based on the spectral transformations (Fourier and Walsh) and the information entropy concept. The results of calculations for particular structures are used for a comparative analysis, showing both advantages and drawbacks of these methods. © *2001 MAIK "Nauka/Interperiodica".*

The existing methods of description of the morphological features of two-dimensional (2D) structures (or the projections of 3D objects) are mostly qualitative and frequently involve visual analysis. This complicates (and sometimes even hinders) the comparison of the results of various experiments, especially if the volume of data is large and the morphology variations are small. In recent years, these tasks are frequently solved using a quantitative parameter called the fractal dimensionality [1]. However, applicability of this approach to sufficiently "dense" or uniformly porous structures not representing spatial fractals is disputable, and the accuracy of such analysis is not high. Therefore, finding integral morphological parameters providing a means of the quantitative characterization and classification of 2D structures is still of importance.

Below, we will consider the parameters which can be used to quantitatively assess the degree of order and disorder of surface structures. Apparently, the introduction of such a parameter playing the role of an order parameter (here and below this term is understood in a somewhat narrower sense than in synergetics [2]) can be very useful both for numerous applications in materials science and for the rapidly developing science about self-organizing systems [2].

There are three natural approaches that can be used in solving the formulated task. The first is the traditional spectral approach, in which the order parameters are represented by the number of spectral components or by the components proper [2, 3]. However, in the absence of clearly pronounced individual modes, practical implementation of this approach meets serious difficulties. In the case of a noiselike spectrum, the order parameter can be introduced using the second approach based on calculating the fractal dimensionality—a spatially observable quantity calculated, for example, by the Takens method [4]. The main disadvantages of this method are the requirement of a large volume of the array used for discretization of the 2D "image" (sometimes this cannot be technically realized) and a large volume of time-consuming calculations (even with modern computational facilities). The third approach is based on the Shannon entropy [2, 5]. This method is rarely employed for introducing an order parameter in practical surface analysis, which is probably explained by the apparent abstractness.

Below, we will consider two of these approaches to the introduction of an order parameter for the surface structures, which are presently most acceptable for practical implementation. The first method is based on spectral transformations (with a special application to the case of a large number of spectral modes) and the second method employs the information entropy concept. The main attention will be paid to a practical implementation and a comparative analysis of the proposed methods.

We studied 2D crystalline structures (Fig. 1) simulated in a model computer experiment [6]. This object was selected due to extremely high variety of the possible structures obtained upon variation of the control parameter C (relative content of impurity) from 7.6 (skeletal crystal) to 293.9 (faceted crystal) [6]. We have analyzed the structures obtained upon variation of the parameter C at an 0.1 step, which is explained by the wish, on the one hand, to completely cover various morphologies possible in this model and, on the other hand, to avoid repeated analysis of the same structures (for this choice, the experimental series contained about 3000 structures). All the calculations were carried out for a central region of the structures (Fig. 1), which allowed us to eliminate the effect of the external boundary shape. The size of this region was selected as 64×64 (which was convenient for the spectral analysis). For the practical realization of the proposed methods, we ignored the impurity distribution in the crystal structure.
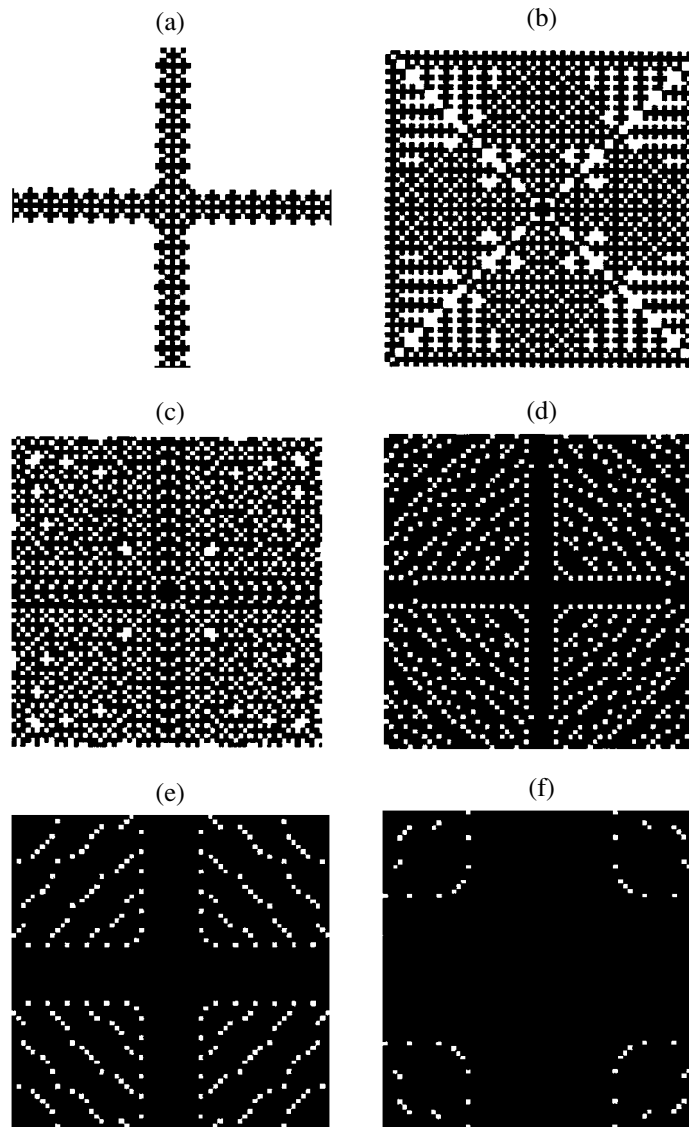
(a)

(b)

(c)

(d)

(e)

(f)

Fig. 1. The basic morphological types observed in the crystal during variation of the control parameter C: (a) 8.9 (1.16 ± 0.05); (b) 9.5 (1.93 ± 0.05); (c) 12.0 (1.97 ± 0.01); (d) 25.0 (1.95 ± 0.02); (e) 60.0 (1.97 ± 0.03); (f) 150.0 (1.99 ± 0.01). Values in parentheses indicate a fractal dimensionality with the corresponding error limits.

For implementing the entropy approach, each structure was represented by a graph [5] in which the vertices corresponded to cells occupied by the crystal (painted black in Fig. 1) and each pair of adjacent black squares was considered as an edge. The structures studied contain vertices of the four types (equivalence classes), connected to the graph with one, two, three, or four edges. Then, a topological index called the information content (essentially, the information entropy) was introduced using the Shannon formula $IC = -\Sigma p_i \log_2 p_i$ (where p_i is the fraction of vertices belonging to the ith equivalence class, $i = 1$–4). This index is considered as a quantitative measure of the structural order in the graph [2, 5]. The probabilities entering into the IC value are normalized to the total number of ver-

tices, which allows the order parameters of graphs with different numbers of vertices to be compared. The IC value is maximum for a vertex belonging with equal probability to one of the four classes. When all vertices in a structure are equivalent, IC is equal to zero.

Using this scheme, each structure was characterized by the number of vertices of each type and by the information content calculated using the Shannon formula. Figure 2a shows a plot of the IC versus relative impurity concentration. The IC curve possesses a dome shape with a maximum shifted toward smaller impurity concentrations. The IC maximum falls within the region of the control parameter values between 10 and 13.7 (a typical structure for this region is depicted in Fig. 1c). On the general background trend (Fig. 2a),

there are certain jumplike variations which are most pronounced in the region of small impurity concentrations. This fact reflects real changes observed in the model structures [6], where the most significant, multiply repeated structural rearrangements were observed for small values of the control parameter (Figs. 1a–1d). In contrast to the fractal dimensionality, the *IC* value can quantitatively characterize very different structures. For example, the fractal dimensionality of the structures depicted in Figs. 1e and 1f is the same (to within the determination error), while the information content of these patterns is significantly different (0.906 versus 0.380 byte, respectively).

In order to compare the results of the entropy approach and the spectral method, we used the 2D transformations of two types, Fourier and Walsh. The former was chosen due to its wide traditional use in the analysis of 2D structures [1], which is related to its simple implementation in all standard mathematical software. The Walsh transformation is apparently most adequate for the type of structures studied from the standpoint of basis functions (binary and step functions) [7]. We employed the Kronecker ordered Walsh functions, which are readily introduced using the Hadamard matrices [7] (contained in MATLAB).

In order to carry out the spectral transformations, each cell in the structure image was digitized using four counts [8]. The crystal cells were assigned +1, while the solution and impurity were assigned −1. Since the number of spectral modes is traditionally used to evaluate the structural order, we have to introduce some integral structural parameter related to the number of spectral peaks. Since no universal parameters are known for complicated spectra with a large number of peaks, we tried two possibilities. The first value (K_1) was determined as number of peaks in the energy spectrum, the amplitudes of which exceed a certain fraction of the maximum peak amplitude; the second quantity (K_2) was determined as the minimum number of peaks representing a certain fraction of the total spectrum energy. Apparently, the smaller the K_1 and K_2 values, the higher the structure ordering. A common disadvantage of the proposed variants is the necessity of formulating an apriori unknown criterion (reflecting the system evolution) used for selecting significant peaks.

Each of the two parameters has advantages from the standpoint of the task to be solved. Let us compare the spectra of two structures, one representing a clearly pronounced peak on the noise background and the other displaying several such peaks. The K_2 value for the second spectrum is naturally smaller and, based on the comparison of K_2 values only, we might conclude that the first structure is more chaotic. However, both the K_1 value and intuition suggest the opposite. On the other hand, should there be no such single pronounced peak, the use of K_1 criterion becomes very subjective. In comparing the results of two spectral transformations of the same structure, it is more expedient to
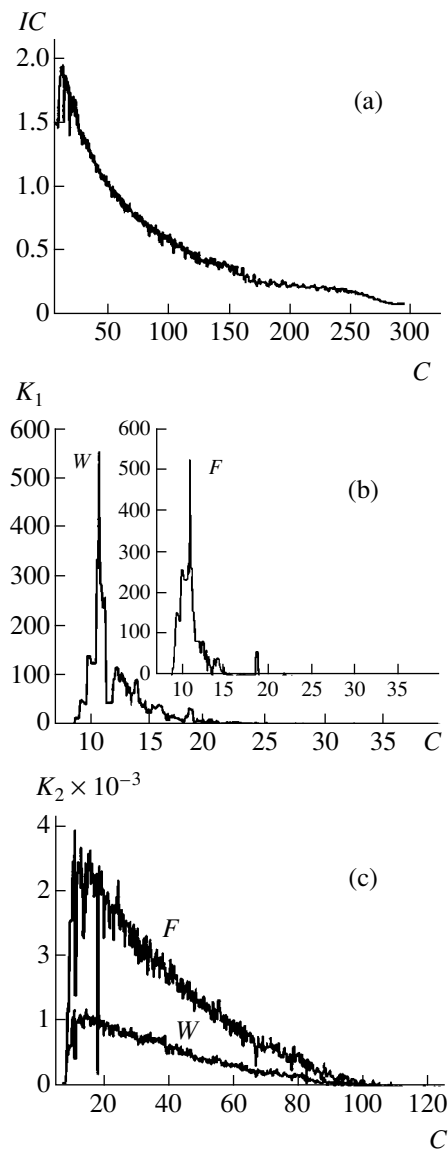

Fig. 2. Plots of the (a) information content *IC* and the spectral parameters (b) K_1 and (c) K_2 versus relative impurity concentration (control parameter) *C*. The K_1 and K_2 values were determined using the Walsh (*W*) and Fourier (*F*) transformations.

employ K_2 because this quantity refers to the spectrum energy, which is the same for both spectra [7, 8].

In selecting the critical fractions for determining K_1 and K_2, we were guided by two factors: the parameters should be sufficiently sensitive to variations of the control parameter while being insensitive to the spectral noise components. It was found that the optimum levels are 1% for K_1 and 90% for K_2.

Figure 2b shows the results of calculations of the parameter K_1. As seen, the curves obtained for the Fourier and Walsh transformations are qualitatively similar. Indeed, the maximum value of K_1 in both cases falls within the impurity concentration interval from 10 to

11.5. However, there are certain distinctions as well: K_1 for the Fourier spectrum more rapidly attains a constant level and then becomes virtually insensitive with respect to variation of the control parameter determining the structure morphology. Figure 2c presents the analogous results for the parameter K_2. Similarly to the case of K_1, the K_2 plots for the Fourier and Walsh transformations are qualitatively similar, showing a maximum in the impurity concentration interval from 10 to 16. Note that the K_2 value for the Fourier transformation is approximately four times that for the Walsh transformation. This implies that a parameter based on the energy spectrum gives advantage to the Walsh transformation over the Fourier transformation for C from 12 to 100.

An analysis indicates that, in terms of the order parameters K_1 and K_2 determined for sample structures of the type depicted in Fig. 1, neither of the two spectral transformations offers significant advantages for description of these structures. This result can be explained by the fact that, according to our calculations, the Walsh transformation has significant advantages in the analysis of asymmetric structures. For symmetric patterns with a nonuniform arrangement of pores filled with solution or impurity (nonuniform porous structure), an advantage of the Walsh transformation over the Fourier transformation is not as pronounced. Finally, for the symmetric uniformly porous structures, an advantage of the Walsh transformation is related to the signal digitization: as the discretization frequency increases, the number of peaks in the Fourier spectrum increases in direct proportion to the number of counts, while the number of peaks in the Walsh spectrum remains unchanged (which is an evident advantage for practical realization). Since the structures studied in our case (Fig. 1) belong to this last type, the comparison did not reveal any significant advantage of the of the Walsh transformation over the Fourier transformation (Figs. 2b, 2c); however, for the digitization process employed (four counts), the Walsh transformation offered at least a fourfold advantage over the Fourier transformation (Fig. 2c).

A comparison of the results of spectral and entropy approaches reveals a direct relationship between the topological index *IC* and the parameters related to the number of peaks. Both approaches indicate the pres-ence of two regions (with approximately coinciding boundaries), with the maximum occurring within the impurity concentration interval from 10 to 13.7 (Fig. 2). An increase in the control parameter (concentration *C*) leads to chaotization in the first region, and to structural ordering in the second region.

Thus, the results of our investigation lead to the conclusion that complicated structures described by a large number of spectral modes should be characterized by the order parameter determined as the Shannon entropy (information content) *IC*. An advantage of this approach is the absence of additional evaluation criteria necessary in the case of spectral methods. It should be noted that a correlation observed in this study between the *IC* and the spectral characteristics may not always be revealed. However, this circumstance poses no limitations on the use of *IC*, since the term "order parameter" is presently not strictly determined.

REFERENCES

1. J. C. Russ, *Fractal Surfaces* (Plenum, New York, 1999).
2. H. Haken, *Synergetics: An Introduction* (Springer-Verlag, Berlin, 1978; Mir, Moscow, 1989).
3. P. Bergé, Y. Pomeau, and C. Vidal, *L'ordre dans le chaos: vers une approche déterministe de la turbulence* (Hermann, Paris, 1988; Mir, Moscow, 1991).
4. M. I. Rabinovich, A. L. Fabrikant, and L. Sh. Tsimring, Usp. Fiz. Nauk **162** (8), 1 (1992) [Sov. Phys. Usp. **35**, 629 (1992)].
5. *Chemical Applications of Topology and Graph Theory*, Ed. by R. B. King (Univ. of Georgia, Athens, 1983; Mir, Moscow, 1987).
6. L. M. Martyushev and V. D. Seleznev, Pis'ma Zh. Tekh. Fiz. **25** (20), 71 (1999) [Tech. Phys. Lett. **25**, 833 (1999)].
7. L. A. Zalmanzon, *The Fourier, Walsh, and Haar Transforms and Their Application in Control, Communications and Other Fields* (Nauka, Moscow, 1989).
8. A. A. Kharkevich, *Spectra and Analysis* (Gostekhizdat, Moscow, 1957).

Translated by P. Pozdeev

The Field-Induced Ion Evaporation
from Electrolyte Solutions

A. I. Grigor'ev

Yaroslavl State University, Yaroslavl, Russia
e-mail: grig@uniyar.ac.ru
Received November 3, 2000

Abstract—It is demonstrated that, in a mass spectrometer with electrohydrodynamic injection of analyzed substances, the field-induced ion evaporation provides for the effective formation of an ion-cluster beam at an electric field strength of ~1 V/nm at a charged liquid surface. © *2001 MAIK "Nauka/Interperiodica"*.

Introduction. Problems encountered in the mass spectrometry of nonvolatile and thermally unstable organic substances can be solved by using the effect of electrohydrodynamic dispersion of the solutions of such substances in weak electrolytes [1]. The idea of this method consists in that the electrohydrodynamic dispersion process leads to the formation of solution clusters or small droplets containing one molecule of the substance studied and a certain amount of ions and molecules of the solvent. Once the solvent ions and molecules are removed from the cluster by some means, the residue represents a complex of ion or molecule of the compound studied. However, a theoretical approach to the physical laws determining the ion and cluster formation under these conditions is still not completely developed [2, 3].

In the case of a vacuum mass spectrometer, where the ion-cluster beam is formed at low temperatures and pressures, it would be natural to assume that the main role belongs to the effect of field-induced evaporation of ions and clusters from solution [1–4]. Moreover, we should distinguish between the direct field evaporation of ions from the vertex of an emitting cusp on the solution surface [1, 2, 5, 6] and the field evaporation of ions from the surface of strongly charged submicron droplets emitted from the charged solution surface in a nonlinear stage of development of the instability with respect to the intrinsic charge [2, 3, 7–10].

The main difficulty in developing a theoretical model of the field-induced evaporation of ions from electrolyte solutions is related to a large value of the electric field strength at the solution surface, which is necessary for the ion beam formation [2, 8]. According to estimates [2, 5, 6], the field evaporation of "bare" (i.e., deprived of the solvate shell) ions from an electrolyte solution is significant only for an electric field strength of $E \approx 10$ V/nm. As was demonstrated by Iribarne and Thomson [4], already at $E \approx 1$ V/nm we must observe an effective evaporation of clustered (solvated) ions—aggregates comprising an ion and 6–12 neutral water molecules, for which the activation energy of evaporation is minimum.

Field ion evaporation model. The mechanism of field-induced evaporation of ions and charged clusters from electrolyte solutions is implied to be generally identical to that involved in the field evaporation of ions from a metal surface, which was developed in much detail (in terms of a thermoactivated process) for the field ion microscopy [11] and liquid-metal ion sources [12]. According to this theory, the rate constant of the electric-field-induced ion evaporation by thermal activation above the Schottky barrier (related to an electric field with a strength E at the metal surface) is described by a simple Arrhenius relationship [11]:

$$ K = \nu \exp\left[-\frac{Q - (q^3 E)^{1/2}}{kT}\right], \quad Q \equiv \Lambda + J - W, \quad (1) $$

where ν is the ion oscillation frequency ($\nu \sim 10^{12}$–10^{13} s^{-1} [11]); k is the Boltzmann constant; T is the absolute temperature; and q is the ion charge. In the exponent of Eq. (1), the quantity Q in the numerator is the activation energy for evaporation of a singly charged ion from the metal surface. This value is determined for a thermionic process by the following scheme [11]: (i) a neutral atom evaporates from the metal surface, absorbing the sublimation energy Λ; (ii) the atom is ionized, which requires an additional energy J; (iii) the electron returns to the metal, liberating an energy W equal to the electron work function. The second term in the numerator of the exponent (square root) describes a decrease in the activation energy of the field ion evaporation due to the Schottky effect.

The field evaporation of ions or ion clusters from the electrolyte solutions is also described by a relationship similar to Eq. (1) [4, 6], in which the activation energy Q for the ion evaporation from a metal surface is replaced by the quantity ΔH_+ representing a change in the enthalpy upon the ion (or ion cluster) transition

Table 1. The values of the sublimation (Λ) and dissociation (D) energies for the molecules studied

	Molecule			
	NaF	NaI	NaBr	NaCl
Λ, eV	2.91	2.08	2.25	2.39
D, eV	4.96	3.76	3.13	4.22

Table 2. The electron affinities L of the halogen atoms studied

	Atom			
	F	I	Br	Cl
L, eV	3.4	3.06	3.36	3.61

Table 3. The activation energy Q for the field evaporation of Na$^+$ ion from various aqueous electrolyte solutions

	Solution			
	NaF	NaI	NaBr	NaCl
Q, eV	3.48	1.78	1.03	2.01

from solution to vacuum. This last quantity is taken equal to the value of ΔH_* (with inverse sign), representing a change in the enthalpy upon solvation of the ion (or additional solvation of a clustered ion) in solution. As was demonstrated in [4] for clustered ions, the ΔH_* value considered as a function of the number n of neutral atoms in the cluster is a nonmonotonic function with a minimum ($\Delta H_* = 2.32$–2.73 eV) at a certain value $n = n_*$. This value of the activation energy for the field evaporation of clustered ions provides for the agreement of theory and experiment even at $E = 1$ V/nm. However, the activation energy ΔH_* for the evaporation of bare ions calculated from the solvation energy is 2–3 times the value indicated above [13]. From this, we may infer that the agreement between theory and experiment can be achieved only with electric field strengths ten times greater at the solution surface [2, 5, 6], which must be as high as those for the field evaporation of metals ($E \geq 10$ V/nm). However, this conclusion is still rather hasty, since the field strengths on the order of ~10 V/nm for the field evaporation of ions from the solid or liquid metal surface are achieved in practice only for specially prepared emission points having a tip curvature radius ~1 μm. Reaching a field strength of ~10 V/nm is hardly probable in mass spectrometers with electrohydrodynamic injection of analyzed substances into a discharge chamber via a capillary with a diameter of ~100 μm. Moreover, it must be noted that not all the possible channels of the field-induced ion evaporation from solutions were taken into consideration in [2, 5, 6].

Results and discussion. In a real solution, only a certain part of dissolved molecules (depending on the component concentrations, temperature, and features of the intermolecular interaction [13]) are dissociated rather than all of these molecules. In this context, let us evaluate the possibility of the field evaporation of a positive ion Na$^+$ ion from aqueous solutions of various salts: NaF, NaI, NaBr, and NaCl. The activation energy for the field evaporation of Na$^+$ ions from the solution surface will be calculated based on the virtual thermionic process for neutral NaF, NaI, NaBr, and NaCl molecules, by analogy with the calculation for the field evaporation of ions from a metal surface [11]. In contrast to the case considered in [11] (ion detachment from a continuous metal surface), we will consider a process of the field-induced decomposition of a neutral salt molecule (NaF, NaI, NaBr, and NaCl) on the surface of an electrolyte solution (in the region of a strong electric field) with the formation of positive (Na$^+$) and negative (F$^-$, Br$^-$, I$^-$, or Cl$^-$) ions and the Na$^+$ ion transition to vacuum. In terms of the energy of sublimation of a molecule (Λ); the ionization energy (J); the electron affinity to F, I, Br, or Cl atom (L); the electron work function for water (W); and the energy of dissociation into two neutral particles, Na and F, I, Br, or Cl (D), the activation energy for the field-induced Na$^+$ ion evaporation from an electrolyte solution can be written as

$$Q = \Lambda + D + J - W - L. \qquad (2)$$

This implies that (i) a molecule is sublimated from solution and dissociated into two neutral atoms, (ii) Na atoms are ionized, (iii) electrons and neutral atoms (F, I, Br, or Cl) return into solution where electrons attach to these atoms with the formation of negative ions. It should be emphasized that this cycle is virtual: in fact, the field breaks a salt molecule into positive (Na$^+$) and negative (F$^-$, I$^-$, Br$^-$, or Cl$^-$) ions immediately on the solution surface and transfers the Na$^+$ ion into vacuum.

Table 1 gives the values of the sublimation (Λ) and dissociation (D) energies for NaF, NaI, NaBr, and NaCl molecules [14]. Table 2 lists the electron affinities L of F, I, Br, and Cl atoms [15]. The ionization energy for Na ($J = 5.14$ eV) was taken from [14]. The electron work function for water ($W = 6.13$ eV) was taken from [16]. The values of the activation energy Q calculated by Eq. (2) for the field evaporation of a positive ion Na$^+$ ion from electrolytes based on the aqueous solution of salts NaF, NaI, NaBr, and NaCl are presented in Table 3. As seen, the calculated Q values are always smaller than the bare ion evaporation energy $Q_* = 4.18$ eV [2, 13] calculated using the hydration (solvation) energies according to the concepts developed in [2, 4, 6]. It is also evident that the calculated Q values are close to the activation energy for the field evaporation of clustered ions (2.32–2.73 eV) calculated based on the Iribarne–Thomson theory [4, 8].

It should be pointed out that a decrease in the potential barrier height due to the Schottky effect at $E = 1$ V/nm for a singly charged ion, which is determined by the second term in the numerator of exponent in Eq. (1), amounts to ≈ 1.18 eV. Thus, the probability of the field evaporation of a Na^+ ion, which is determined by the exponent in Eq. (1), will be greater than unity, for example, for a NaBr solution and smaller than unity for NaI and NaCl solutions; even the latter probabilities are sufficiently high in order to provide for a high intensity of Na^+ line intensity in the spectrograms (this is due to a large value of ν and a high concentration of nondissociated molecules on the solution surface).

Conclusion. An electric field strength of ~1 V/nm at an electrolyte solution surface allows for an effective field evaporation of both bare and clustered ions. The electric field strength on this order of magnitude can be achieved at the surface of submicron droplets formed in the final stage of a cascade decay during the electrostatic dispersion of a conducting liquid [9]. The channel of the field evaporation of bare ions from electrolyte solutions considered in this paper, which relates the process activation energy to the type of dissolved substances, can be readily verified in experiment.

REFERENCES

1. D. S. Simons, Int. J. Mass Spectrom. Ion Processes **15** (3), 291 (1974).

2. N. B. Zolotoĭ, G. V. Karpov, and V. E. Skurat, Zh. Tekh. Fiz. **58** (2), 315 (1988) [Sov. Phys. Tech. Phys. **33**, 193 (1988)].

3. J. B. Fenn, M. Mann, Chin Kai Meng, *et al.*, Science **246** (4926), 64 (1989).

4. J. V. Iribarne and V. A. Thomson, J. Chem. Phys. **64** (6), 2287 (1976).

5. N. B. Zolotoĭ and G. V. Karpov, Dokl. Akad. Nauk **348** (3), 336 (1996).

6. N. B. Zolotoĭ, Zh. Tekh. Fiz. **65** (11), 159 (1995) [Tech. Phys. **40**, 1175 (1995)].

7. L. N. Gall', N. V. Krasnov, Yu. S. Kusner, *et al.*, Zh. Tekh. Fiz. **54** (8), 1559 (1984) [Sov. Phys. Tech. Phys. **29**, 911 (1984)].

8. F. W. Rollgen, E. Bramer-Weger, and L. Buttfering, J. Phys. **48**, C6-253 (1987).

9. A. I. Grigor'ev and S. O. Shiryaeva, Izv. Ross. Akad. Nauk, Mekh. Zhidk. Gaza, No. 3, 3 (1994).

10. S. O. Shiryaeva and A. I. Grigor'ev, Zh. Tekh. Fiz. **63** (8), 162 (1993) [Tech. Phys. **38**, 715 (1993)].

11. E. W. Muller and T. T. Tsong, *Field Ion Microscopy: an Introduction to Principles, Experiments, and Applications* (Elsevier, New York, 1969; Metallurgiya, Moscow, 1972).

12. R. Gomer, Appl. Phys. **19**, 365 (1979).

13. N. A. Izmaĭlov, *Electrochemistry of Solutions* (Khimiya, Moscow, 1976).

14. L. V. Gurvich, I. V. Veĭts, V. A. Medvedev, *et al.*, *Thermodynamic Properties of Individual Substances* (Nauka, Moscow, 1982), Vol. 4, Part 1.

15. L. V. Gurvich, I. V. Veĭts, V. A. Medvedev, *et al.*, *Thermodynamic Properties of Individual Substances* (Nauka, Moscow, 1978), Vol. 1, Part 1.

16. V. S. Fomenko, *Emission Properties of Materials: Handbook* (Naukova Dumka, Kiev, 1981).

Translated by P. Pozdeev

The Conditions of Existence of Autooscillations
in a Dropwise Liquid Flow through a Vertical Capillary

A. V. Melkikh and V. D. Seleznev

Ural State Technical University, Yekaterinburg, Russia

Received October 5, 2000

Abstract—A model describing the dropwise liquid flow through a vertical capillary, taking into account the mutual influence of the drops, is developed, and the conditions of existence of an autooscillatory regime in this system are established. The period and amplitude of the autooscillations are described as functions of the system parameters. © 2001 MAIK "Nauka/Interperiodica".

The dropwise flow of liquids in capillaries is employed in various devices and technological processes, for example, in electric jet printers, liquid dosing apparatus employed in the chemical industry and medicinal equipment, etc. The liquid flow transition into the dropwise regime was studied both experimentally and theoretically [1–5].

The conditions needed for drop formation are well known for various liquids and different system geometries [4, 5]. However, it is obvious that the presence of an external noise or a noise related to the drop formation and separation may significantly affect the boundaries of existence of the dropwise flow regime. Previously [6], we developed a model describing the transition from evaporation to a dropwise flow regime and vice versa. It was established that the mutual influence of the drops may, under certain conditions, give rise to a hysteresis phenomenon. In this case, the transitions from evaporation to a dropwise regime may proceed in a jumplike manner.

If there is a reservoir above the capillary, which is supplied with liquid at a preset rate, then there is a certain interval of the flow rates in the capillary for which the system has no stationary solutions [6]. In this case, the system may feature autooscillations. The purpose of this study was to establish the conditions and system parameters necessary for the appearance of autooscillations in the dropwise flow of a liquid through a capillary.

The frequency (J) of liquid dropping from a capillary can be described by the following equation [6]:

$$\frac{32\eta\gamma L}{3r}J = \Delta p - \frac{2\sigma}{r} + \xi\rho g r \exp\left(-\frac{1}{J\tau}\right),$$

where Δp is the pressure difference between the capillary ends, γ is a coefficient taking into account the difference between the radii of the drops and the capillary [2], L is the capillary length, ρ is the liquid density, ξ is a dimensionless coefficient (on the order of unity), σ is the coefficient of surface tension, r is the capillary duct radius, and η is the dynamic viscosity of the liquid. A characteristic time of the pressure relaxation at the free liquid surface is τ. Using the dimensionless variables

$$\Delta p' = \frac{\Delta p}{\xi\rho g r}; \quad J' = J\tau$$

the above equation can be rewritten as (dashes are omitted)

$$MJ = \Delta p - B^{-1} + \exp\left(-\frac{1}{J}\right), \tag{1}$$

where $B = \dfrac{\rho g r^2 \xi}{2\sigma}$ is the Bond number characterizing the ratio of the gravity force to the surface tension and $M = \dfrac{32\eta\gamma L}{3r^2\xi\rho g\tau}$ is a dimensionless quantity characterizing the ratio of the viscosity forces to the gravity forces. It was also established previously [6] that the curve $J(\Delta p)$ has an S-like shape for $M < 4e^{-2}$.

Let us consider the equation of balance for the volume of liquid in the reservoir under the controlled flow conditions:

$$S\frac{dh}{dt} = Q_{in} - Q.$$

Here S is the cross section area, h is the liquid column height, Q_{in} is the controlled input flow rate (which is constant in time), and Q is the current flow rate in the capillary (Fig. 1). The rate of variation of the pressure difference between the capillary ends can be expressed as follows:

$$\frac{d\Delta p}{dt}\frac{S}{\rho g} = Q_{in} - Q, \tag{2}$$

where the flux Q can be expressed through the liquid

dropping frequency:

$$Q = J\frac{4\gamma\pi r^3}{3}.$$

Expressing Δp through J and introducing the dimensionless time

$$dt' = dt\frac{4\pi r^2\gamma}{3\xi S\tau},$$

we obtain an equation in the dimensionless variables (dashes are omitted)

$$\left[M - \frac{1}{J^2}\exp\left(-\frac{1}{J}\right)\right]\frac{dJ}{J_{\text{in}} - J} = dt. \qquad (3)$$

Equation (3) is valid on the time scale significantly greater than a characteristic time of the drop formation. In the absence of drops, a characteristic time for this regime can be determined (from Fig. 2), by the formula

$$\frac{\Delta p_1}{J_{\text{in}}} = t_0. \qquad (4)$$

In this regime (in the absence of noise), the system performs a cyclic motion over the curve $J(\Delta p)\Delta p = 1/B$ (Fig. 2): the system moves by a lower branch up to point B, then jumps to the upper branch and goes down to point A, and jumps back to the lower branch. This behavior is physically manifested by the liquid dropping process being periodically suspended. By controlling the input flow, we may change the period of autooscillations.

Numerically integrating Eq. (3) and using relationships (1) and (4), we obtain a piecewise curve describing the time variation of the dropping frequency. Figure 3 shows a plot of the dropping frequency versus time for $J_{\text{in}} = 0.5$ and $M = 0.2$. The period of autooscillations can be divided into three parts corresponding to the motion over a certain portion of the curve in Fig. 2. For small M, a major part of the autooscillation period is the "dead" time, when the liquid flow is absent. When M approaches the critical level, the "dead" region disappears (beginning with $M = 0.37$) but the autooscillations still exist representing alternation of various dropping regimes (fast and slow [6]). The period of autooscillations depends both on the input flow rate and the M value.

Dependence of the period of autooscillations on the input flow is as follows: when the flow rate approaches the level of stability loss (points A and B in Fig. 2), the time of the system motion over the corresponding branch of the curve in Fig. 2 increases to infinity (e.g., when J_{in} approaches point A, the system occurs for an infinitely long time on the upper branch of the curve). Accordingly, the period of autooscillations tends to infinity. This behavior can be described by expanding Eq. (3) into series in the vicinity of the point of instability development. A minimum value of the period is
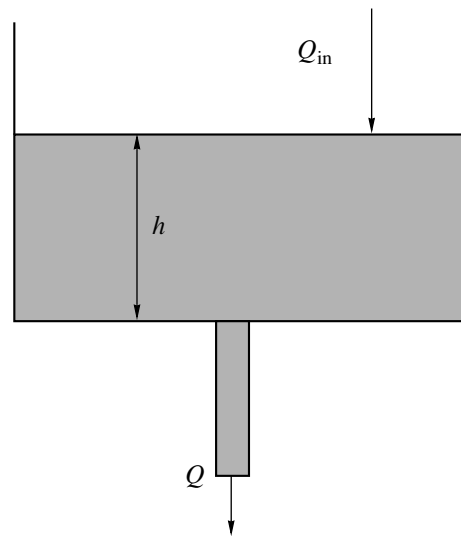
Fig. 1. A schematic diagram of the model system comprising a capillary with controlling reservoir.
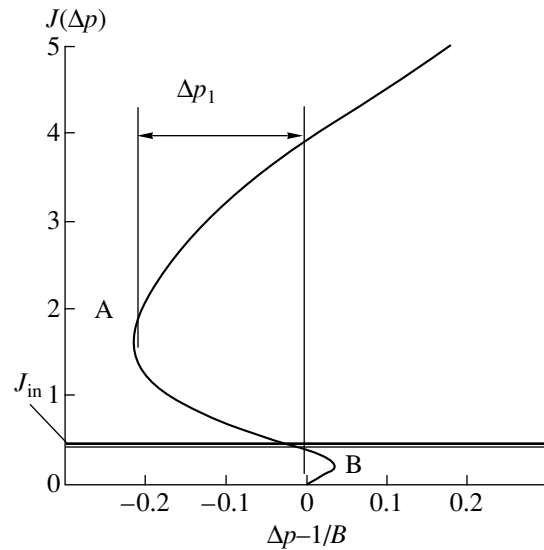

Fig. 2. The plot of dropping frequency versus pressure difference. The horizontal line indicates the input control flow rate.
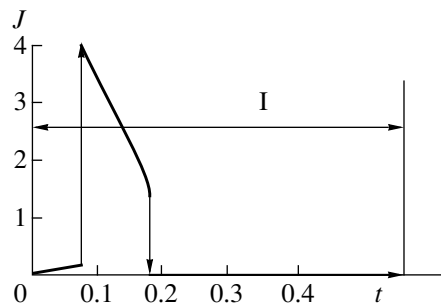

Fig. 3. The plot of dropping frequency versus time for $J_{\text{in}} = 0.5$ and $M = 0.2$ (I is the region corresponding to autooscillations).
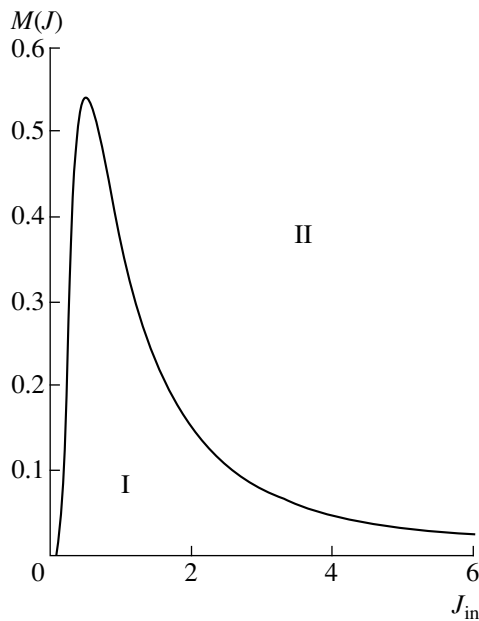
Fig. 4. Phase diagram in the M versus J_{in} coordinates showing the regions where autooscillations (I) appear and (II) disappear.

attained when the input flow rate takes a value between the points of stability loss. As the M value approaches the critical level, the period of autooscillations decreases.

Figure 4 shows the region of existence of the autooscillation regime (phase diagram) in the M versus J_{in} coordinates. In the presence of noises, the jumplike transitions from one regime to another may take place before the system can reach the point of stability loss. In this case, the period and amplitude of autooscillations are no longer constant and vary in a random manner around certain average values.

REFERENCES

1. S. D. R. Wilson, J. Fluid Mech. **190**, 561 (1988).

2. A. S. Skotnikov and T. B. Kholina, Khim. Prom–st (Moscow), No. 5, 44 (1985).

3. V. F. Dunskiĭ and N. V. Nikitin, Zh. Prikl. Mekh. Tekh. Fiz., No. 1, 49 (1980).

4. A. I. Grigor'ev, A. A. Zemskov, and S. O. Shiryaeva, Nauchn. Priborostr. **1** (2), 50 (1991).

5. R. Finn, *Equilibrium Capillary Surfaces* (Springer-Verlag, New York, 1986; Mir, Moscow, 1989).

6. A. V. Melkikh and V. D. Seleznev, Pis'ma Zh. Tekh. Fiz. **25** (24), 30 (1999) [Tech. Phys. Lett. **25**, 983 (1999)].

Translated by P. Pozdeev

Axisymmetric Solutions for the Equations of Motion of a Dielectric Liquid with a Free Charged Surface

N. M. Zubarev

Institute of Electrophysics, Ural Division, Russian Academy of Sciences, Yekaterinburg, Russia
e-mail: nick@ami.uran.ru
Received August 30, 2000

Abstract—Evolution of a boundary of the ideal dielectric liquid with a free charged surface is described in the limiting case of large surface curvature. Particular axisymmetric solutions of the equations of motion are obtained, which describe a paraboloidal boundary drawn inward the liquid at a constant velocity. © *2001 MAIK "Nauka/Interperiodica".*

As is known [1, 2], the flat boundary of a dielectric liquid possessing a free surface charge of sufficiently large density is unstable. The instability development in this system may lead to the boundary being drawn into the liquid [3] and, hence, to the loss of charge from the surface. Below we will demonstrate particular solutions to the equations of motion which describe the evolution of a paraboloidal perturbation of the liquid boundary. These results refer to the limiting case of a large surface curvature, when the approach based upon construction of the amplitude equations [2, 4] becomes inapplicable.

Let us consider a potential motion of the ideal dielectric liquid with a density ρ, occupying a region bounded by the free surface $z = \eta(x, y, t)$. The electric field potential in the medium $\varphi(x, y, z, t)$ and the liquid velocity potential $\Phi(x, y, z, t)$ satisfy the Laplace equations

$$\nabla^2 \varphi = 0, \quad \nabla^2 \Phi = 0, \tag{1}$$

which have to be solved together with the kinematic and dynamic boundary conditions

$$\eta_t = \Phi_z - \nabla_\perp \eta \nabla_\perp \Phi, \quad z = \eta(x, y, t), \tag{2}$$

$$\Phi_t = -\frac{1}{2}|\nabla \Phi|^2 - \frac{1}{8\pi\rho}|\nabla \varphi|^2, \quad z = \eta(x, y, t); \tag{3}$$

the condition of equipotentiality of the liquid surface in the presence of the surface charge,

$$\varphi = 0, \quad z = \eta(x, y, t); \tag{4}$$

and the condition of attenuation of the electric field strength and the velocity field at infinite distance from the liquid surface (in the case of infinitely deep liquid layer),

$$|\nabla \varphi| \longrightarrow 0, \quad |\nabla \Phi| \longrightarrow 0, \quad z \longrightarrow -\infty. \tag{5}$$

Note that Eq. (3) is written in the approximation in which both the electrostatic pressure over the liquid

surface and the capillary pressure are small in comparison to the electrostatic pressure under the surface. The validity of this approximation will be considered below.

In a previous study [5] devoted to the motion of a charged surface of liquid helium in a strong electric field, it was shown that the set of Eqs. (1)–(5) is compatible with the condition $\sqrt{4\pi\rho}\,\Phi = \varphi$. Moreover, this relationship between the two potentials reveals the unstable solutions of the initial set of equations, which are of most importance from the standpoint of physics. In this study, we will consider the simplest axisymmetric perturbations of the free liquid surface, which correspond to the substitution

$$\sqrt{4\pi\rho}\,\Phi(x, y, z, t)$$
$$= \varphi(x, y, z, t) = \tilde{\varphi}(u(x, y, z, t)), \tag{6}$$

$$u(x, y, z, t) = -z - Vt + \sqrt{x^2 + y^2 + (z + Vt)^2}, \tag{7}$$

where V is a constant. A physical meaning of this quantity is the velocity of the surface being drawn into the liquid (see [6], where a similar substitution was used to obtain axisymmetric solutions of the Stefan problem). As can be readily seen, the equipotential surfaces corresponding to Eqs. (6) and (7) represent a family of confocal paraboloids of rotation

$$x^2 + y^2 = 2u(z + Vt) + u^2. \tag{8}$$

Substituting expressions (6) and (7) into the initial set of equations (1), we eventually arrive at the ordinary differential equation

$$u\tilde{\varphi}_{uu} + \tilde{\varphi}_u = 0. \tag{9}$$

According to (2)–(4), the boundary conditions for this equation are as follows:

$$\tilde{\varphi}_u(u_0) = \sqrt{\pi\rho}\,V, \quad \tilde{\varphi}(u_0) = 0, \tag{10}$$

where u_0 is the value of the parameter u on the liquid surface. In what follows, we will use the reciprocal quantity $K = 1/u_0$ representing, as is seen from Eq. (8), the curvature of the free liquid surface on the symmetry axis. Jointly solving Eqs. (9) and (10), we obtain

$$\tilde{\varphi}(u) = \sqrt{\pi \rho}\, V \ln(Ku)/K, \qquad (11)$$

which, together with Eq. (7), describes the time evolution of the electric field potential. It is easy to see that conditions (5) are also naturally fulfilled. The shape of the liquid surface corresponding to the above exact solution of the equations of motion is described by the relationship

$$\eta(x, y, t) = K(x^2 + y^2)/2 - Vt - (2K)^{-1},$$

which represents a depression in the surface which is drawn inward the liquid.

For a real configuration, in which the thickness of the dielectric liquid layer D is finite and the potential difference between the charged surface and bottom of the liquid (metal substrate) is U, we obtain from Eq. (11) for $DK \gg 1$

$$V = \frac{UK}{\sqrt{\pi\rho}\ln(DK)}. \qquad (12)$$

This result indicates that the velocity of the surface being drawn inward the liquid is a linear function of the potential difference and the surface curvature (a weak logarithmic dependence on K in the denominator of this formula can be ignored) and slowly (logarithmically) decreases with increasing thickness D.

Now let us consider the question concerning the applicability of the nonstationary Bernoulli equation (3). As can be readily obtained from Eqs. (7), (10), and (12), the maximum field strength on the surface is

$$E = \frac{2UK}{\ln(DK)}.$$

This relationship implies that the electrostatic pressure is proportional to $P_E \sim E^2 \sim K^2/(\ln K)^2$. At the same time, the pressure at the liquid surface is $P_L \sim K$. Evidently, for a sufficiently large surface curvature $P_E \gg P_L$ and the capillary effects can be ignored. It is also obvious for large K that the field strength over the boundary

(i.e., in a depression on the equipotential surface) will be negligibly small (as a result of screening) as compared to the field strength beneath the boundary (near the depression vertex). This implies that the dynamic boundary condition in the form of Eq. (3) is applicable.

Thus, we have obtained particular axisymmetric solutions to the problem of motion of a charged equipotential surface drawn inward a dielectric liquid. We also determined the dependence of the velocity of the drawing on the problem parameters. It is important to note that the obtained solutions are not limited by a condition of small surface perturbations (as was the case in [2, 4]). On the contrary, these solutions describe the evolution of a localized surface perturbation possessing a significant curvature. Nevertheless, the obtained particular solutions should not be considered as the general case solutions. It is more likely that the blow-up-type solutions will dominate, for which the surface exhibits infinite sharpening within a finite time interval. However, methods for constructing such solutions are developed only for the problem in a planar geometry, where the conformal mapping formalism is applicable.

REFERENCES

1. J. R. Melcher, *Field-coupled Surface Waves* (MIT Press, Cambridge, 1963).

2. L. P. Gor'kov and D. M. Chernikova, Dokl. Akad. Nauk SSSR **228** (4), 829 (1976) [Sov. Phys. Dokl. **21**, 328 (1976)].

3. V. P. Volodin, M. S. Khaĭkin, and V. S. Édel'man, Pis'ma Zh. Éksp. Teor. Fiz. **26** (10), 707 (1977) [JETP Lett. **26**, 543 (1977)].

4. H. Ikezi, Phys. Rev. Lett. **42**, 1688 (1979).

5. N. M. Zubarev, Pis'ma Zh. Éksp. Teor. Fiz. **71** (9), 534 (2000) [JETP Lett. **71**, 367 (2000)].

6. G. P. Ivantsov, Dokl. Akad. Nauk SSSR **LVIII** (4), 567 (1947).

Translated by P. Pozdeev

Nonlinear Magnetization Reversal in Copper–Permalloy Composite Wires Induced by a High-Frequency Current

A. S. Antonov*, N. A. Buznikov*, A. F. Prokoshin**, A. L. Rakhmanov*, I. T. Iakubov**, and A. M. Yakunin**

* Institute of Theoretical and Applied Electrodynamics, Russian Academy of Sciences, Moscow, Russia
** Central Research Institute of Ferrous Metallurgy, Russian Academy of Sciences, Moscow, Russia
e-mail: n_buznikov@mail.ru
Received November 8, 2000

Abstract—The phenomenon of magnetization reversal in copper–permalloy composite wires induced by a high-frequency ac current field was studied. The frequency spectrum of a voltage measured in the probing coil wound on the wire contains only even harmonics in a broad range of amplitudes of the ac excitation current and the bias magnetic field strength. The amplitude of the even harmonics measured is highly sensitive with respect to the bias field. The results can be used to develop weak magnetic field sensors. © *2001 MAIK "Nauka/Interperiodica".*

The effect of giant magnetoimpedance (GMI), whereby the impedance of a conductor exposed to an applied magnetic field exhibits a very strong variation, was extensively studied in the past decade. The interest of researchers is related to the possibility of using this phenomenon for creating highly sensitive magnetic field sensors [1]. The GMI effect was observed in amorphous wires [2–4] and ribbons [5], multilayer film structures [6–8], and glass-coated microwires [9, 10]. In addition, the effect also takes place in composite wires comprising a highly conducting core and a magnetically soft sheath [10–13]. As was demonstrated [14], the presence of the highly conducting core in a composite wire may lead to a significant increase in the GMI amplitude.

The linear GMI effect can be observed at a sufficiently small amplitude of the ac excitation current, in which case the response signal is proportional to the sample impedance. An increase in the current amplitude gives rise to a nonlinear magnetization reversal process, which is accompanied by the appearance of a nonlinear response voltage between the conductor ends or in the probing coil wound around the sample [11, 15, 16]. Since the nonlinear response is highly sensitive with respect to the applied magnetic field, the nonlinear magnetization reversal is also a promising phenomenon from the standpoint of technological applications.

In this work, the nonlinear magnetization reversal in copper–permalloy composite wires exposed to a high-frequency current field was studied by experimental and theoretical methods. In particular, the frequency spectrum of a voltage induced in the probing coil wound around the wire sample was measured. It was found that amplitudes of the even harmonics induced in the probing coil are highly sensitive to the longitudinal bias magnetic field strength. The experimental results were described within the framework of a quasistatic Stoner–Wohlfarth model [17].

The copper–permalloy composite wires were prepared by a method involving compressing, drawing, and annealing the initial composite material. The copper rod with a diameter of 0.67 cm was confined inside a permalloy tube with a diameter of 1 cm. Upon drawing the composite rod, the wires were annealed in vacuum for 1–3 h at a temperature from 750 to 1000°C and a residual pressure of 10^{-3} Pa [12]. The copper core diameter d ranged from 20 to 120 μm, and the permalloy sheath thickness fell within 10–40 μm. The core to composite wire diameter ratio d/D was approximately 2/3 in all samples. The sample wire length varied from 0.5 to 2 cm. The permalloy sheath exhibited a circular anisotropy; the anisotropic field H_a of the wire samples studied fell within 1–5 Oe. The saturation magnetization M of the wires was about 800 G [12].

The nonlinear magnetization reversal process was studied by passing a high-frequency current of sufficiently large amplitude through the composite wires. The ac current amplitude reached 0.25 A, while the frequency f was varied from 0.1 to 1 MHz. The wire was placed into a constant longitudinal magnetic field H_e generated by a solenoid oriented along the wire axis. The H_e value was varied from 0 to 50 Oe. A probing coil with the number of turns N varied from 40 to 130 was wound directly around the wire. The amplitudes of the voltage harmonics V_φ induced in the probing coil
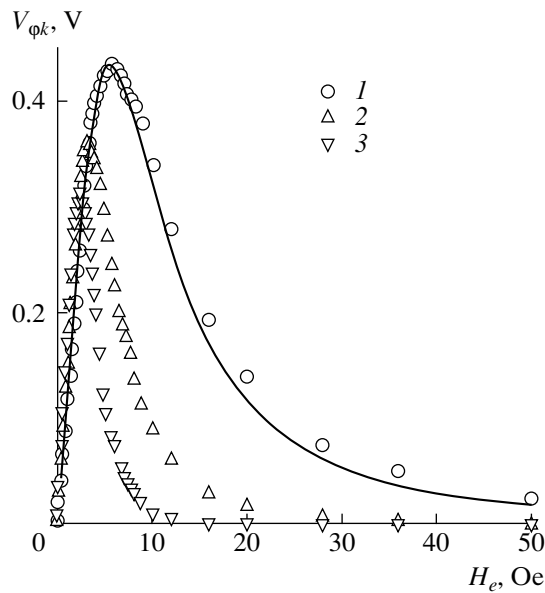
$V_{\varphi k}$, V

Fig. 1. The experimental plots of response signal amplitude $V_{\varphi k}$ versus bias magnetization field strength H_e measured at $f = 315$ kHz and $I_0 = 0.19$ Å for various even harmonics $k = 2$ (*1*), 4 (*2*), 6 (*3*). Solid curve shows the results of calculation of $V_{\varphi 2}$ as a function of H_e by Eq. (2) for $H_a = 3.5$ Oe, $M = 820$ G, $d = 66$ μm, $D = 100$ μm, $l = 0.9$ cm, and $N = 110$.
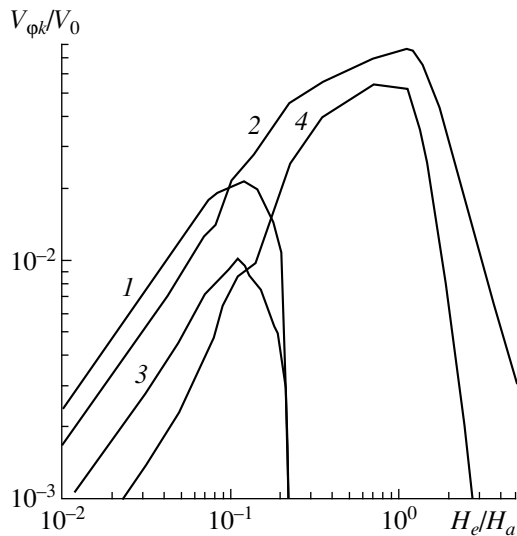

Fig. 2. The plots of response signal amplitude $V_{\varphi k}$ versus bias magnetization field strength H_e calculated by Eq. (2) with $4I_0/cDH_a = 0.5$, $d/D = 2/3$ for various harmonics $k = 1$ (*1*), 2 (*2*), 3 (*3*), 4 (*4*).

were measured using a Hewlett Packard Model 4395A spectrum analyzer.

When the current amplitude I_0 and the bias magnetic field strength H_e are small, a dominating component in the frequency spectrum is the first harmonic. As soon as the bias field strength H_e exceeds a certain threshold value (dependent on I_0), the odd harmonics disappear

and the second harmonic becomes predominant. For a sufficiently large I_0, the frequency spectrum contains only even harmonics irrespective of the H_e value. Figure 1 shows typical plots of the first even harmonic amplitudes $V_{\varphi k}$ (k is the harmonic number) versus bias magnetic field strength H_e. As can be seen, all the even harmonic amplitudes initially increase with H_e, pass through a maximum, and then rather slowly decrease.

In order to describe the experimental results, let us consider a simple model capable of explaining the main features of the frequency spectrum of response voltage in the probing coil. It is assumed that the permalloy sheath possesses no domain structure and the current flows only in the copper core because the conductivity of copper is considerably greater than that of permalloy. The circular magnetic field H_φ induced by the ac current $I = I_0 \sin(2\pi ft)$ leads to variations in the circular magnetization component M_φ and, hence, in the longitudinal magnetization component M_z. According to the Faraday law, this results in the appearance of induced voltage in the probing coil. Since the current frequency is relatively small, the magnetization reversal process can be described within the framework of the quasistatic Stoner–Wohlfarth model [11, 16, 18].

In the quasistatic approximation, minimization of the free energy leads to the following equation for the circular magnetization component M_φ:

$$(1 - m_\varphi^2)[m_\varphi + h_0\rho^{-1}\sin(2\pi ft)]^2 = h_e^2 m_\varphi^2, \quad (1)$$

where $m_\varphi = M_\varphi/M$, $h_e = H_e/H_a$, $h_0 = 4I_0/cDH_a$ is a dimensionless amplitude of the circular field, and $\rho = 2r/D$ is a dimensionless radial coordinate. For small amplitudes of the circular field and $H_e < H_a$, the circular magnetization M_φ depends on H_φ in a reversible manner. When the ac current field amplitude exceed a certain threshold, this dependence acquires the shape of a curve with hysteresis and the Barkhausen jumps. Since a characteristic time of the Barkhausen jumps is on the order of 10^{-9} s, we may neglect their contribution to amplitudes of the first harmonics of the response voltage. Then, the voltage V_φ in the probing coil is given by the expression [18]:

$$V_\varphi = V_0 h_0 \cos(2\pi ft)$$
$$\times \int_{d/D}^{1} \frac{m_\varphi^2(1 - m_\varphi^2)d\rho}{h_e m_\varphi^3 + h_0\rho^{-1}\sin(2\pi ft)(1 - m_\varphi^2)^{3/2}}, \quad (2)$$

where $m_\varphi = m_\varphi(\rho, t)$ is a solution to Eq. (1) and $V_0 = 4\pi^3 D^2 NMf/c$. According to formula (2), the dimensionless voltage $v_\varphi = V_\varphi/V_0$ is a function of three parameters: h_0, h_e, and d/D.

Figure 2 shows the plots of harmonic amplitudes $V_{\varphi k}$ versus the bias magnetic field strength H_e calculated using the Fourier transform of Eq. (2). As can be seen, the first harmonic dominates in the frequency spectrum

for small H_e values. When the bias field strength H_e exceeds the threshold value

$$H_c = H_a[1 - (4I_0/cDH_a)^{2/3}]^{3/2}, \qquad (3)$$

the odd harmonics vanish, while the second harmonic starts dominating in the spectrum. The even harmonic amplitudes reach a maximum for $H_e \cong H_a$ and then sharply drop as well.

Thus, the proposed model is capable of describing the main features of the frequency spectrum of response voltage in the probing coil. Figure 1 shows a comparison between the measured and calculated values of the second harmonic amplitude $V_{\varphi 2}$ as function of the bias magnetic field strength H_e. It should be pointed out that the calculated values significantly depend on the selected anisotropic field H_a and the saturation magnetization M. The best coincidence between calculated and measured values was obtained for $H_a = 3.5$ Oe and $M = 820$ G.

In conclusion, it should be noted that the amplitudes of even harmonics are highly sensitive to the bias magnetic field strength. For example, The characteristic sensitivity coefficient of the second harmonic amplitude in the samples studied was on the order of 10^{-1} V/Oe for $f = 315$ kHz and $I_0 = 0.19$ A. This level, coinciding with the maximum sensitivity attained using the GMI effect, can even be increased by using higher frequencies and current amplitudes. Additional increase in the sensitivity can be ensured by optimizing the wire parameters, that is, by increasing the ferromagnetic sheath thickness and decreasing the anisotropic field strength. Therefore, the process of nonlinear magnetization reversal in composite wires is a promising effect to be implemented in weak magnetic field sensors.

REFERENCES

1. M. Vázquez and A. Hernando, J. Phys. D **29** (4), 939 (1996).

2. K. Mohri, T. Kohzawa, K. Kawashima, *et al.*, IEEE Trans. Magn. **28** (5), 3150 (1992).

3. R. S. Beach and A. E. Berkowitz, Appl. Phys. Lett. **64** (26), 3652 (1994).

4. L. V. Panina and K. Mohri, Appl. Phys. Lett. **65** (9), 1189 (1994).

5. F. L. A. Machado, C. S. Martins, and S. M. Rezende, Phys. Rev. B **51** (6), 3926 (1995).

6. M. Senda, O. Ishii, Y. Koshimoto, and T. Tashima, IEEE Trans. Magn. **30** (6), 4611 (1994).

7. K. Hika, L. V. Panina, and K. Mohri, IEEE Trans. Magn. **32** (5), 4594 (1996).

8. A. S. Antonov, S. N. Gadetskiĭ, A. B. Granovskiĭ, *et al.*, Fiz. Met. Metalloved. **83** (6), 60 (1997).

9. M. Vázquez, A. P. Zhukov, P. Aragoneses, *et al.*, IEEE Trans. Magn. **34** (3), 724 (1998).

10. M. Vázquez, M. García-Beneytez, J. M. García, *et al.*, in *Proceedings of the Moscow International Symposium on Magnetism* (Mosk. Gos. Univ., Moscow, 1999), Part 1, pp. 259–266.

11. R. S. Beach, N. Smith, C. L. Platt, *et al.*, Appl. Phys. Lett. **68** (19), 2753 (1996).

12. A. S. Antonov, A. L. Rakhmanov, N. A. Buznikov, *et al.*, IEEE Trans. Magn. **35** (5), 3640 (1999).

13. G. V. Kurlyandskaya, V. O. Vas'kovskiĭ, H. García-Migel, and M. Baskes, in *Proceedings of the XVII International School-Workshop "Novel Magnetic Materials in Microelectronics"* (Mosk. Gos. Univ., Moscow, 2000), p. 666.

14. N. Usov, A. Antonov, and A. Granovsky, J. Magn. Magn. Mater. **171** (1-2), 64 (1997).

15. A. Yelon, M. Britel, D. Menard, and P. Ciureanu, Physica A (Amsterdam) **241** (1-2), 439 (1997).

16. A. S. Antonov, N. A. Buznikov, I. T. Iakubov, *et al.*, in *Proceedings of the Moscow International Symposium on Magnetism* (Mosk. Gos. Univ., Moscow, 1999), Part 2, p. 252.

17. E. S. Stoner and E. P. Wohlfarth, Philos. Trans. R. Soc. London, Ser. A **240**, 599 (1948).

18. A. S. Antonov, N. A. Buznikov, A. N. Lagar'kov, *et al.*, Élektrichestvo, No. 4, 52 (2000).

Translated by P. Pozdeev

A Physical Model of the Oxygen Subsystem Evolution in PLZT Ceramics under Neutron Irradiation and Annealing

D. V. Kulikov*, D. A. Lesnyh*, Yu. V. Trushin*, H. W. Weber**, K. Humer, R. Bittner, and A. R. Sternberg***

* Ioffe Physicotechnical Institute, Russian Academy of Sciences, St. Petersburg, 194021 Russia
** Atomic Institute of Austrian Universities, Vienna, Austria
*** Institute of Solid State Physics, University of Latvia, Riga, Latvia
e-mail: trushin@natalie.ioffe.rssi.ru
Received November 28, 2000

Abstract—A physical model describing the evolution of defects in the oxygen subsystem of ferroelectric PLZT ceramics under neutron irradiation and isochronous annealing conditions is proposed. The model takes into account the dependence of the material properties on the lanthanum content. The oxygen vacancy concentration variations calculated using this model agree with the experimental data on the polarization behavior in annealed ceramics. © 2001 MAIK "Nauka/Interperiodica".

Introduction. At present, ferroelectric materials are being actively introduced into modern technologies. Transparent ferroelectric ceramics are promising materials for optoelectronic devices working in the IR range. PLZT ceramics can be employed in radiant power detectors of the bolometer type. In some applications, such as thermonuclear reactors, the electronic devices have to operate under significant background radiation conditions. Therefore, it is necessary to study the behavior of ferroelectric materials under the conditions of exposure to high-energy radiation; a related problem is the possibility of restoring the radiation-damaged material properties by thermal annealing.

Previously [1, 2], the effect of high-energy radiation (neutron, electrons, γ-quanta) on the properties of ferroelectric $Pb_{1-Z}La_ZZr_YTi_{1-Y}O_3$ (PLZT) ceramics was studied for the $X/65/35$ compositions where $X = 4.5-11$ at. % is the lanthanum content; the zirconium and titanium content being 65 and 35 at. %, respectively. It was demonstrated that neutron irradiation leads to a considerable decrease in the spontaneous polarization and dielectric permittivity values of the ceramics, irrespective of the composition [1, 2] (i.e., of the lanthanum doping). After irradiation, the samples were subject to isochronous annealing, with the temperature increased at a rate of 2 K/min. It was found that the behavior of ceramics during annealing depends on the composition: the dielectric properties of samples with different content of lanthanum began to restore at various temperatures.

It is known that variation of the La content in PLZT ceramics affects the structure and properties of the material [1–3]. Viehland [3] showed that a phase transition takes place in the region of a La concentration between 6 and 8 at. %, whereby the initial micron-sized domains in the material vanish and the so-called polaron nanodomains appear with a size of about 50 Å.

Recently [4, 5], we proposed a physical model describing the evolution of defects in the oxygen subsystem of ferroelectric PLZT ceramics under neutron irradiation and isochronous annealing conditions and the influence of defects on the material polarization. A model calculation of the concentration of defects in the oxygen subsystem of the samples annealed upon the irradiation to small fluences showed satisfactory agreement with experiment [1, 2]. The purpose of this work was to develop the physical model [4, 5] so as to render this theory applicable to the case of high neutron irradiation doses and greater lanthanum contents in the ceramics.

Model formulation and application. Now we can formulate the following refined physical model describing evolution of the oxygen defects in PLZT ceramics with various lanthanum contents in the course of neutron irradiation and subsequent annealing.

1. According to Park and Chadi [6], the tetragonal phase of lead titanate ($PbTiO_3$) contains oxygen vacancies of two types (V^u and V^s) in the Ti–O–Ti chains, which differently affect the polarization:

(i) Atoms in the vicinity of a V^u vacancy exhibit relaxation such that their dipole moments along the c-axes of the neighboring crystal lattice cells "above" and "below" the vacancy are oriented in opposite directions [2, 5];

(ii) The relaxation of atoms in the lattice near V^s vacancies does not alter the polarization.

2. It is assumed that a potential minimum for vacancies of the V^s type is lower than the minimum for the V^u vacancies. This can be related to the fact that the above relaxed atomic configuration corresponding to the

opposite polarization orientations is energetically less favorable than that with like polarizations.

3. It is suggested that vacancies may pass from one state (V^u) to another (V^s) and back upon surmounting certain potential barriers (ε_{us} and ε_{su}). In accordance with point 2, the transition from V^u to V^s is easier than the reverse transition ($\varepsilon_{us} < \varepsilon_{su}$).

4. Proceeding from the results of Park and Chadi [6] (see pp. 1–3 above), we assume that neutron irradiation of the PLZT ceramics leads to the formation of oxygen vacancies of the V^u type corresponding to a decrease in the polarization. On annealing, vacancies of this type may either recombine with interstitial oxygen atoms or pass to the V^s sate (and back), which leads eventually to the restoration of the initial polarization level.

5. We suggest that a change in the content of La in PLZT ceramics (influencing the material structure [6]) may also affect the transitions between various vacancy states. An increase in the La content, accompanied by the formation of small-size nanodomains, leads to a decrease in the energy barriers for transitions from V^u to the V^s state and back (as compared to the barrier height in the samples with a lower La concentration). This can be related to the fact that a change in the polarization direction (accompanying the vacancy transitions) more readily takes place in small nanodomains than in micron-sized regions.

6. We believe that the domain boundaries serve as the sinks for interstitial oxygen. The higher the La content, the smaller the size of domains [3] and the shorter the distance between their boundaries, which increases the sink capacity S_i.

7. We assume that the interstitial oxygen atoms may overcome the potential barrier (ε_{is}) and leave the sinks in the course of annealing at high temperatures.

In order to describe the evolution of defects in the oxygen subsystem of neutron-irradiated PLZT ceramics in the course of subsequent annealing, we consider a system of the kinetic balance equations (see, e.g., [7, 8]) written with an allowance for the above processes:

$$\frac{\partial C_{vs}(t)}{\partial t} = -\mu(D_i + D_v)C_i C_{vs} + \chi_{us}C_{vu} - \chi_{su}C_{vs}, \quad (1)$$

$$\frac{\partial C_{vu}(t)}{\partial t} = -\mu(D_i + D_v)C_i C_{vu} - \chi_{us}C_{vu} + \chi_{su}C_{vs}, \quad (2)$$

$$\frac{\partial C_i(t)}{\partial t} = -\mu(D_i + D_v)C_i(C_{vu} + C_{vs}) \\ - D_i C_i S_i + \chi_{is}C_{is}, \quad (3)$$

$$\frac{\partial C_{is}(t)}{\partial t} = D_i C_i S_i - \chi_{is}C_{is}. \quad (4)$$

Here $C_{vu}(t)$ and $C_{vs}(t)$ are the time-dependent relative concentrations (per unit cell) of oxygen vacancies of the V^u and V^s types, respectively; $C_i(t)$ and $C_{is}(t)$ are
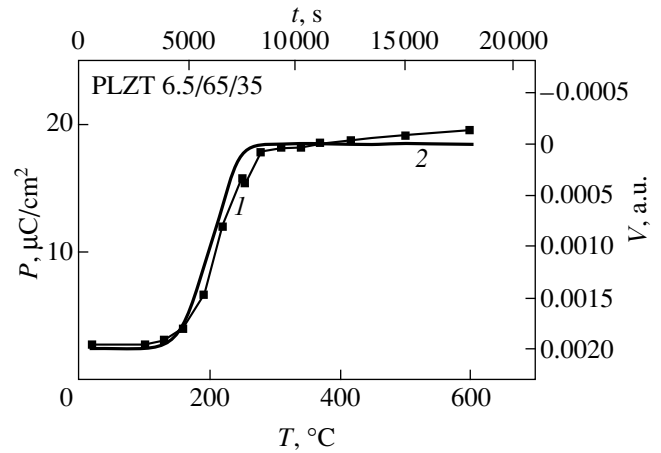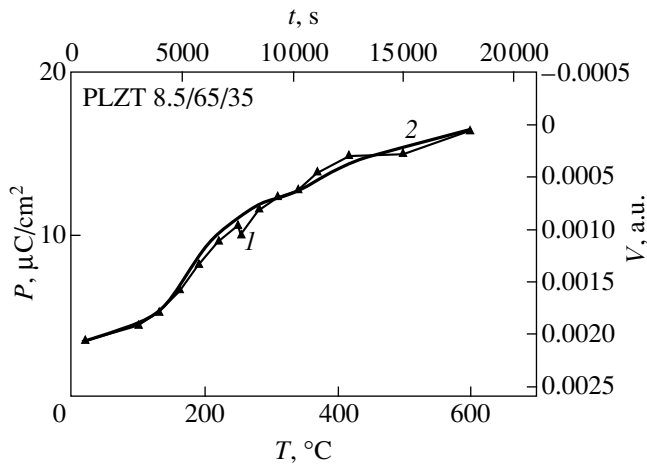

Fig. 1. The plots of oxygen vacancy concentration $C_{vu}(t)$ and experimental polarization values versus time of isochronous annealing for PLZT ceramics containing 6.5% La: (*1*) experimental points; (*2*) calculated curve.

the relative concentrations of interstitial oxygen—free and trapped on sinks—respectively; $\mu = 4\pi r_R$, r_R being the recombination parameter ($r_R \approx a$, where $a = 4$ Å is the lattice parameter); $D_j = D_0 \exp(-\varepsilon_j^m/kT)$ is the diffusion coefficient, ε_j^m being the activation energy for the migration of oxygen defects of the jth type (j = vs, vu, i); χ_l is the probability parameter for the oxygen vacancy transitions from V^u to V^s state and back, l = su, us; χ_{is} is the probability parameter for the interstitial oxygen to leave a sink; the oxygen transition probabilities are given by the relationship $\chi_l = \nu^* \exp(-\varepsilon_l/kT)$, where ν is the frequency of oxygen jumps between interstitial sites (on the order of the Debye frequency), l = us, su, is.

Model application and results. The calculations were performed for the following values of parameters:

(i) $\varepsilon_j^m = 1.7$ eV (j = vs, vu, i) [4, 5];

(ii) $\nu \approx 3 \times 10^{11}$ s^{-1} (the exact value is unknown, but this frequency must be close to the value reported for an YBaCuO superconductor structurally close to the PLZT ceramics [8]);

(iii) $S \approx 1/L^2$, where L is on the order of a half domain size (for a sample containing 6.5% La, $L \approx 10^{-5}$ cm and the sink capacity is $S \approx 10^{10}$ cm^{-2}; for a sample with 8.5% La, $L \approx 2 \times 10^{-7}$ cm and $S \approx 3 \times 10^{13}$ cm^{-2}, see [3]).

The values of potential barriers for the oxygen vacancy transitions between V^u and V^s states were selected as follows:

(iv) For the sample containing 6.5% La, we took $\varepsilon_{us} = 1.45$ eV [4, 5] and $\varepsilon_{su} = 1.7$ eV (this implies that the $V^s \longrightarrow V^u$ transition is forbidden, as was previously assumed for PLZT ceramics containing 4.5 and 7% La [5]);

Fig. 2. The plots of oxygen vacancy concentration $C_{vu}(t)$ and experimental polarization values versus time of isochronous annealing for PLZT ceramics containing 8.5% La: (*1*) experimental points; (*2*) calculated curve.

(v) For the sample containing 8.5% La, the ε_{us} and ε_{su} values were considered as variable parameters because no data on these energies are available. Another variable quantity was the potential barrier ε_{is} for an interstitial oxygen atom leaving a sink.

(vi) The initial defect concentrations in PLZT ceramics irradiated with neutrons to a total dose of 2×10^{18} n cm^{-2} were determined using the TRIRS program [4, 5, 9] to be $C_{vs}(0) = 10^{-3}$, $C_{vu}(0) = 2 \times 10^{-3}$, and $C_i(0) = 3 \times 10^{-3}$.

Thus, the relative content of C_{vu} in the irradiated ceramics was approximately 10^{-3}; this is equivalent to one vacancy per 1000 lattice cells, or one vacancy contained in a cube with a side length of $10a$ (in this cube, the polarization has a configuration depicted in [5, Figs. 2c and 2d], whereby the polarization components have opposite directions on different sides of the vacancy to yield almost zero upon summation). During annealing at various temperatures (for the samples with different La content), the concentration of vacancies in the V^u state (C_{vu}) decreases due to recombination of these vacancies or their passage to the V^s state, which leads to an increase in the degree of polarization.

Results and discussion. The system of Eqs. (1)–(4) was solved by numerical methods. Figures 1 and 2 show the results of calculations for the oxygen vacancy concentrations in the V^u state (decreasing the polarization) for the samples containing 6.5 and 8.5% La, respectively. Also presented in these figures are the experimental data (taken from [2]) on the polarization variation in the course of annealing.

A satisfactory agreement of the experimental data and the results of calculation for the ceramics containing 6.5% La (Fig. 1), allows us to evaluate the potential barriers for the transition of vacancies between V^u and

V^s states ($\varepsilon_{us} = 1.38$ eV, $\varepsilon_{su} = 1.42$ eV) and for the interstitial oxygen leaving a sink ($\varepsilon_{is} = 2.2$ eV); these values provide for the best coincidence between theory and experiment. As can be seen, the possibility for the vacancies to pass from V^u to the V^s state and back (see point 3 of the model) results in that the concentration of vacancies in the V^u state decreases, which proceeds at a slower rate in the ceramics containing 8.5% La than in the samples with 6.5% La (Figs. 1 and 2) or 4.5% La [14, 5].

Conclusion. Thus, we proposed a physical model describing the evolution of defects in the oxygen subsystem of ferroelectric PLZT ceramics in the course of neutron irradiation to various doses and subsequent annealing. The model explains changes in the crystal microstructure and the related variations in the material polarization. Using this model, we calculated the concentration of defects in the oxygen subsystem as a function of the annealing time, which satisfactorily agrees with experimental data on the polarization behavior. The refined model takes into account the dependence of the material structure and properties on the lanthanum content and the effect of oxygen vacancy concentration in various states on the sample polarization.

Based on the satisfactory coincidence of the calculated variation in the oxygen vacancy concentrations and the polarization behavior in annealed samples, we determined the values of potential barriers for the oxygen vacancy transitions between the V^u and V^s states and for the oxygen vacancy leaving the sink.

REFERENCES

1. A. Sternberg, L. Shebanov, E. Birks, *et al.*, in *Proceedings of the Fourth Conference of the European Ceramic Society "Euro-Ceramics," 1995*, Vol. 5, p. 233.
2. A. Sternberg, L. Shebanov, E. Birks, *et al.*, Ferroelectrics **183**, 301 (1996).
3. D. Viehland, X. H. Dai, J. F. Li, and Z. Xu, J. Appl. Phys. **84** (1), 458 (1998).
4. D. V. Kulikov, Yu. V. Trushin, V. S. Kharlamov, *et al.*, in *Proc. SPAS, 2000*, Vol. 4, Preprints and Program NDTCS-2000, pp. E15–E17.
5. D. V. Kulikov, Yu. V. Trushin, V. S. Kharlamov, *et al.*, Proc. SPIE (2001) (in press).
6. C. H. Park and F. J. Chadi, Phys. Rev. B **57** (22), R13961 (1998).
7. Yu. V. Trushin, *Theory of Radiation Processes in Metal Solid Solution* (Nova Science, New York, 1996).
8. D. V. Kulikov, R. A. Suris, and Yu. V. Trushin, Supercond. Sci. Technol. **8**, 303 (1995).
9. Yu. V. Trushin, B. J. Ber, V. S. Kharlamov, and E. E. Zhurkin, J. Nucl. Mater. **233**–**237**, 991 (1996).

Translated by P. Pozdeev

Spectral and Current–Voltage Characteristics of Si–Si$_{1-x}$Ge$_x$ Heterostructures Grown by Liquid Phase Epitaxy

A. S. Saidov, A. Kutlimratov, B. Sapaev, and U. T. Davlatov

Physical Engineering Institute, "Solar Physics" Research and Production Corporation,
Academy of Sciences of the Republic of Uzbekistan, Tashkent, Uzbekistan

Received November 1, 2000

Abstract—The spectral and current–voltage (*I–V*) characteristics of Si–Si$_{1-x}$Ge$_x$ heterostructures grown by liquid phase epitaxy on silicon substrates were studied. The dependence of the longwave photosensitivity boundary of these structures on the variband solid solution composition was determined. It is shown that these variband solid solutions can serve as transition buffer layers between silicon substrates and a structure based on a different semiconductor. These structures can be employed in elements converting a part of the IR solar radiation in cascade solar cells and in photodetectors for the optical fiber communication lines transmitting signals with the wavelengths λ = 1.33 and 1.5 μm. © *2001 MAIK "Nauka/Interperiodica".*

Silicon and silicon-based solid solutions are still among the most important materials in modern semiconductor electronics. This is related to the fact that silicon is a relatively cheap semiconductor material with a highly developed technology. In addition, silicon offers certain advantages over the other semiconductors, including properties such as low density, high thermal conductivity, sufficient mechanical strength, etc. [1–3].

Since the crystal lattice parameters of various semiconductor materials may significantly differ, it is frequently impossible to obtain device structures obeying all requirements of modern semiconductor electronics. In order to attain structural matching and ensure the obtainment of high-quality device structures (meeting the aforementioned requirements) on silicon substrates, it is common practice to grow intermediate (or transition) buffer layers between substrates and device heterostructures. Depending on the composition and type of the heterostructure, the buffer layers usually represent a substrate solid solution with variable composition, including elements of the subsequently grown film (i.e., of the working structure material). One representative of the solid solution systems for buffer layers is the series of Si$_{1-x}$Ge$_x$ variband solid solutions grown on Si substrates. In growing the device heterostructures on buffer layers, one must take into account that these transition layers may affect the output characteristic of the final devices. Therefore, the development of a technology to obtain semiconductor devices with high working characteristics must include a thorough investigation of the properties of buffer layers and their effects upon the parameters of heterostructures involving these layers.

Previously we reported on the conditions of obtaining variband solid solutions of the Si$_{1-x}$Ge$_x$ system by liquid phase epitaxy (LPE) on silicon substrates [4, 5]. Some properties of these solid solutions were reported in [6]. This work was devoted to studying the effect of the parameters of the Si$_{1-x}$Ge$_x$ epitaxial films on the spectral and current–voltage (*I–V*) characteristics of Si–Si$_{1-x}$Ge$_x$ heterostructures grown by LPE. It will be demonstrated that these heterostructures can be employed in practice as buffer layers, for example, in narrow-bandgap elements of cascade solar cells and in photodetectors for optical fiber communication lines (OFCLs) transmitting signals with the wavelengths λ = 1.3 and 1.55 μm [7].

The films of Si$_{1-x}$Ge$_x$ solid solutions were grown by LPE on (111)-oriented single crystal silicon wafers of the KEF-5 grade with a resistivity of ρ = 5.0 Ω cm. In order to study the effect of the solution melt composition on the properties of LPE heterostructures, the epitaxial films were grown using either gallium- or tin-based melts. For obtaining films with mirror surfaces and improved electrical characteristics the solution melt was doped with small amounts (below 1 at. %) of lead and aluminum [8].

A study of the morphology and Hall characteristics of the Si$_{1-x}$Ge$_x$ solid solution films showed that the samples grown by LPE from both gallium- and tin-based melts possess a conductivity of the acceptor type and a composition gradually varying from 100% Si at the heterojunction to 100% Ge on the epitaxial film surface. Accordingly, the bandgap width of the solid solution also smoothly varied from $E_{g,\,\mathrm{Si}}$ = 1.1 eV (near the substrate) to $E_{g,\,\mathrm{Ge}}$ = 0.71 eV on the film surface. Figure 1a shows an energy band diagram of the (*n*)Si–(*p*)Si$_{1-x}$Ge$_x$ hetero-
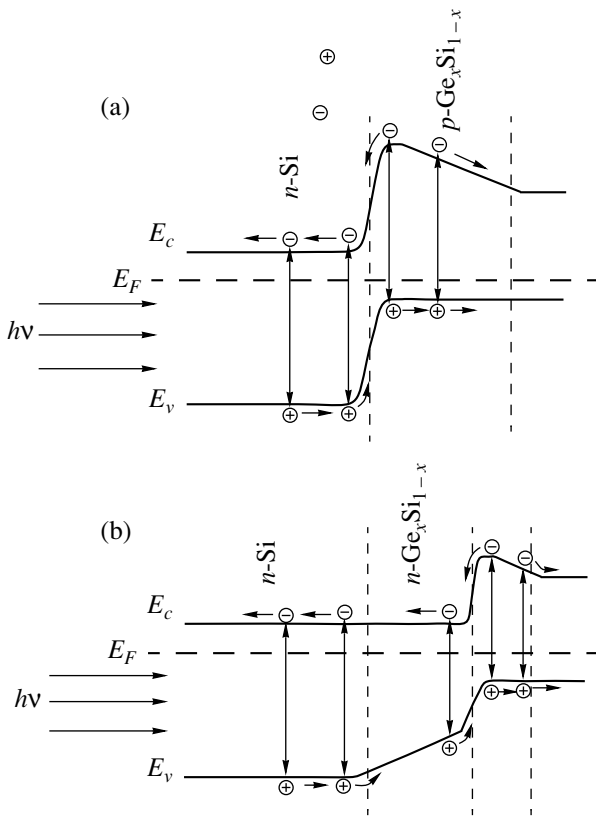
Fig. 1. Energy band diagrams of (a) (n)Si–(p)Si$_{1-x}$Ge$_x$ and (b) (n)Si–(n)Si$_{1-x}$Ge$_x$–(p)Si$_{1-x}$Ge$_x$ epitaxial heterostructures.

structure, which shows that the presence of a variband structure modifies the principal system parameters such as the resistivity ρ, the shallow acceptor (N_a) and shallow donor (N_d) concentrations, charge carrier mobility μ, and some others.

Figure 2 shows the plots of electron (μ_n) and hole (μ_p) mobility versus solid solution composition param-

eter x constructed by the Hall data. As can be seen, the μ_n and μ_p values gradually increase with the content of Ge atoms in the solid solution. This behavior is readily explained taking into account that the charge carrier mobilities in Ge are greater than those in Si (for a certain impurity concentration). Note that the growth in mobility with increasing x might be even greater if there were no opposite trend, whereby the mobility of charge carriers decreases with an increase in their concentration. As a result, the μ_n and μ_p values grow only slightly with x.
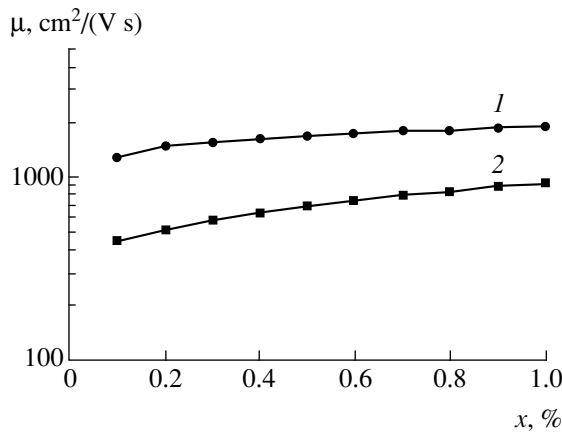
Figure 3 presents the plots of room-temperature resistivity ρ versus solid solution composition parameter x for the Si$_{1-x}$Ge$_x$ LPE films grown from gallium- and tin-based melts. The resistivity–composition profiles were measured by the four-point-probe method in combination with the layer-by-layer removal technique [9]. As is seen, the resistivity of the film grown from a tin melt is higher than that of the film obtained from the gallium melt. At the same time, in both cases the resistivity nonlinearly decreases with increasing Ge content in the solid solution composition, which is explained by increasing μ_n and μ_p values (Fig. 2) and by the fact that Sn and Ga atoms form deeper acceptor impurity levels in Si (0.27 and 0.072 eV) than in Ge (0.12 and 0.011 eV, respectively) [10].

In order to determine the range of spectral sensitivity of the (n)Si–(n)Si$_{1-x}$Ge$_x$–(p)Si$_{1-x}$Ge$_x$ heterostructure, we have studied the photoresponse of the samples in the short-circuit regime. The measurements were performed using an MDR-4 monochromator and a 100-W halogen lamp supplied from a stabilized power supply unit of the B5-20 type. The samples were illuminated from the substrate side. The spectrum was calibrated using a standard silicon photodetector with a known spectral characteristic.

Figure 4 presents typical spectral characteristics of the (n)Si–(p)Si$_{1-x}$Ge$_x$ heterostructure grown from gallium- and tin-based melts. An analysis of these data

Fig. 2. The plots of (*1*) electron and (*2*) hole mobilities versus Ge$_x$Si$_{1-x}$ solid solution composition parameter x.
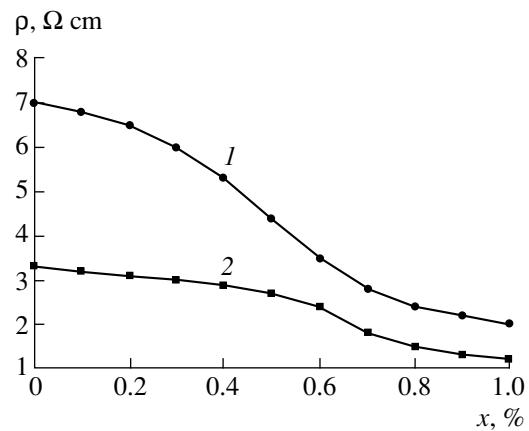

Fig. 3. The plots of room-temperature resistivity ρ versus solid solution composition parameter x for the Si$_{1-x}$Ge$_x$ variband solid solution films grown from (*1*) gallium- and (*2*) tin-based melts.

shows that the sample structure obtained from the gallium melt exhibits inversion of the photoresponse sign for $\lambda = 930$ and 820 nm. A similar result was previously reported by Donnelly and Milnes [11] for anisotypic sharp (n)Si–(p)Ge heterojunctions, where the photoresponse sign inversion was observed at $\lambda = 1.2$ and 1.8–1.9 μm. Van Opdorp and Vrakking [12] explained this phenomenon by the interband transitions in Ge and Si and by the photoemission of electrons from states at the interface and from the valence band of Ge into the conduction band of Si. The properties of these structures were described by a model representing the heterojunction as a pair of inversely connected diodes.

The fact that the photoresponse sign inversion in our experiments was observed at $\lambda = 930$ and 820 nm (Fig. 4), is related to the fact that our heterostructures, in contrast to those studied by Donnelly and Milnes [11], are smooth rather than sharp. As is seen from Fig. 4, the photoresponse of LPE heterostructures grown from the tin melt exhibits no points of sign inversion, which is probably explained by a relatively high density of states at the heterojunction from substrate to epitaxial film. Accordingly, a contribution to the photo emf is provided only by the electron–hole pairs photogenerated at a distance from the p–n junction that is shorter than the diffusion length Ld of nonequilibrium charge carriers (see Fig. 1).

As can be seen in Fig. 1, most photons penetrating through the Si substrate are absorbed within the variband solid solution layer with the bandgap width corresponding to a higher quantum energy ($h\nu \geq E_g$). Because of the entraining effect of a quasi-electric pulling field, related to the variband character of the layer, electrons generated outside of the space-charge region cannot contribute to the photo emf. Therefore, the $Si_{1-x}Ge_x$ variband solid solutions in the structures intended for the IR solar radiation conversion must be provided with a p–n junction at a certain depth (d) selected so as to ensure the maximum conversion efficiency. Figure 1b shows an equilibrium energy diagram of such an (n)Si–$(n)Si_{1-x}Ge_x$–$(p)Si_{1-x}Ge_x$ variband heterostructure. In this system, the longwave photosensitivity boundary of the heterostructure shifts toward the IR range.

Experimental data on the photosensitivity boundary wavelength λ for various solid solution compositions and the corresponding E_g values calculated using the relationship $E_g = 1.241/\lambda$ (eV) are summarized in the table. As seen from these data, the epitaxial films of $Si_{1-x}Ge_x$ variband solid solutions exhibit photosensitivity in the wavelength range from 1.15 to 1.6 μm. Therefore the (n)Si–$(n)Si_{1-x}Ge_x$–$(p)Si_{1-x}Ge_x$ heterostructures can be employed in narrow-bandgap elements of the cascade solar cells converting the IR solar radiation. Under certain conditions characteristic of the avalanche photodiode structures, these variband heterostructures can be also successfully employed in photodetectors for the wavelength range from 1.3 to 1.5 μm [7].
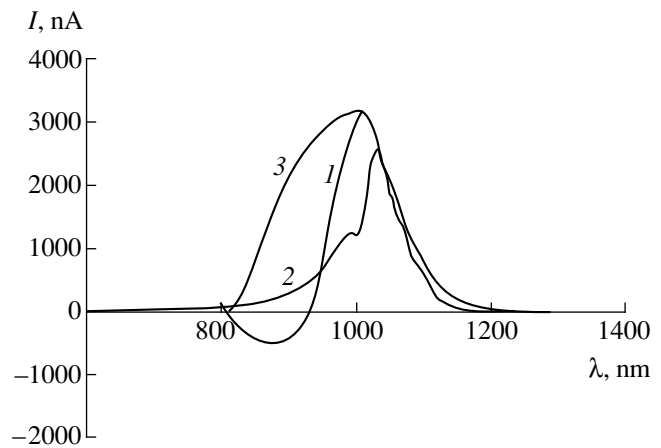

Fig. 4. Typical spectral characteristics of the photoresponse of Si–$Si_{1-x}Ge_x$ heterostructure grown on silicon substrates from (*1*, *2*) gallium- and (*3*) tin-based melts. The samples grown from gallium melts were measured (*1*) before and (*2*) after thermal treatment.

The quality of a p–n junction is evaluated by its I–U characteristic. Figures 5a and 5b show the forward and reverse dark I–U characteristics, respectively, for the Si–$Si_{1-x}Ge_x$ heterostructures grown from both gallium- and tin-based melts. An analysis of these curves indicates that, as expected, the heterojunction contains recombination centers accounting for the charge leak through the junction. It is also evident that the I–U characteristics of the LPE heterostructures grown from the gallium melt (curves *1* in Figs. 5a and 5b) are better than those of the samples grown from the tin melt (curves *2* in Figs. 5a and 5b). However, even the former structures are characterized by rather significant leak currents, especially pronounced in the forward mode.

In order to study the effect of thermal treatment on the I–U characteristics of the heterostructures studied, the samples were annealed for 20–30 min at 650–700°C in a flow of pure hydrogen. Subsequent measurements of the I–V curves showed improved characteristics (curves *1'* and *2'* in Figs. 5a and 5b). This result is explained by disappearance of the recombination

Experimental data on the longwave photosensitivity boundary λ for $Si_{1-x}Ge_x$ variband solid solutions with different compositions

No.	x in $Si_{1-x}Ge_x$	λ, μm	E_g, eV
1	0.05	1.15	1.07
2	0.10	1.25	1.01
3	0.20	1.28	0.97
4	0.35	1.38	0.90
5	0.50	1.47	0.84
6	0.70	1.54	0.81
7	0.90	1.60	0.77

The Effect of Scaling Factors on the Pinch-Induced Transition from a High-Velocity Sliding Contact to the Arc Mode

É. M. Drobyshevskiĭ

Ioffe Physicotechnical Institute, Russian Academy of Sciences, St. Petersburg, 194021 Russia
Received June 19, 2000

Abstract—Dependence of the velocity of a compact projectile slider accelerated in a railtron, reached by the moment of a transition of the high-velocity sliding contact to the high-current arc mode, on the system parameters and the acceleration regime is determined within the framework of a model assuming the magnetohydrodynamic (pinching) instabilities as the main factor responsible for this transition. It is established that the maximum transition velocity is proportional to the system gauge, specific conductivity, and strength of the slider material and is inversely proportional to the average slider density. © 2001 MAIK "Nauka/Interperiodica".

Introduction. When a solid slider is accelerated in a railtron system, the initial stage of a rather stable operation of the sliding metal–metal contact is followed by the arc formation between the rail and slider surfaces. As a result, the dusty plasma is ejected from the contact gap into the duct to initiate shorting arcs both in front of and behind the slider [1, 2]. As a result, the solid slider operates in a hybrid regime and the acceleration process passes within a few microseconds into a low- efficiency arc mode. This transition is unambiguously indicated by a sharp increase in the voltage drop measured at the duct output ($\Delta U_m \geq 30$–60 V).

Monitoring and analysis of the above phenomena, together with the study of the surface layers of rails and sliders upon acceleration and stopping, led us to the conclusion that the main factors responsible for the contact transition to the arc mode are the magnetohydrodynamic (MHD) instabilities of the pinch type developed in the contact zone [1, 2], rather than some two-dimensional processes of the velocity skin effect (VSE) type [3, 4]. This discovery allowed us to explain the well-known empirical rule according to which no contact transition to the arc mode takes place provided that the slider is pressed against the rails at a load exceeding a "one gram per ampere" level [5]. Under these conditions, a magnetic field pressure at the contact gap during the slider acceleration within a nearly standard regime does not exceed the slider pressure on the rails and the slider material strength, so that no pinching can take place in the contact zone. Determining the key role of the MHD phenomena at the contact interface revealed the inadequacy of the boundary conditions conventionally formulated assuming the ideal contact between slider and rails.

Within the framework of the VSE model [3, 4], the main parameter characterizing the contact transition to the arc mode during the slider acceleration is the critical velocity V_c at which the fusion wave arising at the back edge of the slider contact surface (where the skinned electric current concentrates) reaches the front edge of the contact zone. For a preset linear current density in the 2D approximation, the V_c value is a function of only the electric and thermodynamic (ETD) parameters of the rail and slider materials [3, 4].

However, in a real 3D experiment it is necessary to take into account, at least, the possibility of the current protruding forward by the side faces of both rail and slider. This implies dependence of the VSE manifestations on the system geometry, in particular, on the system gauge. An attempt at the theoretical analysis of the effect of scaling factors on the V_c value based on the experimental data was undertaken by James [6, 7]. Performed within the framework of the VSE model, this analysis showed that, in the general case, V_c must decrease with increasing system gauge.

It should be noted that the problem of the acceleration process scaling in a railtron, considered as a generalized electromechanical system, has been repeatedly studied, for example, in [8, 9]. An analysis of the general equations showed that a K-fold change in the system gauge, provided conservation of the current shape and a linear dependence of the current strength on K, the time scale increases as K^2 and the accelerator length and the accelerated body mass—as K^3. The sliding velocity grows in proportion to K, the acceleration is proportional to K^{-1}, whereas the output kinetic energy of the projectile device is proportional to $\propto K^5$.

Below we will attempt to elucidate, based on the new physical model of the slider–rail contact transition to the arc mode, how the resultant transition velocity V_c depends on the system gauge and other typical acceleration regime parameters. This will make possible a targeted search for the conditions ensuring the maximum possible V_c value, for the optimum accelerator design, and for the arcless system operation regime.

Main assumptions. In order to follow the major trends, we will ultimately simplify the problem making the following assumptions.

(i) We consider a monolithic slider (cube, cylinder, etc.) with a mass obeying the relationship $m = \rho_a d_0^3$, where d_0 is the railtron gauge (m) and ρ_a is the average slider density (below we use $\rho_a = 2700$ kg/m^3).

(ii) We assume that the sliding contact transition to the arc mode is due to a pinching constriction of the slider by the magnetic field pressure p_B in the zone of the slider–rail contact. In this zone, the material strength is decreased by the lack of shear resistance, whereby the transition onset corresponds to

$$p_B = B^2/2\mu_0 > s_y, \qquad (1)$$

where $\mu_0 = 4\pi \times 10^{-7}$ H/m is the permeability of the vacuum and s_y is the ultimate strength of the slider material (for Al-based alloys, $s_y = 400$ MPa). Since the magnetic field strength B depends on the current I as $B \approx \mu_0 I/2\pi r$, the pressure p_B at $I = $ const increases with decreasing pinch constriction radius r ($r \leq d_0/2$). Under condition (1), this leads to a collapse of the constricted region, followed by a thermal explosion and the appearance of an electric arc.

(iii) We assume that the skin layer thickness on the side faces of the slider increase with time t as $l = (t/\mu_0\sigma)^{1/2}$, where σ is the specific conductivity of the slider material (for Al, $\sigma \approx 10^7$ S/m).

(iv) We consider the case when the current passing through the slider is constant ($I = $ const).

(v) We assume that the main current flows in the substance under the skin layer, since the σ value within this layer drops with increasing temperature in the course of Joule's heating. This assumption is corroborated by more rigorous calculations performed for an analogous situation considered previously (see Figs. 1a and 2a in [10]).

(vi) We believe that the material strength within the heated skin layer is significantly lower than the strength of the cold material body.

(vii) We assume that the slider, accelerated by the force $F = L'I^2/2$ during the time t, acquires the velocity

$$V = \frac{L'I^2}{2d_0^3\rho_a}t, \qquad (2)$$

where L' is the linear inductance of the rails (typically, $L' \approx 0.3$ μH/m).

We will neglect a certain decrease in the slider mass related to a loss of the low-strength material caused by the TED effects [10]. Finally, we assume that the initial force pressing the slider to the rails is considerably lower than the ultimate strength of the slider material.

The critical velocity of the transition to the arc mode as a function of the acceleration regime. Taking into account the above assumptions (v) and (vi), we conclude that the effective constriction radius is $r \approx (d_0/2) - l$ and the pinching onset condition (1) in the region of slider–rail contact can be written as

$$\frac{B^2}{2\mu_0} = \frac{\mu_0 I^2}{2\pi^2(d_0 - 2l)^2}$$
$$= \frac{\mu_0}{2\pi^2}\frac{I^2}{d_0^2}\left[1 - \frac{2}{d_0}\left(\frac{t}{\mu_0\sigma}\right)^{1/2}\right]^{-2} \geq s_y. \qquad (3)$$

Excluding the current I from Eqs. (2) and (3), we obtain the following expression for a critical velocity corresponding to the contact pinching:

$$V(t) = \pi^2 \frac{L's_y}{\mu_0\rho_a}\frac{t}{d_0}\left[1 - \frac{2}{d_0}\left(\frac{t}{\mu_0\sigma}\right)^{1/2}\right]^2. \qquad (4)$$

Depending on the acceleration regime and the characteristics of the slider (more precisely, of the entire projectile structure), including the values of I, ρ_a, etc., the contact crisis onset may take place at any velocity given by formula (4). The maximum value of $V(t) = V_c$ is reached when the term in the square brackets equals $1/2$, that is, when $t = \tau_0/4 = \mu_0\sigma d_0^2/16$. In this case,

$$V_c = \gamma L'\sigma s_y d_0/\rho_a, \qquad (5)$$

where γ ($\pi^2/256$ for the above assumptions) is the normalization factor. Thus, the critical transition velocity for a compact slider is proportional to the system gauge. With the numerical values indicated above for an aluminum slider, we obtain $V_c = 68.5d_0$ km/s. In order to reach this velocity, it is necessary to maintain (over a time period $\tau_0/4$) the current at

$$I = \pi d_0(s_y/2\mu_0)^{1/2}, \qquad (6)$$

which corresponds to the transverse linear current density $I/d_0 \approx 40$ MA/m. This result implies that the scaling relationships are consistent with the aforementioned general scaling laws for electromechanical systems.

Discussion and conclusions. It is obvious that the obtained relationship between V_c, the slider characteristics, and the overall system parameters is a rough approximation, which can be employed only for estimating the character of the influence of various factors on the acceleration process. More precise particular relationships can be obtained by refining the assumptions and making allowance for some additional factors.

Nevertheless, we can already draw the following obvious conclusions.

First, the critical velocity has proved to depend on the properties of the slider material. In this respect, the combined parameter $\sigma s_y/\rho_a$ is the best for beryllium- and aluminum-based alloys. Thus, the variants selected

previously using a purely empirical approach [11] seem to exhaust the real possibilities.

Second, it is obvious that some of the above assumptions are very rough. For example, the presence of a payload would increase the average projectile density in formula (5). It should also be recalled that we ignored the TED effects.

Some other factors, such as the appearance of a melt on the contact gap or the initial force f acting upon the slider due to the rail pressure, were not taken into account. In principle, the latter additional pressure can be introduced into the resulting equations by replacing s_y with $s_y + (f/d_0^2)$ (recall the rule of "1 gram-force per ampere").

Finally, it is clear that the local features and the rate of the magnetic field penetration into the slider body significantly depend on the slider design and the rail–slider contact geometry. These features, as well as the inavoidable VSE manifestations, can be taken into account by carrying out the 3D numerical calculations. From these considerations, it is obvious that a description of the operation of C-shaped sliders with terminal contacts pressed against the rails by the magnetic field pressure would require a more detailed analysis. Therefore it is by no means surprising that some experiments using C-shaped sliders gave significantly greater V_c values as compared to the estimates predicted by formula (5). In particular, we managed to reach a value of $V_c = 1.33$ km/s for the C-shaped slider, which is the maximum value reported for the systems with $d_0 = 10$ mm. Price and Yum [12] reported on $V_c = 2.2$km/s for a $d_0 = 25$ mm gauge. The latter value is apparently the maximum velocity reached in systems with an arbitrary gauge.

A comparison of the two V_c values generally confirms the above conclusion concerning the proportionality of the transition velocity to the system gauge. It turns out that V_c is a secondary quantity depending on a number of other factors (really controlling the system operation), rather than a parameter determining the transition moment and character. Another conclusion,

also following from a comparison of the critical velocity value given by formula (5) ($V_c \approx 70d_0$ km/s) to the above values achieved in the experiments with C-shaped sliders, is that the effective value of s_y (or γ) in Eq. (5) must be greater by a factor of about two (indeed, the slider pressing onto the rails provided by any means, including the magnetic forces, can hardly exceed the material strength s_y). These considerations lead us to expect that considerably higher transition velocities can be achieved in systems of significantly greater gauge.

REFERENCES

1. É. M. Drobyshevskiĭ, B. G. Zhukov, R. O. Kurakin, *et al.*, Pis'ma Zh. Tekh. Fiz. **25** (6), 89 (1999) [Tech. Phys. Lett. **25**, 245 (1999)].

2. E. M. Drobyshevski, R. O. Kurakin, S. I. Rozov, *et al.*, J. Phys. D **32** (22), 2910 (1999).

3. P. B. Parks, J. Appl. Phys. **67** (7), 3511 (1990).

4. L. C. Woods, IEEE Trans. Magn. **33** (1), 152 (1997).

5. R. A. Marshall, IEEE Trans. Magn. **33** (1), 125 (1997).

6. T. E. James and D. C. James, IEEE Trans. Magn. **33** (1), 86 (1997).

7. T. E. James, IEEE Trans. Magn. **35** (1), 403 (1999).

8. K. T. Hsieh and B. K. Kim, IEEE Trans. Magn. **33** (1), 240 (1997).

9. H. D. Yun, IEEE Trans. Magn. **35** (1), 484 (1999).

10. É. M. Drobyshevskiĭ, É. N. Kolesnikova, and V. S. Yuferev, Pis'ma Zh. Tekh. Fiz. **25** (7), 25 (1999) [Tech. Phys. Lett. **25**, 260 (1999)].

11. D. Kirkpatrick and D. Haugh, IEEE Trans. Magn. **33** (1), 109 (1997).

12. J. H. Price and H. D. Yum, IEEE Trans. Magn. **31** (1), 219 (1995).

Translated by P. Pozdeev

Exoelectron Emission and Critical Phenomena in CuCl Crystals

N. A. Zakharov, T. V. Zakharova, V. A. Klyuev, and V. V. Gorbachev

Institute of General and Inorganic Chemistry, Russian Academy of Sciences, Moscow, Russia
Received May 18, 2000; in final form, November 2, 2000

Abstract—The temperature dependence of thermostimulated exoelectron emission (TSEE) and the specific heat c_p of CuCl single crystals were studied in a broad temperature range. It is suggested that the TSEE peaks observed in the region of 375 and 420°C are due to the polytype formation and the structural transition from a sphalerite to wurtzite polymorph; the peak at 170°C is assigned to Cu^{2+} ions present in the CuCl crystals studied. © 2001 MAIK "Nauka/Interperiodica".

Below we report on the results of investigation of the thermostimulated exoelectron emission (TSEE) of CuCl single crystals in a temperature range from 20 to 500°C. The interest in this study was related primarily to the fact that a relatively small difference between the sphalerite–wurtzite structural transition temperature ($T_{1'}$) and the melting temperature ($T_{2'}$) of CuCl (407 and 422°C, respectively [1]) creates considerable difficulties in obtaining high-quality single crystals of this compound [2]. At the same time, information about the crystal structure stability in CuCl is also of importance for both fundamental and applied research.

The experiments were performed on the samples of CuCl single crystals grown by the Bridgman and Kiropulos techniques, which contained no impurities of foreign elements [2]. According to the room-temperature X-ray diffraction data, the CuCl crystal samples possessed a cubic structure of sphalerite ($F\bar{4}3m$) with a unit cell parameter $a = 5.416$ Å. To within the error of the X-ray diffraction measurements, no foreign phases were detected in the samples studied. The TSEE measurements were performed as described elsewhere [3]. Thermoanalytical measurements in the differential thermal analysis (DTA) mode were carried out on a DSK-2M differential scanning calorimeter using crushed CuCl samples with a particle size of about $1 \times 1 \times 1$ mm.

The TSEE curve for CuCl single crystals (Fig. 1b) exhibits a clearly pronounced peak at $T_1 = 170$°C and two more intense closely spaced peaks at $T_2 = 375$ and $T_{1'} = 410$°C. The latter peak can be related to the structural transition from a sphalerite to wurtzite polymorph in CuCl, which is confirmed by the thermoanalytical data (Fig. 1a). Indeed, the alternating exo- and endothermal features observed in the c_p curve of a CuCl single crystal measured in the heating mode show evidence of two sequential processes. The endothermicity

at $T_{2'} = 422$°C corresponds to the melting temperature of CuCl, while the $T_{1'}$ value agrees with the data reported by other researchers [1, 4]. Then, the endothermal process at $T_{1'} = 410$°C is apparently due to the transition from a sphalerite to wurtzite polymorph, which is also reflected by a TSEE peak at the same temperature.

The TSEE peak at $T_1 = 170$°C (unlike that at $T_{1'} = 410$°C) is not accompanied by thermal effects and has a different nature. By analogy with the crystals of some well-known chalcogenides [5], the TSEE feature in the 170–180°C temperature interval can be related to the bulk Auger effect. The presence of this effect in the samples studied can be explained by the presence of a small amount of Cu^{2+} ions in the CuCl single crystals. The capture of electrons by traps according to the reaction $Cu^{2+} + \bar{e} \longrightarrow Cu^{1+}$ takes place in the course of the preliminary initiation of CuCl samples in the corona discharge field. A weak intensity of the peak at $T_1 = 170$°C in comparison with the other signals can be explained both by the relatively small content of Cu^{2+} ions in the samples and by a lower probability of electron emission from these centers [6].

In order to explain the TSEE peak observed at $T_2 = 375$°C (that is, at a temperature below that of the transition from the sphalerite to wurtzite polymorph), we may suggest the following versions.

First, in the region of temperatures close to $T_{1'}$ where the CuCl crystal structure is rather labile, there is certain probability of alternation in the ball packing mode. The appearance of local inclusions of a hexagonal ($F6_3mc$) wurtzite phase with the closest packing ABABAB… normal to [0001] (different from ABCABCABC… normal to [111] in the cubic $F\bar{4}3m$ structure of sphalerite) agrees with the experimental optical data [1].
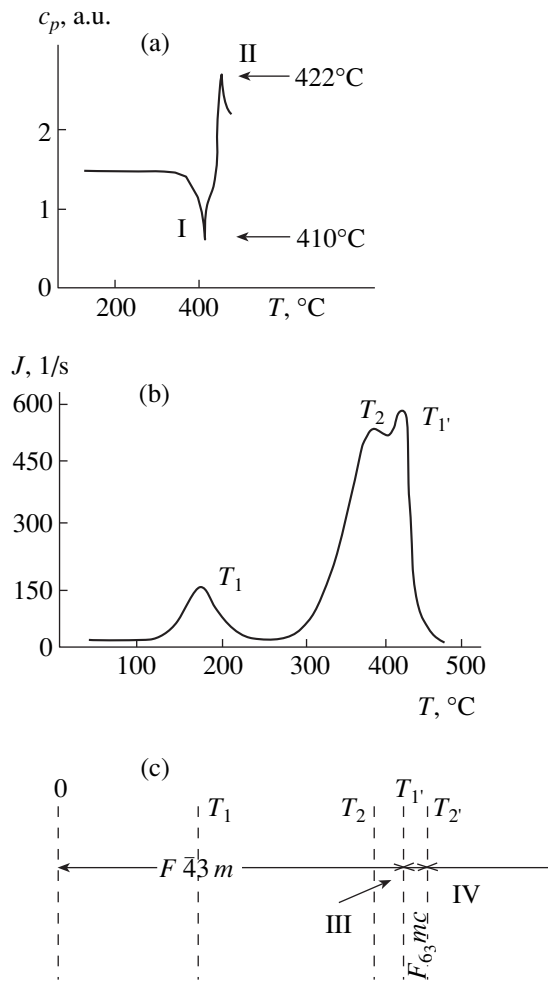
Fig. 1. Temperature dependence of (a) the heat capacity c_p in the region of (I) exo- and (II) endothermal effects and (b) thermostimulated exoelectron emission from CuCl single crystals of different symmetry (c): III, region of polytype formation; IV, melt.

Second, it is not excluded that heating of the CuCl sample may be accompanied by the formation of an intermediate polytype (for example—6H, 8H, 10H, 9R, 12R, etc. [7]) between sphalerite (3C) and wurtzite (2H), by analogy with the effect known in structurally close ZnS crystals [8, 9].

The final judgments on the features of critical phenomena observed in the temperature region of the transition from the sphalerite to wurtzite polymorph in CuCl can be made only after additional investigation. However, the results reported above can already be used in selecting the optimum conditions for the growth of high-quality CuCl single crystals and the operation of devices based on these crystals.

REFERENCES

1. M. Perner, J. Cryst. Growth **6**, 86 (1969).

2. K. V. Shalimova, T. V. Boroshneva, and G. F. Dobrzhanskiĭ, in *Proceedings of the 6th International Conference on Crystal Growth, Moscow, 1980,* Vol. 4, p. 279.

3. N. A. Zakharov, V. A. Klyuev, Yu. P. Toporov, *et al.,* Neorg. Mater. **31** (8), 1100 (1995).

4. M. Perner and J. Jindra, in *Crystal Growth* (Nauka, Moscow, 1967), Vol. 7, pp. 307–314.

5. H. Kaambre, in *Proceedings of the 4th Symposium on Exoelectron Emission and Dosimetry, Liblice, 1973,* p. 57.

6. E. I. Tolpygo, K. B. Tolpygo, and M. K. Sheĭnkman, Fiz. Tverd. Tela (Leningrad) **7** (6), 1790 (1965) [Sov. Phys. Solid State **7**, 1442 (1965)].

7. M. P. Shaskol'skaya, *Crystallography* (Nauka, Moscow, 1976).

8. N. K. Morozova and V. A. Kuznetsov, *Zinc Sulfide: Synthesis and Optical Properties* (Nauka, Moscow,1976).

9. N. G. Parsonage and L. A. Stavely, *Disorder in Crystals* (Oxford Univ. Press, Oxford, 1979; Mir, Moscow, 1982), Vol. 1.

Translated by P. Pozdeev

On the Relationship between the Optical Transmission and Photoluminescence Characteristics of Porous Silicon

A. A. Saren, S. N. Kuznetsov, V. B. Pikulev, Yu. E. Gardin, and V. A. Gurtov

Petrozavodsk State University, Petrozavodsk, Karelia, Russia
e-mail: saren@mainpgu.karelia.ru
Received October 27, 2000

Abstract—The characteristics of free-standing porous silicon (por-Si) films were studied using their optical transmission, photoluminescence (PL), and photoluminescence excitation spectra. The transmission spectra exhibit no features within the emission bands or near PL excitation thresholds, which is evidence that nonluminescent por-Si fragments play a dominating role in the process of light absorption. This fact indicates that the optical transmission spectra cannot be used as a source of information on the bandgap energy of charge carriers in luminescent silicon nanocrystallites. The required energy spectrum parameters can be roughly evaluated using the PL excitation spectrum. © *2001 MAIK "Nauka/Interperiodica".*

Experimental data on the optical transmission of porous silicon (por-Si) films are still used both to justify the quantum-sized model explaining the visible photoluminescence (PL) of por-Si [1] and to argue against this model. In some papers, the position of the optical transmission offset in por-Si is directly related to the bandgap width of the luminescent nanocrystallites [2–4]. The experiments demonstrated a shortwave shift of the transmission spectra of por-Si with increasing porosity of the material, which was interpreted as indicative of an increase in the bandgap width with decreasing dimensions of the por-Si nanocrystallites. At the same time, there is evidence [5] that the optical transmission offset in por-Si films may significantly shift even in the absence of changes in their PL spectra, which contradicts the above concept.

The purpose of this paper is to demonstrate, on the one hand, that the optical transmission (absorption) spectra of por-Si films are noninformative and, on the other hand, that important information for elucidating the radiative recombination mechanisms in these films is provided by the spectra of PL excitation.

We have studied the free-standing films of por-Si obtained by anodic etching of (100)-oriented *p*-type single crystal silicon wafers with a resistivity of 1 Ω cm. The etching electrolyte was a 49% hydrofluoric acid solution in isopropyl alcohol (1 : 1, v/v). The *p*-Si wafers were etched for 5 min at a constant current density of 25 mA/cm² under illumination from a halogen lamp. The films were lifted off in a diluted electrolyte solution, by passing a short (~5 s) pulse of electric current with a strength ten times that used for anodic etching. The separated films had a thickness of ~10 μm at a porosity of ~70%. The free-standing films were transferred onto the surface of polished magnesium fluoride plates. The transfer procedure necessarily involved turning the film over, so that the initial front side of the film was in contact with the plate. The plate material was highly transparent in the wavelength range studied, which allowed the PL to be excited and measured on both sides of the por-Si films.

The PL spectra were excited within a narrow energy range of the UV quanta (~4 eV) at a power density of ~1 mW/cm². The PL spectrum intensity was corrected for the spectrometer response. The PL excitation (PLE) spectra were measured using an original laboratory setup described elsewhere [6]. The induced luminescence signal was measured by a nonselective optical detector in a 600–850 nm wavelength band. The absorption spectra were determined by measuring the transmission coefficient using a Specord M-400 double-beam spectrophotometer (Germany) with a pure magnesium fluoride plate (not carrying a por-Si film) in the reference beam.

Figure 1 shows the normalized PL spectrum of a por-Si film recorded prior to separating the film from the Si wafer and the spectra measured on both sides of the same film in the free standing state. As can be seen, the PL spectrum of the por-Si layer on the original substrate almost coincides with that measured on the front side of the separated film, which indicates that the optical properties of the object are not affected by the separation procedure. The PL spectrum of the back side is shifted toward longer wavelengths, which is due to in-depth inhomogeneity of the luminescent properties of the por-Si layer. Within the framework of the quantum-sized por-Si model [1], this shift is explained by the in-depth porosity gradient: the characteristic size of the silicon crystallites increases from the front to the back side of the por-Si film.

Figure 2 shows the PLE spectra measured on the front and back sides of a separated por-Si film. As can

be seen, the spectra exhibit a well pronounced initial region where the signal intensity grows linearly with the excitation photon energy. Assuming that this dependence holds in the low-energy range (out of the scope of our experiment), we may extrapolate the linear portion to a zero signal and determine a threshold energy E_{th} of the photoexcitation process. The values obtained by this method were $E_{th} = 2.0 \pm 0.05$ eV for the front and $E_{th} = 1.9 \pm 0.05$ eV for the back side of por-Si films.

Figure 3 presents a plot of the optical density logarithm ln$A$ (proportional to the absorption coefficient α) of por-Si versus the photon energy and the corresponding linear approximation of this plot by the least squares method. A high accuracy of this linear approximation allows us to conclude that $\alpha(h\nu)$ is described by an exponent in the quantum energy range studied, which agrees with the data reported in [7]. For comparison, Fig. 3 also shows the PL spectra and indicates the PLE threshold energies E_{th} for both sides of the por-S film. It should be noted that the absorption spectrum exhibits no features in the vicinity of the PLE threshold and varies rather slightly within the PL bandwidth. Is is also interesting to note that the PL band of an amorphous hydrogenated silicon (a-Si:H) also falls within the energy range of the exponential $\alpha(h\nu)$ spectrum [8].

Now let us discuss the experimental data obtained. By definition, the PLE spectrum intensity is proportional to $\alpha(h\nu)$ and to $\eta(h\nu)$, the quantum yield of PL. Apparently, the relatively weak energy dependence of the absorbance (Fig. 3) cannot account for the sharp growth of the PL signal intensity in the PLE spectrum (Fig. 2). However, the quantum confinement theory of por-Si [9] predicts no significant variation of $\eta(h\nu)$ in this energy range either. In order to resolve the apparent discrepancy, it is reasonable to suggest that por-Si contains two components—luminescent and nonluminescent. The latter component, having a markedly greater relative volume, accounts for the optical absorption spectrum of por-Si. As noted above, the long exponential absorption "tail" is also characteristic of a-Si:H. The pattern of electron diffraction in por-Si shows the presence of an intensive diffuse halo due to an amorphized phase [10]. A high concentration of hydride bonds Si–H$_n$ in effectively luminescent por-Si is also confirmed by the IR spectroscopy data [11]. On the whole, all these facts allow us to suggest that a-Si:H is most probably the main component of por-Si, which determines the optical absorption—but not the luminescent properties of this material.

We relate the por-Si fragments capable of luminescence to nanosized silicon crystallites incorporated into the amorphous por-Si matrix. Absorption of the excitation light quanta in these nanocrystallites gives rise to the PL response registered in the PLE spectra. What information is provided by the PLE threshold energy E_{th}? Evidently, this characteristic acquires unambiguous interpretation assuming that $\eta(h\nu) = const$ and $d\alpha_{eff} \ll 1$, where d is the film thickness and α_{eff} is the
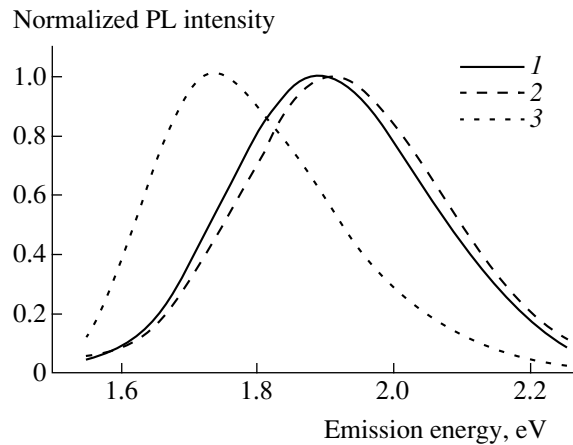

Fig. 1. PL spectra of (*1*) a por-Si layer on the original silicon substrate and (*2, 3*) the free-standing por-Si film separated from the substrate, measured from the (*2*) front and (*3*) back side.
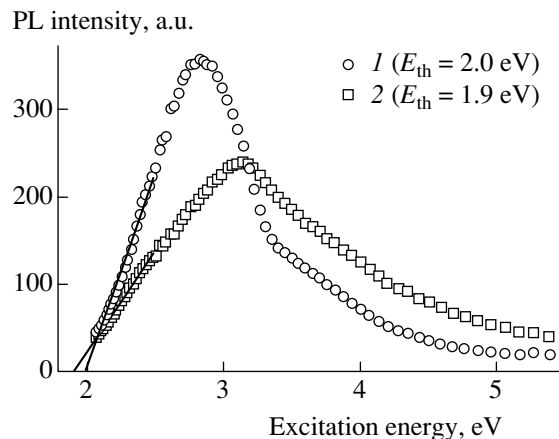

Fig. 2. PLE spectra measured on the (*1*) front and (*2*) back sides of a free-standing por-Si film. Solid curves show the linear least-squares approximations of the initial portions. The threshold excitation energies E_{th} are determined at intersections of the extrapolated linear portions with the abscissa axis.

effective absorption coefficient. Under these conditions, E_{th} represents the threshold energy for the electron–hole pair production, that is, the optical bandgap width of Si nanocrystallites. In our case, $d\alpha_{eff} \sim 1$ in the region of $h\nu \sim 2$ eV. This implies that the experimental E_{th} value determined from the PLE spectra provides a rough estimate of the bandgap width and also explains the fact that the E_{th} values obtained by extrapolation are significantly greater than the lowest emission energy observed in the PL spectra (see Fig. 3).

In conclusion, the comprehensive investigation of the luminescence properties (PL and PLE spectra) and optical absorption of free-standing films showed that the absorption spectra do not provide the unique characterization of nano-sized crystallites in porous silicon. Approximate characteristics of the energy band struc-
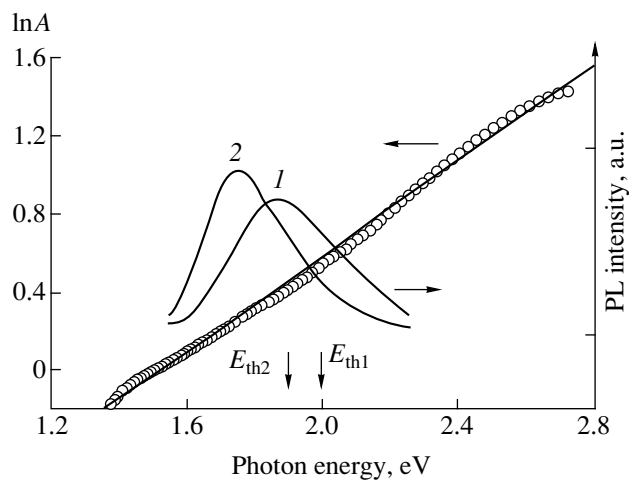
Fig. 3. The plot of natural logarithm of the optical density ln$A$ versus photon energy (circles) of a por-Si film and its linear approximation by least squares (solid line). Curves *1* and *2* show the PL spectra of the front and back sides of a free-standing film. Arrows indicate the threshold excitation energies E_{th} determined from the photoexcitation spectra.

ture of luminescent silicon nanocrystallites can be determined from the photoluminescence excitation measurements.

REFERENCES

1. L. T. Canham, Appl. Phys. Lett. **57**, 1046 (1990).

2. I. Sagnez, A. Halimaoui, *et al.*, Appl. Phys. Lett. **62**, 1155 (1993).

3. V. Grivickas and P. Basmaji, Thin Solid Films **235**, 234 (1993).

4. M. H. Chan, S. K. So, and K. W. Cheak, J. Appl. Phys. **79**, 3273 (1996).

5. Y. Kanemitsu, H. Uto, *et al.*, Phys. Rev. B **48**, 2827 (1993).

6. V. B. Pikulev, S. N. Kuznetsov, *et al.*, J. Porous Mater. **7**, 253 (2000).

7. Y. H. Xie, M. S. Hybersten, *et al.*, Phys. Rev. B **49**, 5386 (1994).

8. R. A. Street, Philos. Mag. B **37**, 35 (1978).

9. C. Delerue, G. Allan, and M. Lannoo, Phys. Rev. B **48**, 11024 (1993).

10. A. Nakajima, Y. Ohshima, *et al.*, Appl. Phys. Lett. **62**, 2631 (1993).

11. A. Borghesi, A. Sassella, *et al.*, Solid State Commun. **87**, 1 (1993).

Translated by P. Pozdeev

The Magnetic Sensitivity of Planar Triacs Increased by Radiation-Induced Structure Modification

S. G. Novikov, S. B. Baklanov, N. T. Gurin, and S. I. Vorontsov

Ul'yanovsk State University, Ul'yanovsk, Russia
e-mail: nsg@sv.uven.ru
Received November 10, 2000

Abstract—It is suggested and demonstrated that the magnetic sensitivity of planar triacs can be increased by the surface structure modification achieved by irradiating the devices with α- and β-particles. The results of investigation of the samples of low-power optocouplers based on the structure-modified triacs show evidence of a significantly (tenfold) increased magnetic sensitivity. © *2001 MAIK "Nauka/Interperiodica".*

In the past decade, considerable attention has been devoted by researchers to the study of radiation effects in solids [1, 2]. Very interesting effects are related to the radiation-induced modification of semiconductor structures and devices [3]. A very promising direction in this research is the study of new and modified properties of irradiated semiconductor devices. An example is offered by the magnetic sensitivity of multilayer semiconductor structures with negative differential resistance.

Well-known devices, such as thyristors and triacs, showing S-shaped current–voltage (I–U) characteristics and involving several p–n junctions, possess unique properties and can be used in various fields of electronics. Owing to a threshold operation mode and high sensitivity with respect to optical radiation, the electric field, and galvanic control, these devices are widely used as transducers, key switches, etc. However, ordinary commercial thyristors and triacs are characterized by very low or zero sensitivity with respect to the magnetic field, which hinders their use as reliable magnetic switches, magnetic field sensors, magnetic-field-controlled memory elements, etc. Several special types of thyristors possessing rated magnetic sensitivity have been developed, but even these devices possess a rather low magnetic sensitivity. An additional disadvantage of these thyristors is their complicated fabrication technology, which is related to the need to create additional elements to provide for the increased magnetic sensitivity [4]. At the same time, no data on the magnetic sensitivity of devices with symmetric S-shaped I–U characteristics were reported. Therefore, the task of creating effective magnetically sensitive triacs for their operation in ac circuits is still urgent.

We suggest increasing the magnetic sensitivity of planar triacs by modifying their surface structure with the aid of bombardment by α- and β-particles. To solve this task, we have studied the magnetic sensitivity of two triac-based optocouplers as a function of the irradiation dose. The planar-diffusion triacs (PDTs) in the optocouplers studied were based on the integrated moduli composed of two coplanar thyristor structures representing back-to-back connected hybrid threshold switches of the 2U106 type housed in a common semiconductor volume [5, 6]. Prior to irradiation, the samples were tested for the magnetic sensitivity with and without optical control. Sample 1 gave no response to the applied magnetic field up to $B = 1.4$ T, while sample 2 showed very weak magnetic sensitivity (the field-induced switching voltage variation did not exceed 5 V/T).

The samples were irradiated using a ^{244}Cm source emitting α-particles with the energies 5.76 and 5.8 MeV and an intensity of 23×10^{10} Bq. The β-radiation was obtained from an ^{90}Sr + ^{90}Y source of the BIS-50 type producing a flux of β-particles (2π) with an intensity of 1.37×10^{10} s^{-1}.

During the experiment, we monitored the main parameters of the triac optocouplers (switch-on voltage and current, keep-back current, residual voltage) depending on the irradiation dose and the applied magnetic field strength. The external magnetic field was oriented along the p–n junction so that the Lorentz force would deviate the charge carriers toward the plate surface.

Sample 1 was exposed to α-particles during 3.25 h, which corresponded to a total fluence of $\Phi = 10^{10}$ cm^{-2}. This treatment gave rise to a magnetic sensitivity, whereby the switch-on and keep-back currents and the switch-on voltage U_{so} (at a control gate current of $I_g = 20$ mA) were linear functions of the magnetic field strength (Fig. 1).

Sample 2 was irradiated with β-particles (electrons). The treatment consisted of three exposures so as to study variation of the magnetic sensitivity with the increasing fluence. The exposure durations were $t = 1$, 4, and 23.3 h, which corresponded to the irradiation
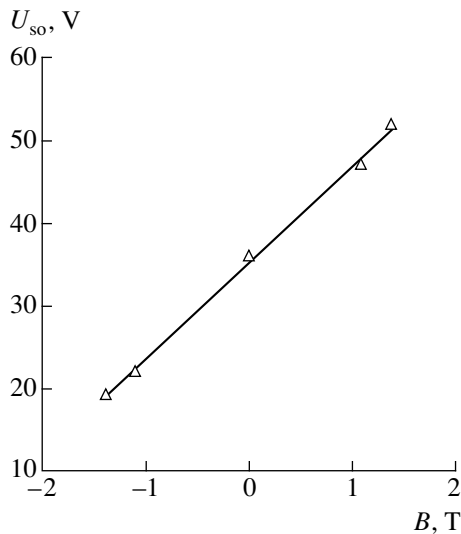
U_{so}, V

Fig. 1. The plot of triac switch-on voltage versus applied magnetic field strength for PDT sample 1 ($I_g = 20$ mA).
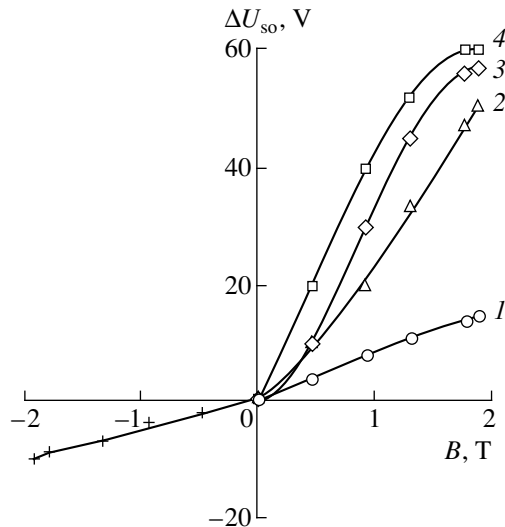

Fig. 2. The plots of a change in the triac switch-on voltage versus applied magnetic field strength for PDT sample 2 ($I_g = 10$ mA) β-irradiated for $t = 0$ (*1*), 1 (*2*), 4 (*3*), and 23.3 h (*4*).

doses of $D = 4.1 \times 10^{12}$, 1.7×10^{13}, and 10^{14} cm^{-2}, respectively. It was found that the sensitivity of sample 2 to the magnetic field gradually increased with the irradiation dose (Fig. 2).

The results of our experiments showed that the α and β radiation increases the magnetic sensitivity of PDTs from 0 to 11 V/T (sample 1) and from 5 to 39 V/T

(sample 2), respectively (Fig. 2). The higher magnetic sensitivity of the PDT irradiated with β-particles is due to a greater fluence: this treatment allows a higher density of surface defects to be obtained without changing the bulk electric parameters. The investigation also showed evidence of a high radiation stability of the static parameters of triacs involved in the optocouplers studied: the irradiation with 4-MeV α-particles to a fluence of $\Phi = 3 \times 10^{11}$ cm^{-2} did not change the main device characteristics. In contrast, irradiation of a silicon bipolar transistor with 2.8-MeV α-particles to a lower fluence of 1.5×10^{11} cm^{-2} decreased the transistor gain to one-tenth of the initial value.

A preliminary analysis of the radiation-induced magnetic sensitivity in PDTs showed that the main factors responsible for the triac sensitization effect are the defects related to the radiation-induced atomic displacements (for the α-irradiation) and the ionization events (for the β-irradiation) in the near-surface base region (within a 3-μm-thick layer). These defects significantly increase the rate of the surface recombination of charge carriers driven to the surface by the Lorentz force. Taking into account the recombination component of the base current in the equations for *I–U* characteristics of PDTs, it is possible to describe dependence of their main triac parameters on the applied magnetic field strength.

Thus, we have proposed a method for increasing the magnetic sensitivity of planar-diffusion triacs by irradiating the devices with α- and β-particles and have studied the mechanism of this effect and the radiation stability of triacs on optocouplers. Using triacs with the radiation-stimulated magnetic sensitivity, it is possible to create various types of magnetic key switches, ac and dc transducers, storage devices, etc.

REFERENCES

1. A. Chilingarov and T. Sloan, Nucl. Instrum. Methods Phys. Res. A **399**, 3537 (1997).
2. E. Simonen, J. Vanhellemont, J. P. Dubuc, *et al.*, Appl. Phys. Lett. **68**, 788 (1996).
3. Tomii Kazushi, Maeda Mitsuhide, Keno Takuji, *et al.*, Trans. Inst. Electr. Eng. Jpn., Part D **115**, 806 (1995).
4. I. M. Vikulin, L. F. Vikulina, and V. I. Stafeev, *Galvanomagnetic Devices* (Radio i Svyaz', Moscow, 1983), p. 104.
5. S. B. Baklanov, N. T. Gurin, and S. G. Novikov, Izv. Vyssh. Uchebn. Zaved., Élektron. **6**, 49 (1997).
6. S. B. Baklanov, V. V. Gaĭtan, N. T. Gurin, *et al.*, Élektron. Prom–st **1**, 51 (1992).

Translated by P. Pozdeev

Effect of Oxygen on the Chemical Reactions and Electron Work Function in Ba–Si and BaO–Si Structures

V. V. Il'chenko and G. V. Kuznetsov

Kiev State University, Kiev, Ukraine
Received November 2, 2000

Abstract—Effects of the annealing in oxygen on the chemical composition and electron work function of Ba–Si and BaO–Si structures were studied. Thin Ba or BaO layers deposited onto silicon stimulate oxidation processes on the semiconductor surface. Treatment of the Ba–Si and BaO–Si samples at temperatures $T_s \geq 500°C$ leads to the formation of a barium orthosilicate (Ba_2SiO_4) layer. A decrease in the electron work function observed for the silicon surface coated with both barium oxide and barium silicate layers provides for a more than tenfold increase in the electron emission current. © 2001 MAIK "Nauka/Interperiodica".

Investigation of the Ba–Si system is of interest because barium and its compounds are promising materials for the field emission cathodes [1, 2], ohmic contacts [3], buffer layers, and MIS structures [4]. The possibility of using these structures under a relatively low vacuum or in the atmosphere is determined to a considerable extent by chemical interactions of the sample surface with the ambient gaseous medium, in particular, with oxygen. For the silicon field emission cathodes, an increase in the electron emission current and the stability of cathode operation can be achieved by coating the silicon surface with thin barium oxide films. Therefore, it is necessary to study the influence of atmospheric oxygen on the process of barium-containing film formation and the electron emission properties of barium-coated silicon cathodes.

In this work, we studied the effect of oxygen on the chemical interactions and electron work function in Ba–Si and BaO–Si structures. Thin films of barium or barium oxide were deposited onto a Si(100) surface in vacuum (at a residual pressure $p = 10^{-4}$ Pa) from a tungsten evaporator. Preliminarily, the evaporation process was stabilized for 1–2 h. After deposition, the Ba–Si and BaO–Si structures were annealed at temperatures up to 800°C both in vacuum and in an oxygen atmosphere. The surface composition was monitored by X-ray photoelectron spectroscopy (XPS). The XPS measurements were performed on a Hewlett-Packard Model 5950A spectrometer. The analytical lines were Si2p (binding energy, 99.1 eV), Ba4$d_{3/2}$ (92.6 eV), and Ba4$d_{5/2}$ (89.9 eV) [5]. The sample surface structure was studied by tunneling microscopy (AFM mode).

Figure 1a shows the XPS data illustrating the effect of annealing in oxygen on the energy position of the ground Si2p level for the pure silicon surface (curve *1*) and the surface coated with thin barium layers with a thickness of $d_{Ba} = 3$ nm (curve *2*) and 10 nm (curve *3*). The samples were treated in an oxygen atmosphere

($p_{O_2} = 10^5$ Pa) for 5 min at $T_s = 500°C$. The XPS spectrum of a pure silicon surface exhibits an additional, very small broad maximum in the region of binding energies above that of the main Si2p level. This plateau is characteristic of a shift of the ground Si2p level related to the presence of various oxidation states (Si^{1+}, Si^{2+}, Si^{3+}, Si^{4+}) [5]. The thermal oxidation of silicon usually takes place at a markedly higher temperatures ($T_s \geq 700°C$); the annealing at lower temperatures only leads to the formation of thin nonstoichiometric oxides SiO_x ($x < 2$). Deposition of a thin Ba layer leads to a sig-
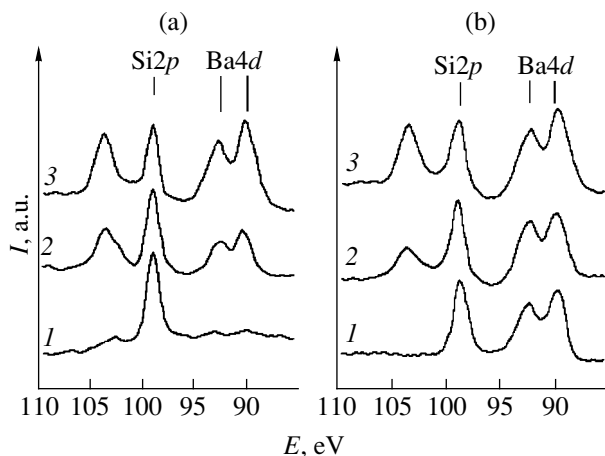

Fig. 1. X-ray photoelectron spectra of the ground levels of silicon (Si2p) and barium (Ba4d) measured for pure silicon, barium-coated (Ba–Si), and barium-oxide-coated (BaO–Si) surfaces annealed for 5 min at $T_s = 500°C$ in oxygen ($p_{O_2} = 10^5$ Pa) or in vacuum. (a) Effect of barium coating: the spectra of (*1*) pure silicon, (*2*) Ba–Si ($d_{Ba} = 3$ nm, oxygen), (*3*) Ba–Si ($d_{Ba} = 10$ nm, oxygen); (b) effect of oxygen: the spectra of (*1*) Ba–Si ($d_{Ba} = 10$ nm, vacuum), (*2*) BaO–Si ($d_{BaO} = 10$ nm, vacuum), and (*3*) BaO–Si ($d_{BaO} = 10$ nm, oxygen).
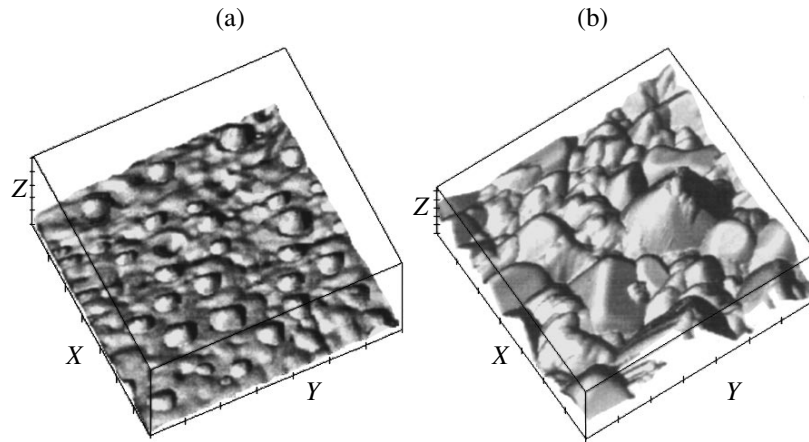
(a)   (b)

Fig. 2. AFM images showing morphology of the surface of a BaO–Si structure upon annealing for 30 min in oxygen at $T_s = 500$ (a) and 750°C (b). Scale: $X = Y = Z = 100$ nm.

nificant intensification of the process of silicon oxidation, as evidenced by an increase in height of the shifted Si2p peak (Fig. 1a, curves *2* and *3*). As the oxygen concentration increases, this Si2p level shifts closer to the position characteristic of Si^{4+} in SiO$_2$ and eventually stabilizes at 103.2 eV for an oxygen pressure above 10^2 Pa. An increase in the Ba layer thickness is accompanied by the growth in the ratio of Si2p peak intensities corresponding to SiO$_2$ and pure Si (Fig. 1a, curves *2* and *3*). This behavior is indicative of the increasing oxygen penetration, which stimulated further growth of the silicon oxide (SiO$_2$) layer.

Using the XPS spectra presented in Fig. 1b, we may compare the effects of oxygen upon chemical interactions in the structures with Ba and BaO layers. Here, the thickness of Ba (curve *1*) and BaO (curves *2* and *3*) layers was the same (10 nm). The samples were treated for 5 min at $T_s = 500$°C in a vacuum (curves *1* and *2*) or in oxygen (curve *3*). The spectrum of the Ba–Si structure (curve *1*) shows a small shift in positions of the ground levels for both Ba4d (increase) and Si2p (decrease) binding energies relative to the values for pure elements, which is evidence of the chemical interaction between Ba and Si atoms. In contrast to the Ba–Si system, the BaO–Si sample annealed in a vacuum at $T_s = 500$°C shows the oxidation-induced shift of the Si2p level toward higher binding energies (Fig. 1b, curve *2*). Silicon is an effective reducing agent for barium oxide and a certain amount of oxygen passes to silicon, although barium has a greater oxygen affinity. In the BaO–Si sample annealed in an oxygen atmosphere, a rapid chemisorption of oxygen leads to intensive silicon oxide formation (Fig. 1b, curve *3*). Similarly to the Ba–Si structures (Fig. 1a), the degree of silicon surface oxidation increases with the BaO layer thickness and the oxygen concentration.

The above results allow us to explain the process of Ba–Si and BaO–Si structure formation in the presence of oxygen, assuming that an electron exchange mechanism is operative between deposited atoms and the silicon substrate. In the initial stage, the electron charge transfer from Ba to Si atoms leads to their ionic binding, which is typical of the behavior of alkali atoms adsorbed on silicon [2]. This charge transfer accounts for a certain weakening of the strong covalent Si–Si bonds, whereby silicon atoms become more active in reacting with oxygen. For a sufficiently thick barium coating, the covalent Si–Si bonds in the near-surface layer of the silicon substrate are completely broken and Si atoms diffuse to the outer film surface to allow continuing oxidation. As the annealing temperature grows, the energy structure of Si2p peaks in the XPS spectrum varies: the binding energy of the Si2p level is lower as compared to that in SiO$_2$, which is probably evidence of the silicate phase formation [5].

The annealing in oxygen at $T_s \geq 500$°C leads to active chemical interaction between BaO and SiO$_2$ oxides. In the presence of broken coordination Si–Si bonds, the silicon substrate surface features the formation of a metal-rich orthosilicate phase of the Ba$_2$SiO$_4$ type, in which silicon atoms are surrounded by both oxygen and barium atoms [4]. In comparison with the other silicate phases, the growing orthosilicate layer is characterized by minimum internal stresses developed at the substrate boundary.

Figure 2 shows AFM images of the surface of a 100-nm-thick BaO coating on the silicon substrate, obtained upon annealing the samples for 30 min in oxygen at $T_s = 500$ and 750°C. The sample annealed at 500°C exhibits a smooth surface of the amorphous deposit, with pyramidal islands formed at the crystallization centers on this background (Fig. 2a). As the annealing temperature increases, the linear dimensions of the crystallites increase and the silicate layer formed acquires a polycrystalline structure. Upon the annealing at $T_s = 750$°C, the sample surface exhibits closely

Electron work function of silicon with and without Ba and BaO coatings annealed in oxygen

Structure	Si	Ba–Si	BaO–Si	
Annealing temperature T_s, °C	500	500	500	750
Work function φ, eV	4.8–5.0	2.8–3.0	2.9–3.1	3.1–3.3

spaced crystallites with dimensions up to several tens of nanometers (Fig. 2b).

A change in the electron work function of a silicon substrate coated with thin Ba or BaO layers and annealed in oxygen was studied by the method of contact potential difference. In the measuring scheme, the average work function value for the tungsten cathode was taken equal to $\varphi_W = 4.5$ eV [2] and silicon samples were used as replaceable anodes. The difference between the work functions φ_A of two anodes with identical geometries was determined by a shift of the current–voltage characteristic $e\Delta V = \varphi_{A1} - \varphi_{A2}$. Data on the electron work function of silicon samples with and without Ba and BaO coatings determined upon anneal-

ing in oxygen ($t = 30$ min; $p_{O_2} = 10^5$ Pa; $d_{Ba} = d_{BaO} = 10$ nm) are presented in the table.

Investigation of the field electron emission characteristics of the sample structures showed that a decrease in the electron work function provides for a more than tenfold increase in the electron emission current for the surface of silicon coated with barium oxide or barium silicate layers.

REFERENCES

1. C. Spindt, C. Holland, A. Rosengreen, and I. Brodie, IEEE Trans. Electron Devices **38** (10), 2355 (1991).
2. B. P. Nikonov, *Oxide-coated Cathode* (Moscow, 1979).
3. M. T. Usmanov, I. Z. Dzhumanov, A. K. Tashatov, and B. E. Umirzakov, in *Proceedings of the XIII International Conference on Interaction of Ions with Surface, Moscow, 1997*, Vol. 2, p. 311.
4. I. V. Belousov, V. V. Ilchenko, G. V. Kuznetsov, *et al.*, IEEE Trans. Appl. Supercond. **5** (2), 1510 (1995).
5. V. I. Nefedov, *X-ray Photoelectron Spectroscopy of Chemical Compounds: A Handbook* (Moscow, 1984).

Translated by P. Pozdeev

Microwave-Band Reflection Coefficient of High-Temperature Superconductor Specimens in *E*-Plane Waveguide Structures

A. I. Gubin, A. A. Lavrinovich, and N. T. Cherpak

Usikov Institute of Radiophysics and Electronics, National Academy of Sciences of Ukraine, Kharkov, Ukraine

Received November 13, 2000

Abstract—The microwave-band reflectivity of high-temperature superconductor (HTSC) specimens was measured for the first time in the *E*-plane waveguide structures of two types: tapered waveguide termination and *E*-plane corner section. The measured reflection coefficient of a textured $YBa_2Cu_3O_{7-\delta}$ specimen used as a tapered waveguide termination corresponds well to the theoretical curve calculated using an improved two-fluid HTSC model. © *2001 MAIK "Nauka/Interperiodica".*

The microwave-band impedance of various superconductors, including high-temperature ones (HTSCs), is studied using different approaches. Most of these apply various types of resonance structures; however, a nonresonance technique is also known. This technique is based on measuring the microwave power penetrating through a HTSC film [1]. However, when the film is placed in the cross section of a waveguide, the transmitted power can only be measured for very thin specimens [2]. In the case of HTSCs, the thickness of these specimens must be of an order of 10 nm. It seems that, for thicker films, the surface impedance Z_s (or the surface admittance σ) of the specimen can be obtained by measuring the reflection coefficient $\Gamma = |\Gamma|e^{i\psi}$. However, for a thick HTSC plate oriented perpendicularly to the longitudinal axis of the waveguide (Fig. 1a), amplitude $|\Gamma|$ of this coefficient is close to unity for all conductors [3] and changes only slightly even when σ varies over a wide range [4]. A similar result is obtained for the normally incident plane electromagnetic wave. As a result, the transition of the HTSC specimen from a normal to superconducting state affects only slightly the temperature behavior of the reflection coefficient Γ.

Recent experiments have shown that, in the infrared frequency band, the situation can be improved by using a *p*-polarized beam incident onto the specimen at a grazing angle [4].

Although, at lower frequencies, the reflection coefficient becomes less sensitive to variations in the σ level, it is expected that the effect of increased sensitivity must also be observed in the microwave range. Waveguide eigenmodes, including the fundamental H_{10} mode of the rectangular waveguide, are not plane waves; however, they can be represented as a sum of plane waves. Hence, the effect of increased sensitivity at grazing angles of incidence onto the plane surface of

a HTSC specimen must be observed in the waveguide as well.

The inclination of the specimen was implemented in two waveguide structures: a waveguide corner section (Fig. 1b) and a waveguide section with tapered termination (Fig. 1c). In both cases, *E*-plane structures were used. In the first structure (unlike the second one), the incident and reflected waves are decoupled from each other. The waves traveling in the *E*-plane waveguide structures simulate the case of a *p*-polarized plane wave incident to the specimen at an arbitrary angle.
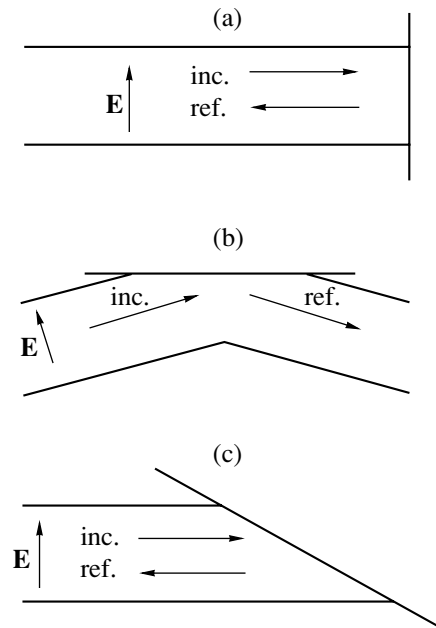

Fig. 1. Waveguide sections used in the measurements: (a) shorting plane placed perpendicularly to the longitudinal axis of the waveguide, (b) waveguide corner, and (c) tapered termination.

The experiments were performed with a 5.2 × 2.6-mm waveguide. The reflectivity $|\Gamma|^2$ and the phase ψ of the reflection coefficient of a textured $YBa_2Cu_3O_{7-\delta}$ specimen were measured in the Q wave (6 mm) band in a temperature range from 77 to 300 K with the help of a microwave phase bridge. The measurements were performed for two angles of the specimen orientation $\theta = 0°$ and $80°$ (for both waveguide sections, the angle was measured between the direction of the incident waveguide mode and the normal to the specimen surface).

The measured temperature dependence of $|\Gamma|^2$ is shown in Fig. 2. One can see that the sensitivity of $|\Gamma|$ to changes in the specimen conductance increases by a factor of approximately 10 for the tapered termination and by a factor of 7 for the corner section. The measurements were performed at 45 GHz. In the case of the tapered termination, this factor varies nonmonotonically in the waveguide passband. This may be caused, apparently, by the influence of instrumental factors. In this passband, the range of the reflection coefficient may change approximately 1.5 times. It seems that this nonmonotonic behavior can be removed by increasing isolation of the incident and reflected waves (e.g., with the help of a circulator).

Figure 2 presents both the measured temperature dependence of $|\Gamma|$ and theoretical curves calculated for a HTSC material used as a terminating load at $\Theta = 0°$ and $80°$. No calculations were performed for the waveguide corner because of the complexity of the electrodynamic analysis of such a waveguide structure.

The calculations were based on an improved two-fluid model describing the microwave-band features of a HTSC material, which takes into account the field penetration depth λ_L and the residual surface resistance [5]. The fitting parameters ($\sigma_N = 6 \times 10^4$ $(\Omega \text{ m})^{-1}$, $\lambda_L = 10^{-6}$ m, $\gamma = 1.7$, and $\alpha = 4.0$; see [5] for the notations) agree well with the known data. Measurements of the phase and amplitude of the reflection coefficient can be used to determine the behavior of the complex permit-
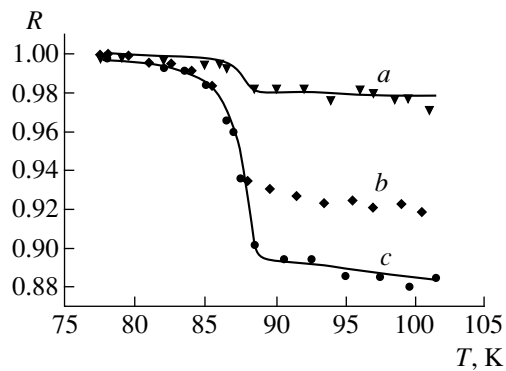

Fig. 2. Experimental (points) and theoretical (solid curves) temperature dependencies of the reflection coefficient of the HTSC specimen for waveguide sections shown in Figs. 1a–1c (dotted and solid lines marked with *a*, *b*, and *c*, respectively).

tivity ε and/or the surface impedance Z_s as a function of external factors (temperature, magnetic field, microwave or optical pumping, etc.).

REFERENCES

1. A. P. Jenkins, K. S. Kale, and D. Dew-Hughes, Stud. High Temp. Supercond. **17**, 179 (1996).

2. P. H. Wu and Q. Min, J. Appl. Phys. **71**, 5550 (1992).

3. A. R. Von Hippel, *Dielectric and Waves* (Wiley, New York, 1954).

4. H. S. Somal, B. J. Feenstra, J. Schützmann, *et al.*, Phys. Rev. Lett. **76**, 1525 (1996).

5. O. G. Vendik, I. B. Vendik, and D. I. Kaparkov, IEEE Trans. Microwave Theory Tech. **46** (5), 469 (1998).

Translated by A. Kondrat'ev

The Fluctuational Electromagnetic Interaction of Moving Neutral Atoms with a Flat Surface: An Account of the Spatial Dispersion Effects

G. V. Dedkov and A. A. Kyasov

Kabardino-Balkarian State University, Nal'chik, Kabardino-Balkaria, Russia
Received September 20, 2000

Abstract—General formulas for the fluctuational electromagnetic forces acting upon a neutral atom moving with a nonrelativistic velocity parallel to a flat surface were derived using the mirror reflection image model and a fluctuational-dissipative interaction formalism developed previously. The obtained formulas take into account the spatial dispersion effects and coincide with the local approximation relationships in the absence of these effects. The results are applied to the calculation of the resonance forces of atomic retardation on the surface plasmons. © *2001 MAIK "Nauka/Interperiodica"*.

In the absence of the spatial dispersion effects, the most general expressions for both conservative and dissipative forces acting upon a neutral nonrelativistic particle moving parallel to a flat or cylindrical surface were derived previously [1–4]. In the presence of a nonlocal coupling between the induction and electric field strength, a spatial inhomogeneity of this problem (relative to the z coordinate perpendicular to the surface) leads to transformation of the Maxwell equations for the retarding Green's function of the photon in a medium. These equations transform into a complicated set of integrodifferential equations. However, an allowance of the spatial dispersion for a particle moving at a distance z_0 from the plane is only necessary when $z_0 \leq l$, where l is the surface plasmon wavelength. In practice, solving this task is very important for the interpretation of experiments related to the dynamic mode of an atomic force microscope and to the damping of motions in adsorbed films [5].

In this context, it would be interesting to apply the so-called mirror reflection image (MRI) model [6, 7], which was successfully used to obtain analytical formulas for the interaction of charged particles and dipole molecules with a surface [8–10]. In the absence of a spatial dispersion, these formulas coincided with the analogous expressions obtained by other researchers and with our results [1–4].

The MRI model for a particle with a charge Ze moving near a plane is illustrated in the figure. The main idea of this approach is to consider, in addition to the initial "real" particle moving from the vacuum toward the surface, a mirror reflection image of this particle and to introduce an effective surface charge density $\rho_s(x, y, t)\delta(z)$ necessary to satisfy the boundary conditions of continuity for the potential and the normal component of the electric induction on the surface $z = 0$ bounding the medium.

For a neutral nonrelativistic atom in the S-state moving parallel to the surface (considered as a fluctuating point dipole with all the necessary conditions [3, 4]), the MRI model equations for the Fourier components of the interaction potential can be written in the following form (cf. Eqs. (3), (4) for a charged particle in [9])

$$\Phi(\omega, \mathbf{k}) = \frac{4\pi}{k^2}\rho_s(\omega, \mathbf{q}) - \frac{8\pi i \mathbf{k}\mathbf{d}^{sp}(\omega - \mathbf{q}\mathbf{v})}{k^2}, \quad z < 0;$$
$$\Phi(\omega, \mathbf{k}) = -\frac{4\pi}{k^2}\frac{\rho_s(\omega, \mathbf{q})}{\varepsilon(\omega, \mathbf{k})}, \quad z > 0,$$

(1)

where $\mathbf{k} = (\mathbf{q}, k_z)$, $\mathbf{q}$ is a 2D wavevector in the plane
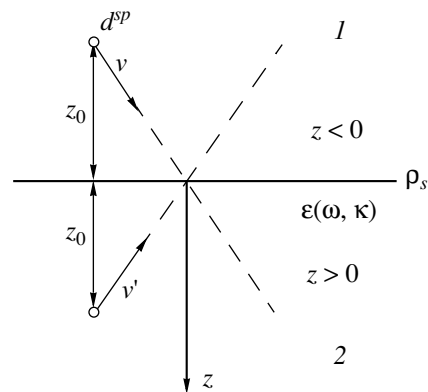
A schematic diagram illustrating reflection of a particle possessing a fluctuational dipole moment d^{sp} from a flat surface at $t = 0$ and showing its mirror image: (*1*) vacuum; (*2*) metal; ρ_s is the effective surface charge density introduced in the MRI model for calculating the induced potential in a vacuum.

$z = 0$, and $\mathbf{d}^{sp}$ is the fluctuating dipole moment vector of the atom, and $\varepsilon(\omega, \mathbf{k})$ is the dielectric function of the medium. Accomplishing the inverse Fourier transform from k_z to z in Eqs. (1), one can show that the derivative of the potential at $z = 0$ obtained using the first equation in (1) can be written in the following form:

$$\left. \frac{d\Phi(\omega, \mathbf{k}, z)}{dz} \right|_{z = 0}$$

$$= -2\pi\rho_s(\omega, \mathbf{q}) + 4 \int_{-\infty}^{+\infty} \frac{dk_z k_z^2 d_z^{sp}(\omega - \mathbf{qv})}{k_z^2 + q^2}. \quad (2)$$

A disadvantage of the MRI model is the obvious divergence of the integral in Eq. (2), which hinders a consistent analysis of the contribution to the interaction related to the spontaneous dipole moment components perpendicular to the surface. Note that, for a polar molecule possessing a constant z-projection of the dipole moment, this disadvantage of the MRI model was obviated in [9] using the results of calculations of the interaction potential for a point charge (in which case the MRI model is rigorous) and representing the dipole as a superposition of two charges. Unfortunately, this method is ineffective in the case of a fluctuating dipole moment.

No problems are encountered for the other dipole moment components (parallel to the interface). Then, taking $d_z^{sp} = 0$ and using the conditions of continuity for the potential and the z-projection of the electric induction on the surface $z = 0$, we obtain from Eqs. (1)

$$\rho_s(\omega, \mathbf{q}) = \frac{2\pi i}{\pi + qI_0} \mathbf{q}\mathbf{d}^{sp}(\omega - \mathbf{qv}), \quad (3)$$

where the quantity I_0 is given by the integral

$$I_0 = \int_{-\infty}^{+\infty} \frac{dk_z}{(k_z^2 + q^2)\varepsilon(\omega, \mathbf{k})}. \quad (4)$$

Substituting formula (3) into Eqs. (1) and subtracting the Fourier component of the intrinsic field potential of the fluctuating dipole, we obtain

$$\Phi^{in}(\omega, \mathbf{k}) = \frac{4\pi i}{k^2} \Delta_s(\omega, \mathbf{q}) \mathbf{q}\mathbf{d}^{sp}(\omega - \mathbf{qv}), \quad (5)$$

where $\Delta_s(\omega, \mathbf{q}) = \dfrac{\pi - qI_0}{\pi + qI_0}$. For the local dielectric fluctuations, this yields $\Delta_s(\omega, \mathbf{q}) = \Delta(\omega) = \dfrac{\varepsilon(\omega) - 1}{\varepsilon(\omega) + 1}$ in agreement with our previous results [1–4]. Using rela-

tionship (5), we may also derive an expression for the induced potential of a fluctuating dipole:

$$\Phi^{in}(x, y, z, t) = \frac{i}{(2\pi)^2} \iiint d^2\mathbf{q}\,d\omega \frac{\Delta_s(\omega, \mathbf{q})}{q}$$

$$\times \exp(-2q|z|)\mathbf{q}\mathbf{d}^{sp}(\omega - \mathbf{qv}). \quad (6)$$

The structure of formulas (5) and (6) differs from that of the expressions derived in [3, 4] only in that $\Delta(\omega)$ is replaced by $\Delta_s(\omega, \mathbf{q})$. Therefore, all subsequent calculations of a conservative potential for the attractive interaction between atom and surface and of the dissipative retardation forces are identical to those made in the absence of the spatial dispersion (see, e.g., the derivation of formulas (6), (13), and (21) in [4]), but the final formulas will differ from those obtained in [4] by an additional factor 1/2 reflecting the absence of a z-projection of the dipole moment of the particle studied. For example, a general expression for the lateral fluctuational force is as follows (double prime indicates imaginary components of the corresponding functions):

$$F(z_0, V) = \frac{\hbar}{\pi^2 V} \int d\omega \iint dk_x\, dk_y k$$

$$\times \exp(-2kz_0) \coth\left(\frac{\omega h}{2k_B T}\right) \{(\omega + k_x V)$$

$$\times [\Delta_s''(\omega, \mathbf{q})\alpha''(\omega + k_x V) - \Delta_s''(\omega + k_x V, \mathbf{q})\alpha''(\omega)] \quad (7)$$

$$+ (\omega - k_x V)[\Delta_s''(\omega, \mathbf{q})\alpha''(\omega - k_x V)$$

$$- \Delta_s''(\omega - k_x V, \mathbf{q})\alpha''(\omega)]\}.$$

Thus, we have certain grounds to believe that Eq. (7) adequately takes into consideration the spatial dispersion effects if taken with a coefficient of 2.

In order to assess the role of nonlocal effects in the retardation of atomic particles on the surface plasmons in simple metals, we will use an approximation for $\Delta_s''(\omega, \mathbf{q})$ in the following form [11]:

$$\Delta_s''(\omega, \mathbf{q}) = \frac{\pi\omega_s^2}{2\omega_s(q)} \delta(\omega - \omega_s(q)), \quad (8)$$

where $\omega_s^2(q) = \omega_s^2 + \alpha q + \beta q^2 + 0.25q^4$ is a dispersion equation for the surface plasmons; the parameters ω_s, α and β are tabulated as functions of the density parameter in the jelly model [11]. For example, aluminum is characterized by $\omega_s = 11.8$ eV, $\alpha = -0.6$ at.u. and $\beta = 2.066$ at.u.

For the atomic polarizability, an analogous (resonance) approximation yields

$$\alpha''(\omega) = \sum_n \frac{\pi e^2 f_{0n}}{2m\omega_{0n}} \delta(\omega - \omega_{0n}), \quad (9)$$

where f_{0n} and ω_{0n} are the oscillator strength and the transition frequency of the $0 \longrightarrow n$ transition. Substituting formulas (8) and (9) into Eq. (7), we obtain

$$
F = \frac{\hbar e^2 \omega_s^2}{mv} \sum_n f_{0n} \int_0^\infty \frac{q^2 dq}{\omega_s(q)} \exp(-2qz_0)
$$

$$
\times \frac{\omega_n - \omega_s(q)}{\sqrt{q^2 v^2 - (\omega_n - \omega_s(q))^2}} \theta\left(1 - \left|\frac{\omega_n - \omega_s(q)}{qv}\right|\right),
$$

(10)

where $\theta(x)$ is the Heaviside function. In the local approximation, with $\omega_s(q) = \omega_s$, relationship (10) leads to an expression obtained previously [3, 4]:

$$
F = -\frac{\hbar e^2 \omega_s}{2mv^4} \sum_n f_{0n}(\omega_s - \omega_n)^3
$$

$$
\times (K_0(2(|\omega_s - \omega_n|z_0/v) + K_2(2(|\omega_s - \omega_n|z_0/v)),
$$

(11)

where K_0 and K_2 are the Bessel functions. For $\omega_n > \omega_s$, Eq. (11) shows the possibility of the appearance of a positive (accelerating) lateral force, whereby the atom receives energy from the surface plasmon field. However, this point requires additional investigation to take into account the distribution of oscillator strengths and dispersion in more detail.

At the same time, it can be readily shown for $v \ll v_F$ (where v_F is the Fermi velocity) that the domain of integration over q in Eq. (11) at a fixed n reduces to a narrow interval with a width of $2\omega_n v/(\alpha + 2\beta k_0 + k_0^3)$, where k_0 is the root of equation $\omega_n = \omega_s(k_0)$ and the force F (still retarding) ceases to depend on the particle velocity. However, this result also should not be overstated because formulas (8) and (9) are valid only provided that the resonance peaks of α'' and Δ_s'' do not overlap. Since the integration over wavevectors in Eq. (11) encounters this very region, it appears that correct results can be probably obtained only using a more general Eq. (7).

REFERENCES

1. G. V. Dedkov and A. A. Kyasov, Pis'ma Zh. Tekh. Fiz. **25** (12), 11 (1999) [Tech. Phys. Lett. **25**, 466 (1999)].
2. G. V. Dedkov and A. A. Kyasov, Phys. Lett. A **259**, 38 (1999).
3. A. A. Kyasov and G. V. Dedkov, Surf. Sci. **463** (1), 11 (2000).
4. G. V. Dedkov and A. A. Kyasov, Fiz. Tverd. Tela (St. Petersburg) **43** (1) (2001) [Phys. Solid State **43**, 176 (2001)].
5. G. V. Dedkov, Usp. Fiz. Nauk **170** (6), 585 (2000).
6. R. H. Ritchie and A. L. Marusak, Surf. Sci. **4**, 234 (1966).
7. D. Wagner, Z. Naturforsch. A **21**, 634 (1966).
8. J. Heinrichs, Phys. Rev. B **8**, 1346 (1973).
9. R. Nunez, P. M. Echenique, and R. H. Ritchie, J. Phys. C **13**, 4229 (1980).
10. J. F. Annett and P. M. Echenique, Phys. Rev. B **36** (17), 8986 (1987).
11. J. F. Annett and P. M. Echenique, Phys. Rev. B **34** (10), 6853 (1986).

Translated by P. Pozdeev

Determination of the Impact Excitation Cross Section for Luminophor Activators Using Voltage–Luminance Characteristics of Thin-Film Electroluminescent Structures

M. K. Samokhvalov, R. R. Davydov, and É. I. Khadiullin

Ul'yanovsk State Technical University, Ul'yanovsk, Russia

Received November 10, 2000

Abstract—A new method is proposed for determining the parameters of emission centers in the luminophor layer of a ZnS-based thin-film electroluminescent display. The method was experimentally verified to yield correct values of the activator concentration and the impact excitation cross section. The results are compared to the data reported previously. © 2001 MAIK "Nauka/Interperiodica".

At present, electroluminescent (EL) thin-film structures are considered as promising elements for the creation of flat active displays. The development of effective and reliable display elements on this basis requires investigating the properties of EL structures and establishing relationships between the parameters of emitting centers, structural and technological factors, and special features of the EL excitation regimes in thin-film structures. The study of physical processes in thin EL films is also of interest from the standpoint of elucidating the mechanisms of charge carrier production and acceleration in strong electric fields and the interaction of carriers with the activated emission centers. In this context, we have developed a new method for determining the principal parameters of emission centers in luminophor films, which is based on the measurement of the voltage–luminance characteristics of EL structures for the harmonic excitation.

The main equation of electroluminescence, derived within the framework of the model of direct impact excitation of emission centers in a luminophor describes the kinetics of variation of the concentration N^* of excited emission centers [1]:

$$\frac{dN^*}{dt} = \frac{\sigma}{e} j(N - N^*) - \frac{N^*}{\tau}, \qquad (1)$$

where σ is the impact excitation cross section of the emission center, e is the electron charge, j is the current density in the luminescent film, N is the concentration of activated emission centers, and τ is the emission decay time constant. Using this equation in a steady-state regime, whereby the emission centers pass into the excited state, produce emission, and return to the initial state within a period of the excitation voltage

variation to ensure that

$$\int_0^T \frac{dN^*}{dt} dt = 0,$$

and taking into account the Talbot law (since the voltage frequency is many times the critical flashing rate ensuring a steady apparent luminance for the human eye)

$$B_1 = \frac{1}{T} \int_0^T B(t) dt,$$

we derive a relationship between the average luminance B_1 of a thin-film EL structure and the applied voltage parameters. This relationship, obtained within the framework of the model of direct impact excitation of emission centers in a luminophor, is as follows:

$$B_1 = \frac{\eta_0 B_0 fk(V - V_{th})}{B_0 + \eta_0 fk(V - V_{th})}, \qquad (2)$$

where V and f are the amplitude and frequency of the applied voltage; V_{th} is the threshold voltage; B_0 is the maximum luminance corresponding to the average luminance in the case when all activator centers pass from the excited to the ground state within the voltage variation period; and η_0 is the maximum light yield (a physical meaning of this quantity is the light yield under conditions that the active current passing through the film excites all activated emission centers and that the accelerated electrons do not interact with excited centers) [2, 3]. The coefficient $k = 4V_{th}CC_D C_L^{-1}$ is determined from an expression for the average power dissipated in the luminophor layer $P_1 = fk(V - V_{th})$, where C is the capacitance of the whole EL structure and C_D and C_L are the capacitances of the dielectric and luminophor layers, respectively [2, 3].
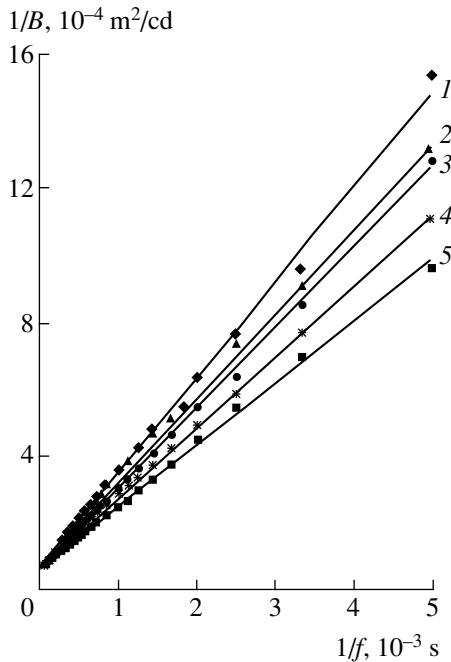
Fig. 1. The plots of inverse luminance $1/B$ versus inverse frequency $1/f$ for various excitation voltage amplitudes $V = 200$ (*1*), 207 (*2*), 214 (*3*), 221 (*4*), 228 V (*5*).

The luminance and light yield are essential characteristics of the emission sources. However, in the case of thin-film emitters, these quantities strongly depend on the conditions of measurement. This circumstance complicates a comparison of these characteristics for various thin-film EL structures. The proposed effective parameters B_0 and η_0 depend on the properties of the materials employed and the structural factors, while being independent of the excitation conditions. These quantities determine the maximum luminance and light yield of a luminophor film. We suggest using these characteristics for the comparison of various EL display elements and for calculating the regimes and devices controlling the operation of such displays.

Using simple transformations [2], Eq. (2) can be written in the following form:

$$\frac{1}{B_1} = \frac{1}{B_0} + \frac{1}{\eta_0 f k (V - V_{th})}. \tag{3}$$

According to this relationship, determination of the maximum luminance and light yield of a luminophor film can be based on the measurement of the voltage–luminance characteristics of the EL structure at various frequencies of the excitation voltage. By plotting the experimental data in the $1/B$ versus $1/f$ (or $1/B$ versus $1/(V - V_{th})$) coordinates, we can determine the B_0 and η_0 values by measuring the slopes of these linear plots and by extrapolating these plots to intersect with the ordinate axis.

The maximum luminance of an EL structure is determined by the luminophor properties and by parameters of the emitting element design:

$$B_0 = \eta_C d_L N \tau^{-1},$$

where η_C is the effective light yield determined by the optical constants of the material employed and d_L is the luminophor layer thickness.

The maximum light yield also depends on the luminophor properties:

$$\eta_0 = (\eta_C \sigma N)(\pi e E_{Lth})^{-1},$$

where E_{Lth} is a threshold value of the electric field strength in the luminophor. Thus, once the maximum luminance and light yield of a luminophor are determined, we may calculate the principal parameters of emission centers in the EL layer—the concentration of activators and their impact excitation cross section. The proposed method of analysis of the voltage–luminance characteristics is especially convenient for determining the impact excitation cross section, since all the other methods require either a complicated instrumentation for the kinetic investigations or additional measurements of the dissipated power [4, 5].

We have experimentally studied the properties of thin-film EL capacitors using multilayer metal–dielectric–luminophor–dielectric–transparent electrode systems prepared by vacuum deposition onto glass substrates. The luminophor layer represented a film of manganese-doped (0.5 at. %) zinc sulfide with a thickness of 0.5–2.5 μm. The dielectric layers were obtained by depositing solid solutions of zirconium and yttrium oxides with a thickness of 0.2–0.3 μm. The sample structures were characterized by measuring their voltage–luminance characteristics and the frequency dependences of integral luminance for the EL excited by a harmonic voltage.

Figures 1 and 2 show typical experimental plots of the luminance versus frequency and amplitude of the excitation voltage plotted in the $1/B$ versus $1/f$ and $1/B$ versus $1/(V - V_{th})$ coordinates, respectively. As seen from these data, the experimental plots are well approximated by straight lines intersecting at the origin. This indicates that the experimental results are consistent with the theoretical relationship (3) derived based on the model of direct impact excitation of the activated emission centers in a luminophor film.

Using the proposed method, based on the measurement of the voltage–luminance characteristics and the frequency dependences of integral luminance, we determined the maximum luminance $B_0 = (1.35 \pm 0.01) \times 10^4$ cd/m^2 and maximum light yield $\eta_0 = 4.76 \pm 0.05$ lm/W. These values agree with the data obtained by other methods and with the known characteristics. We have also estimated the parameters of manganese activated emission centers in a ZnS-based luminophor: the activator concentration was found to be $N = (1.25 \pm$

$0.12) \times 10^{18}$ cm^{-3} and the impact excitation cross section, $\sigma = (2.7 \pm 0.2) \times 10^{-15}$ cm^2.

Thus, the concentration of emission centers amounts to only a few percent of the total manganese content introduced during the luminophor preparation. This discrepancy is explained by the true activated saturation (TAS) effect, whereby a considerable proportion of manganese ions in the luminophor occupy positions in which they either exhibit a considerably lower emission efficiency or do not participate at all in the excitation and emission events. During deposition of a Mn-doped ZnS film, manganese ions may not only substitute for zinc ions, but accumulate in considerable amounts at the grain boundaries (and, probably, in the interstitials) as well, thus not participating in the formation of emission centers [6]. According to previous estimates, obtained based on the luminance and relaxation time data, the proportion of excited emission centers also did not exceed 10% of the total content of Mn^{2+} ions introduced into the luminophor [7].

The impact excitation cross section is a parameter characterizing the probability of interaction of accelerated electrons with the activated emission center, which is accompanied by the energy transfer and the activator passing into an excited state [1, 2]. The *ab initio* calculation of this parameter proceeding from theoretical estimates is difficult, since it is necessary to take into account the electron energy, the activator charge and position in the crystal lattice, and the influence of surrounding ions [3]. Experimental determination of the impact excitation cross section allows us to estimate and compare the probability characteristics of processes involved in the EL excitation in various luminophors. The estimate obtained above for the impact excitation cross section agrees with the data reported by other researchers. In particular, Gurin and Sabitov [8] obtained $\sigma = (2–4) \times 10^{-15}$ cm^2 from the measurements of luminance waves under conditions where the activator excitation rate markedly exceeds the rate of radiative recombination. Mach [9] presented the value $\sigma = 4 \times 10^{-16}$ cm^2, which was calculated from data on the excitation efficiency using some fitting parameters (including the mean free path of electrons). For a more rigorous evaluation of this physical parameter, it is necessary to perform additional investigations using various samples, variable excitation regimes, and alternative methods for the impact excitation cross section determination.

Thus, we have obtained relationships between the luminance and the amplitude and frequency of the harmonic excitation voltage within the framework of the model of direct impact excitation of emission centers in a luminophor. Using this relationship, we determined the principal parameters of thin-film EL emitters and
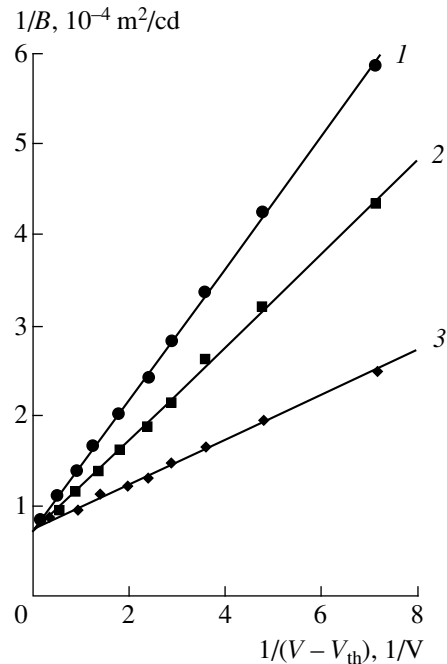

Fig. 2. The plots of inverse luminance $1/B$ versus inverse voltage amplitude $1/(V - V_{th})$ for various excitation voltage frequencies $f = 0.8$ (*1*), 1 (*2*), 1.6 kHz (*3*).

estimated the concentration and impact excitation cross section of the activated emission centers in an Mn-doped ZnS-based luminophor using the experimentally measured voltage–luminance characteristics.

REFERENCES

1. R. Mach and G. O. Muller, Phys. Status Solidi **81** (2), 609 (1984).
2. M. K. Samokhvalov, Zh. Tekh. Fiz. **66** (10), 139 (1996) [Tech. Phys. **41**, 1045 (1996)].
3. M. K. Samokhvalov, *Thin-Film Electroluminescent Radiation Sources* (Ul'yanovs. Gos. Tekh. Univ., Ul'yanovsk, 1999).
4. M. K. Samokhvalov, Zh. Prikl. Spektrosk. **62** (3), 182 (1995).
5. M. K. Samokhvalov, Pis'ma Zh. Tekh. Fiz. **21** (15), 78 (1995) [Tech. Phys. Lett. **21**, 621 (1995)].
6. G. O. Muller and R. Mach, J. Lumin. **40/41**, 92 (1988).
7. N. A. Vlasenko and S. N. Gur'yanov, Izv. Akad. Nauk SSSR, Ser. Fiz. **49** (10), 1909 (1985).
8. N. T. Gurin and O. Yu. Sabitov, in *Proceedings of the International Conference "Centers with Deep Levels in Semiconductors and Semiconductor Structures"* (Ul'yanovs. Gos. Univ., Ul'yanovsk, 1997), p. 122.
9. R. Mach, Springer Ser. Solid-State Sci. **57**, 186 (1985).

Translated by P. Pozdeev

The Spin-Wave Resonance Study
of Concentrational Inhomogeneities
in Nanocrystalline Ni–Fe–P and Ni–Fe–C Alloys

R. S. Iskhakov, D. E. Prokof'ev, L. A. Chekanova, and V. S. Zhigalov

Kirenskiĭ Institute of Physics, Siberian Division, Russian Academy of Sciences, Krasnoyarsk, Russia
Received December 4, 2000

Abstract—The films of nanocrystalline Fe–Ni alloys obtained by various methods in the permalloy composition range (~20 at. % Fe) were studied by the method of spin-wave resonance (SWR) spectroscopy. The effective SW exchange stiffness η^{eff} exhibits a characteristic dependence on the spin wavelength, which is indicative of the magnetization fluctuations in these films with a correlation radius of 12–20 nm. This is indirect evidence of the microphase separation in these nanocrystalline alloys and provides an estimate of the characteristic spatial size of an inhomogeneity in the atomic ratio $X_{\text{Fe}}/X_{\text{Ni}}$. © 2001 MAIK "Nauka/Interperiodica".

Introduction. As is known, nanocrystalline (NC) materials are essentially thermodynamically nonequilibrium systems characterized by a high level of internal stresses, a large concentration of defects, developed grain boundaries, and some other factors accounting for the increased thermodynamic potential ΔG [1, 2]. This leads to the formation of metastable phases in NC alloys [3, 4] and makes these alloys capable of structural transformations that are impossible in thermodynamically equilibrium states. These unusual processes include the dissociation of hydrides [5], the decomposition of thermodynamically stable intermetallic compounds [6], etc.

Another example of such structural transformations is offered by the microphase separation (concentrational inhomogeneity), which we observed in Ni–Fe alloys with compositions in the permalloy concentration range (~20 at. %). In the single- or polycrystalline state, these alloys are classified as disordered ideal (or regular) solid solutions with an fcc crystal lattice the sites of which are randomly occupied by Fe and Ni atoms. Previously, it was believed that the statistical fluctuations of the relative atomic content $X_{\text{Fe}}/X_{\text{Ni}}$ are small, with the fluctuation volume not exceeding more than 1 nm, which corresponds to the atomic and phase (chemical) homogeneity limits. However, our experiments showed that the nanocrystalline state stimulates a chemical inhomogeneity in these alloys, with the spatial scale exceeding 10 nm for fluctuations in the atomic ratio $X_{\text{Fe}}/X_{\text{Ni}}$.

Evidence for this concentrational inhomogeneity was obtained by spin-wave resonance (SWR). The idea was that a chemical or phase inhomogeneity in alloys based on the 3d transition metals (Fe, Co, Ni) is unavoidably manifested by fluctuations of the spin system parameters (exchange parameter α, magnetization M, magnitude and orientation of the local anisotropic magnetic field). These fluctuations can be detected by structurally sensitive magnetic methods such as SWR.

Sample preparation and experimental methods. The SWR spectra of thin-film samples of Ni–Fe–P and Ni–Fe–C alloys were measured at room temperature on a standard X-band spectrometer with a cavity pumping frequency of $f = 9.2$ GHz using standing spin waves with wavevectors in the range from 10^5 to 2×10^6 cm^{-1}. The film samples were placed into a region of the maximum amplitude of the ac magnetic field in the duplex cavity and magnetized perpendicularly to the film surface. In this geometry, the resonance field strengths corresponding to peaks in the SWR spectrum are known to obey the equation

$$H_n = \frac{\omega}{\gamma} + 4\pi M - \alpha M k_n^2, \qquad (1)$$

where ω is the frequency, γ is the gyromagnetic ratio, α is the exchange parameter (related to the exchange interaction constant A), M is the magnetization, and k_n is the wavevector of the nth SWR mode. The last quantity is determined by the formula $k_n = \pi n/d$, where $n = 1, 2, 3, \ldots$, and d is the film thickness.

The resonance field strengths determined in the SWR spectra were plotted in the coordinates $\delta H = H_1 - H_n$ versus n^2 (Fig 1), which allowed the experimental data to be compared to a theoretical dispersion curve $\omega(k^2)$ calculated for the spin waves. The $\omega(k^2)$ curve for an inhomogeneous ferromagnet was calculated in [7, 8], where it was demonstrated that the dispersion law is described by the equation

$$\omega(k) = \omega_0 + \alpha g M k^2 (1 - \gamma_i^2 J_i(k)). \qquad (2)$$

Here, ω_0/g is the internal field in the ferromagnet; $i = \alpha$ or M (fluctuating parameter); $\gamma_i = \Delta i / i$ is the intensity of the fluctuating parameter i; and $J_i(k)$ is a function set by fluctuations of the spin parameter (α, M). The shape of the function $J_i(k)$ determines the SW dispersion law corresponding to the fluctuations of a given spin parameter. In our case, it is important that the functions $J_\alpha(k)$ and $J_M(k)$ depend on the wavevector k in a significantly different manner in the region of $k_i^* = 1/r_i^*$ determined by the correlation radius r_i^*. Indeed, the values of $J_\alpha(k)$ in the vicinity of $k = k^*$ increase (from 1/3 to 5/4), whereas $J_M(k)$ first decreases from 1/2 to 0 and then (for $k = 2k^*$) increases from 0 to 5/4. Because of this difference in behavior of the $J_\alpha(k)$ and $J_M(k)$ functions at $k \sim k^*$, the experimentally determined values of the effective SW stiffness $\eta^{\text{eff}}(k)$ calculated by the formula

$$\eta^{\text{eff}}(k) = \left(\frac{d}{\pi}\right)^2 \frac{(H_1 - H_n)}{(n^2 - 1)} \qquad (3)$$

will also differ provided that the wavevector interval studied contains the k^* value. In the case of the SW exchange fluctuations, the η^{eff} values decrease in the vicinity of $k = k^*$; for the magnetization fluctuations, the η^{eff} values increase at $k = k^*$ and decrease at $k = 2k^*$. Such changes in the behavior of $\eta^{\text{eff}}(k)$ were previously detected by SWR in the films of amorphous ferromagnetic alloys [9–12].

The NC films of Ni–Fe–P alloys with various compositions ($X_{\text{Ni}} = 91\text{–}71$ at. %; $X_{\text{P}} = 2$ at. %) and thicknesses within ~150–200 nm were obtained by chemical vapor deposition (CVD) onto glass substrates [10]. The relative content of iron and nickel ($X_{\text{Fe}}/X_{\text{Ni}}$) was determined by X-ray emission spectroscopy, and the phosphorus concentration was determined by chemical analysis.

Using the X-ray diffraction techniques, the NC film samples were characterized by the symmetry (fcc), lattice constant ($a = 3.52\text{–}3.54$ Å), and the coherent scattering domain (CSD) size (20–26 nm). The effective magnetization determined by the ferromagnetic resonance (FMR) method was $M^{\text{eff}} = 530\text{–}660$ G; the exchange interaction constant determined from the SWR data was $A^{\text{eff}} = (0.4\text{–}0.7) \times 10^{-6}$ erg/cm. Note that the Ni–P (iron-free) NC alloy films exhibited an FMR spectrum with a very broad band. As the alloy was doped with iron, the band width gradually decreased and then (in films with $X_{\text{Fe}} = 8$ at. %) the spectrum showed an SWR signal containing up to 11 peaks (Fig. 2, I). An analysis of the SWR spectra showed that NC films of the Ni–Fe–P alloy system are described by the boundary conditions close to the ideal Kittel conditions (infinite pinning of the surface spins). As can be seen from Fig. 2 (I), intensities of the odd SWR peaks significantly (by more than two orders of magnitude) exceed those of the neighboring even peaks.
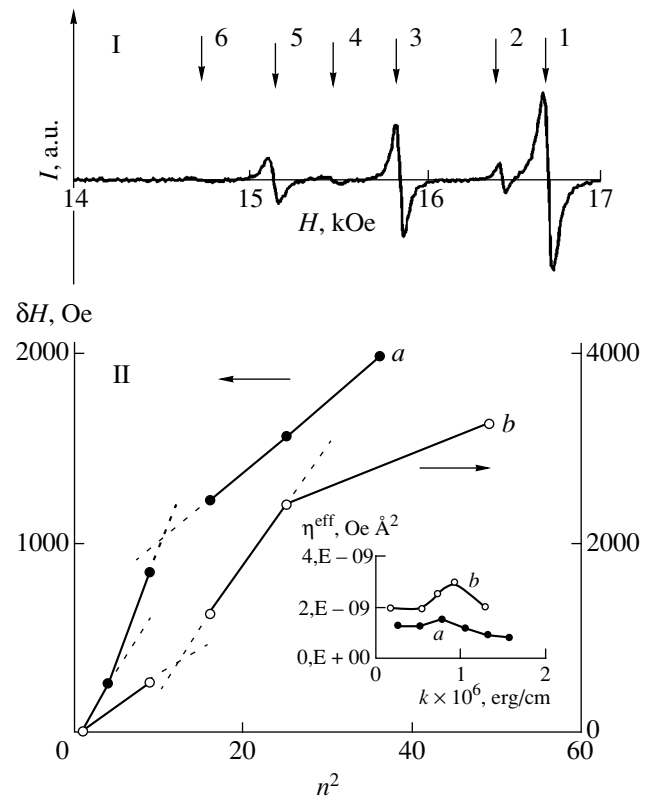

Fig. 1. SWR data for nanocrystalline Ni–Fe–C alloys: (I) a typical SWR spectrum of a film with the thickness $d = 120$ nm; (II) Experimental plots of the resonance field difference δH versus square mode number n^2 for the samples of (a) ($Ni_{65}Fe_{35}$)–C, $d = 120$ nm and (b) ($Ni_{80}Fe_{20}$)–C, $d = 170$ nm. The inset shows the plots of effective exchange stiffness η^{eff} versus wavevector for the same films.

The NC films of the Ni–Fe–C system with the compositions ($Ni_{80}Fe_{20}$)–C and ($Ni_{65}Fe_{35}$)–C ($X_{\text{C}} = 15$ at. %) and thicknesses ~120–170 nm were prepared by pulsed plasma deposition (PPD) in a vacuum [13] at a residual pressure of $P_0 = 5 \times 10^{-6}$ Torr. The PPD samples (as well as the CVD ones) were deposited onto glass substrates. The chemical composition of these films was determined using the Auger electron spectra measured on a Riber photoelectron spectrometer (these measurements were performed at the Institute of Semiconductor Physics, Siberian Division, Russian Academy of Sciences, Novosibirsk). Also determined in these measurements were the depth–concentration profiles of the films, showing the constant content of each element. However, the phase composition exhibited variation with depth [14], for which reason these films were characterized only by the FMR spectra.

In order to measure the SWR spectrum as well, the NC films of the Ni–Fe–C system were annealed for 1 h at $T_0 = 150$, 350, and 500°C under ultrahigh vacuum conditions. This treatment resulted in the transformation of the ($Ni_{80}Fe_{20}$)–C and ($Ni_{65}Fe_{35}$)–C supersaturated solid solutions (CSD size, ~4 nm) into ordered
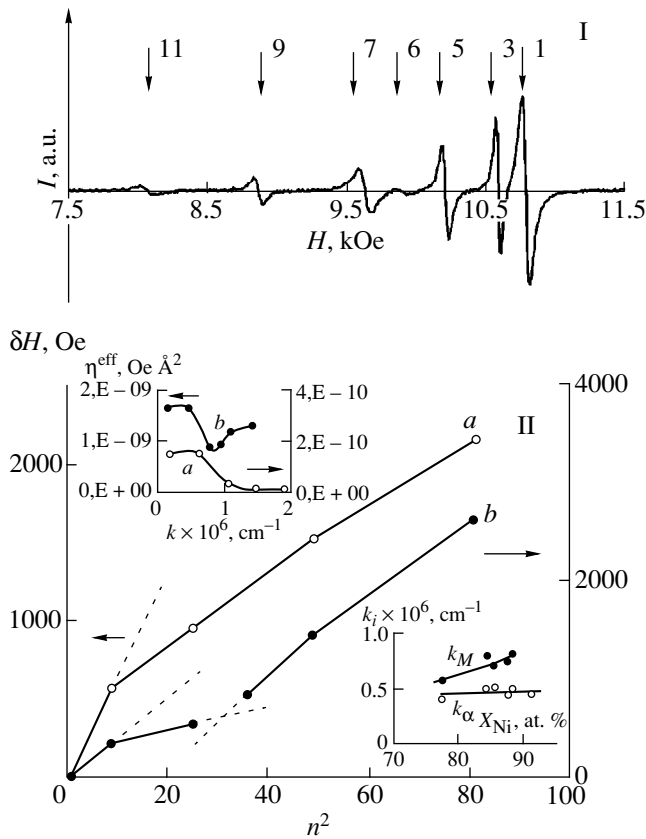
Fig. 2. SWR data for nanocrystalline Ni–Fe–P alloys: (I) a typical SWR spectrum of a film with the thickness $d = 200$ nm; (II) Experimental plots of the resonance field difference δH versus square mode number n^2 for the samples of (*a*) $(Ni_{0.91}Fe_{0.9})_{98}P_2$, $d = 150$ nm and (*b*) $(Ni_{0.88}Fe_{0.12})_{98}P_2$, $d = 190$ nm. The top inset shows the plots of effective exchange stiffness η^{eff} versus wavevector for the same films. The bottom inset shows the plots of wavevectors versus alloy composition for inflection points of the (open circles) "exchange" k_α and (black circles) "magnetization" k_M type.

solid solutions of the hcp Ni_3C and orthorhombic Fe_3C types, respectively, followed by decomposition into $Ni_{80}Fe_{20}$ and $Ni_{65}Fe_{35}$ nanocrystalline alloys with an fcc lattice ($a = 3.55–3.56$ Å), a CSD size of ~40 nm, an exchange constant $A \sim 0.8 \times 10^{-6}$ erg/cm, and a magnetization of $M^{eff} = 860$ and 1155 G, respectively. The films of both annealed alloys exhibited SWR signals (Fig. 1, I) containing 6–7 peaks. An analysis of these spectra showed that the samples also provide for the nearly ideal (Kittel) conditions of the surface spin pinning: intensities of the odd SWR peaks significantly by more than one order of magnitude exceed those of the neighboring even peaks.

Results and discussion. Figure 1 (II) shows the plots of δH versus n^2 determined from the SWR spectra of the $(Ni_{80}Fe_{20})$–C and $(Ni_{65}Fe_{35})$–C films with the thicknesses $d = 170$ and 120 nm, respectively. As can be

seen, both dispersion curves of $\delta H(n^2) \sim \omega(k^2)$ exhibit two special points (inflections) corresponding to the wavevectors k' and k''. The nanocrystalline $Ni_{80}Fe_{20}$ alloy is characterized by $k' = 0.52 \times 10^6$ cm^{-1} and $k'' = 0.94 \times 10^6$ cm^{-1}, while the nanocrystalline $Ni_{65}Fe_{35}$ alloy has $k' = 0.5 \times 10^6$ cm^{-1} and $k'' = 0.93 \times 10^6$ cm^{-1}. The inset in Fig. 1 (II) shows the experimental plots of $\eta^{eff}(k)$ for the same films, which indicate that the η^{eff} value is increasing at k' and decreasing at k''. This behavior, as well as the characteristic shape of the experimental plot of $\delta H(n^2) \sim \omega(k^2)$ is evidence that variation of the SW dispersion law observed in this system is determined by fluctuations of the magnetization M. This is additionally confirmed by a comparison of the k' and k'' values, which is close to the theoretically predicted ratio: $k'' = 2k'$ [7, 8].

By experimentally determining the value $k' \approx k*$, we may estimate the correlation radius for the magnetization fluctuations. Using the data of Fig. 1 (II), we obtain $r_M = 19$ nm for the films of the nanocrystalline $Ni_{80}Fe_{20}$ alloy and $r_M = 20$ nm for the nanocrystalline $Ni_{65}Fe_{35}$ alloy. These spatial fluctuations of the magnetization $M = 1/v_0 \sum_{v_0} \mu_{at}$ (see the standard definitions of μ_{at} and the volume v_0) can be explained only by the spatially inhomogeneous distribution of Ni and Fe atoms, whereby $X_{Fe}/X_{Ni} = f(r)$. Additional evidence is provided by estimates of the magnetic inhomogeneity manifested by the fluctuation intensity γ_M (see Eq. (2)). For the films of a nanocrystalline Fe–Ni alloy, this quantity was equal to ~0.4. We may use this value to estimate the possible deviations in the X_{Fe}/X_{Ni} atomic ratio from the average value, which yields variations of up to ~20 at. %.

Figure 2 (II) shows the $\delta H(n^2)$ plots for films of the Ni–Fe–P alloys. Here, the character of the dispersion law $\delta H(n^2) \sim \omega(k^2)$ depends on the alloy composition. For the $(Ni_{0.91}Fe_{0.09})_{98}P_2$ alloy (curve *a*), the behavior is as follows: $\eta^{eff}(k)$ decreases at $k = k*$ (see the top inset in Fig. 2, II) and the $\delta H(n^2)$ plot exhibits inflection at which the slope decreases. In terms of [7, 10], this inflection point is referred to as the "exchange type." Determination of the $n*$ value corresponding to this point led to $k_\alpha^* = 0.4 \times 10^6$ cm^{-1}. For the $(Ni_{0.88}Fe_{0.12})_{98}P_2$ alloy (curve *b*), there is an inflection point of the "exchange type" at $k_\alpha^* = 0.6 \times 10^6$ cm^{-1} and another inflection, at which the slope increases, while the $\eta^{eff}(k)$ plot accordingly changes from decrease to increase.

This behavior of the dispersion curve (and the corresponding variation of $\eta^{eff}(k)$ in the top inset in Fig. 2, II) is possible provided that the effects of α and M fluctuations add to one another, which implies that the wavevector $k' = 1.05 \times 10^6$ cm^{-1} is equivalent to the k_M^* value. Note that the $\omega(k^2)$ curve corresponding to fluc-

tuations of the magnetization M exhibits two features at $k = k_M$ and $2k_M$ (see Fig. 1 (II) and the previous section). In our case, the experimental dispersion curve $\delta H(n^2)$ for the films of nanocrystalline alloys of the Ni–Fe–P system occurs at $k < 2k_M$. For example, an estimate of the boundary wavevector k obtained from the last peak of the SWR spectrum of a $(Ni_{0.88}Fe_{0.12})_{98}P_2$ alloy (curve b) is $k_b = 1.8 \times 10^6 \, cm^{-1} < 2k_M = 2.1 \times 10^6 \, cm^{-1}$.

The bottom inset in Fig. 2 (II) shows the concentration dependence of the wavevectors k_α^* and k_M^* for films of the nanocrystalline Ni–Fe–P alloys. As can be seen, the k_M value linearly increases with X_{Ni}, while k_α is virtually constant. Note also that the character of the $\eta^{eff}(k)$ or $\delta H(n^2)$ curves exhibiting inflection points of the "magnetization type" depends on the second component concentration. Estimates of the fluctuation intensity γ_i (γ_α, γ_M) (see Eq. (2)) for Ni–Fe–P films of all compositions yield comparable values $\gamma_\alpha = 0.5$ and $\gamma_M = 0.45$. Upon calculating the corresponding boundary wavevectors, we may estimate the spatial fluctuations of the exchange constant and the magnetization. For the alloys studied, these fluctuations are characterized by $r_\alpha \approx 20$ and $r_M \approx 12$–17 nm.

The films of nanocrystalline Ni–Fe–P alloys represent a ternary system of the transition metal (Ni)–transition metal (Fe)–metalloid (P) type. We believe that the fluctuations of α in systems of this type are related to the inhomogeneous distribution of phosphorus in the film, whereas the fluctuations of magnetization are due to the inhomogeneous distribution of the X_{Fe}/X_{Ni} atomic ratio. In our opinion, this is confirmed by the character of variation of the k_α and k_M values as functions of X_{Fe}/X_{Ni} (see the bottom inset in Fig 2, II). Thus, the SWR spectra of the films of nanocrystalline Ni–Fe alloys with compositions in the permalloy range reveal the effects caused by the microphase separation (concentration inhomogeneity) of Ni and Fe with a spatial size of these fluctuations comparable with the coherent scattering domain size.

REFERENCES

1. A. I. Gusev, Usp. Fiz. Nauk **168** (1), 55 (1998) [Phys. Usp. **41**, 49 (1998)].
2. R. A. Andrievskiĭ and A. M. Glezer, Fiz. Met. Metalloved. **88**, 50 (1999); **89**, 91 (2000).
3. R. S. Iskhakov, S. V. Stolyar, D. E. Prokof'ev, et al., Pis'ma Zh. Éksp. Teor. Fiz. **70**, 727 (1999) [JETP Lett. **70**, 736 (1999)].
4. R. S. Iskhakov, S. V. Stolyar, L. A. Chekanova, et al., Pis'ma Zh. Éksp. Teor. Fiz. **72**, 457 (2000) [JETP Lett. **72**, 316 (2000)].
5. V. A. Teplov, V. P. Pilyugin, V. S. Gaviko, et al., Fiz. Met. Metalloved. **84** (5), 96 (1997).
6. C. E. Rodríguez Torres, F. N. Sánchez, and L. A. Mendoza Zeilis, Phys. Rev. B **51**, 12142 (1995).
7. V. A. Ignatchenko and R. S. Iskhakov, Zh. Éksp. Teor. Fiz. **75** (4), 1438 (1978) [Sov. Phys. JETP **48**, 726 (1978)]; R. S. Iskhakov, L. A. Chekanova, S. Ya. Kiparisov, et al., Preprint No. 238F, AN SSSR, Sib. Otd., Inst. Fiz. im. L.V. Kirenskogo (Kirenskiĭ Institute of Physics, Siberian Division, USSR Academy of Sciences, Krasnoyarsk, 1984).
8. M. V. Medvedev, Fiz. Met. Metalloved. **67** (5), 876 (1989).
9. R. S. Iskhakov, M. M. Brushtunov, A. G. Narmonev, and I. A. Turpanov, Fiz. Met. Metalloved. **79** (5), 122 (1995).
10. V. A. Ignatchenko, R. S. Iskhakov, L. A. Chekanova, and N. S. Chistyakov, Zh. Éksp. Teor. Fiz. **75** (2), 653 (1978) [Sov. Phys. JETP **48**, 328 (1978)].
11. L. J. Maksimowicz and R. Zuberek, J. Magn. Magn. Mater. **58**, 303 (1986).
12. R. S. Iskhakov, M. M. Brushtunov, and A. S. Chekanov, Fiz. Tverd. Tela (Leningrad) **29** (9), 1214 (1987) [Sov. Phys. Solid State **29**, 1553 (1987)].
13. V. S. Zhigalov, G. I. Frolov, L. I. Kveglis, et al., Fiz. Tverd. Tela (St. Petersburg) **40**, 2074 (1998) [Phys. Solid State **40**, 1878 (1998)].
14. A. A. Novakova, E. A. Gan'schina, T. Yu. Kiseleva, et al., in *Abstracts of the Moscow International Symposium on Magnetism, Moscow, 1999,* p. 259.

Translated by P. Pozdeev

Stochastic Instability of the Magnetostatic Surface Wave Trajectories in a Ferrite Film Magnetized by a Modulated Field with a Banklike Profile

V. I. Zubkov and V. I. Shcheglov

Fryazino Branch, Institute of Radio Engineering and Electronics, Russian Academy of Sciences,
Fryazino, Moscow oblast, Russia

Received October 27, 2000

Abstract—We report on the previously unstudied stochastic process arising when a magnetostatic surface wave (MSSW) propagates in a ferrite film magnetized by a modulated periodic inhomogeneous field with a banklike profile. The shape of the MSSW trajectories and the phase portrait of the stochastic process were established. It is shown that the MSSW trajectory becomes unstable and terminates when the MSSW propagation angle exceeds the cutoff angle. © *2001 MAIK "Nauka/Interperiodica".*

In connection with the development of new systems for the analog data processing [1], it is important to study the development of magnetostatic surface wave (MSSW) in periodically varying magnetic fields [2–6], in particular, in the fields described by the periodic functions of coordinates [5, 6]. At the same time, there is increasing interest among physicists in the study of processes exhibiting stochastic properties [7]. An example is offered by the chaotic oscillations of a deterministic system excited by a periodic action leading to variation of the system parameters in time. However, such processes must also be possible when the system parameters vary as functions of the spatial coordinates. Below we will demonstrate this possibility by presenting the results of investigation of the stochastic behavior of a MSSW propagating in a ferrite film magnetized by an inhomogeneous field with a banklike profile, the characteristics of which vary periodically in space. The principal possibility of implementing this process in experiment follows from the results reported in [5, 6].

As is known [8, 9], the MSSW trajectories in ferrite films magnetized by an inhomogeneous field with a banklike profile represent a spatial oscillatory process relative to a coordinate parallel to the bank axis. Let the coordinate plane $0yz$ coincide with the film plane, and let the $0x$ axis be perpendicular to this plane. Consider an MSSW with a frequency $\omega = 2\pi f$, the wavevector $\mathbf{k}$ and the group velocity $\mathbf{v}$ of which make the angles φ and ψ, respectively, with the $0y$ axis. The magnetostatic waves propagate in the ferrite film plane inside a channel along the $0y$ axis, their trajectories being close to sinusoidal sawtoothlike curves [8, 9] provided that the φ value at the excitation point φ_0 is smaller than the cutoff angle φ_c. Let us study transformation of the MSSW

trajectories caused by a periodic action modulating the magnetizing field with a banklike profile.

In the absence of modulation, the field H_g along the $0z$ axis is given by the formula

$$H_g = 4\pi M_0[T - F(z - S)^2], \qquad (1)$$

where M_0 is the saturation magnetization of the ferrite film; T, F, and S are the banklike field profile parameters describing the bank height, slope, and position on the $0z$ axis.

Now let the field be modulated by the law

$$R = R_0 + R_m = R_0 + R_{m0}\sin(2\pi R_r y), \qquad (2)$$

where $R = T$, F, or S; R_0 is a constant; R_m is a variable component of the parameter; R_{m0} is the modulation amplitude; and R_r is the modulation frequency. The MSSWs propagating in the field H_g modulated in such a manner experience a periodic action in various parts of their trajectories. As a result, the MSSW trajectory loses its stable sinusoidal character and acquires instability, which is manifested by chaotic jumps of the wave amplitude, frequency, and phase. If the φ angle upon a phase jump exceeds the cutoff angle, the trajectory terminates. The greater the modulation amplitude, the more pronounced the stochasticity manifestations are.

Let us consider, for example, an MSSW trajectory $z(y)$ in the magnetic field H_g with a banklike profile in which only the slope F is modulated according to the law described by formula (2) with $F_0 = 4$ cm^{-2}, $F_{m0} = 2$ cm^{-2}, $F_r = 3.57$ cm^{-1}, $T = 0.25$, and $S = 0$. We assume that the film is made of an yttrium iron garnet (YIG), a material that is frequently used in experiments with MSSWs [1, 5, 6, 8]. The YIG film thickness is taken
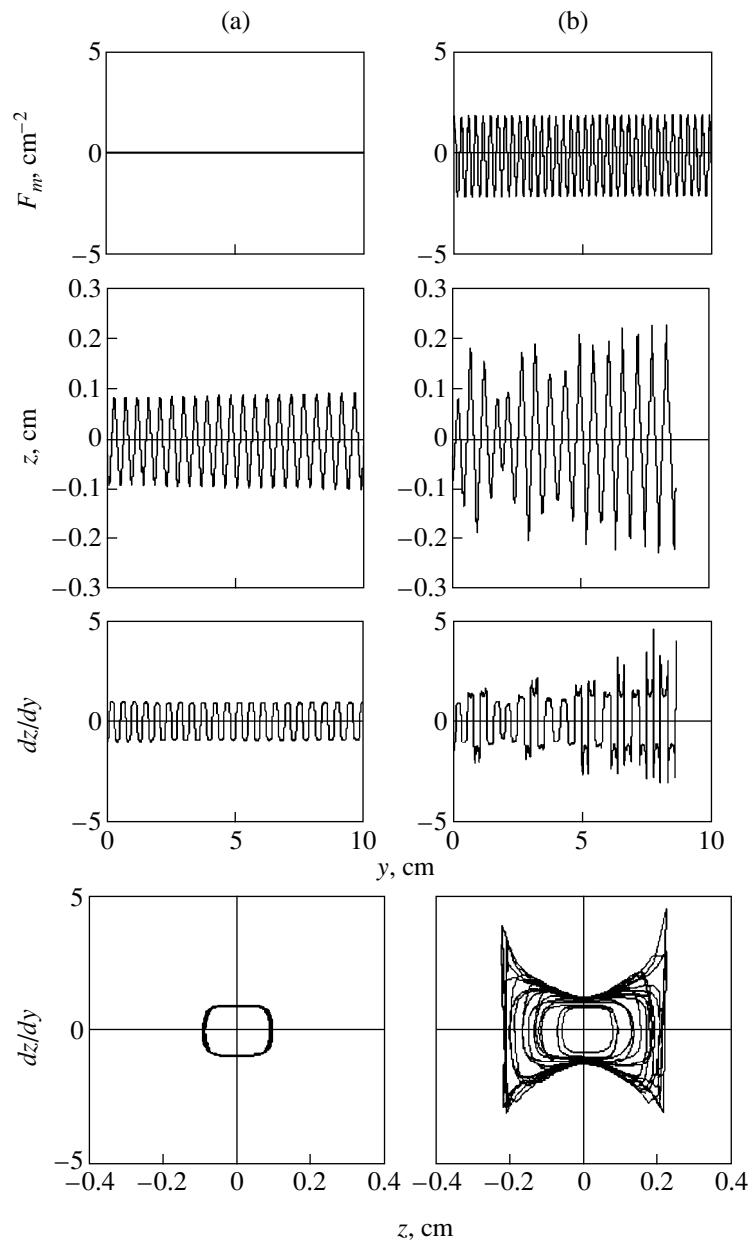
Fig. 1. MSSW characteristics, trajectories, and phase portraits (a) without and (b) with modulation of the banklike field profile parameters.

equal to 15 μm and the saturation magnetization, to $4\pi M_0 = 1750$ G. The MSSWs are excited at a point with the coordinates $y = 0$, $z = 0$ and are emitted at an angle of $\varphi_0 = 30°$.

Figure 1 shows the pattern of changes in the modulated field component F_m, the MSSW trajectory $z(y)$, and the derivative dz/dy, and the phase portraits of oscillations (i.e., the dz/dy versus z plots). In the absence of modulation (Fig. 1a), the MSSW trajectory and its derivative exhibit a strictly periodic nearly sinusoidal character, while the phase trajectory follows the same cycle. In the presence of modulation with respect to F (Fig. 1b), the amplitude of the MSSW trajectory

and its derivative exhibit chaotic jumps, whereas the phase trajectory changes in each cycle to yield a smeared phase portrait; moreover, the phase trajectory terminates at $y = 8.687$ cm.

Figure 2 shows a plot of the maximum MSSW trajectory length y_{max} for various modulation frequencies F_r. The y_{max} values are plotted versus the parameter $N_f = F_r/P_{m0}$, where $P_{m0} = 2.1$ cm^{-1} is the spatial frequency of the MSSW trajectories in the absence of modulation. The strongly uneven dependence of y_{max} on F_r reflects a spatial synchronism between the MSSW trajectories and the H_g field strength. The y_{max} exhibits a minimum every time the MSSW period is a
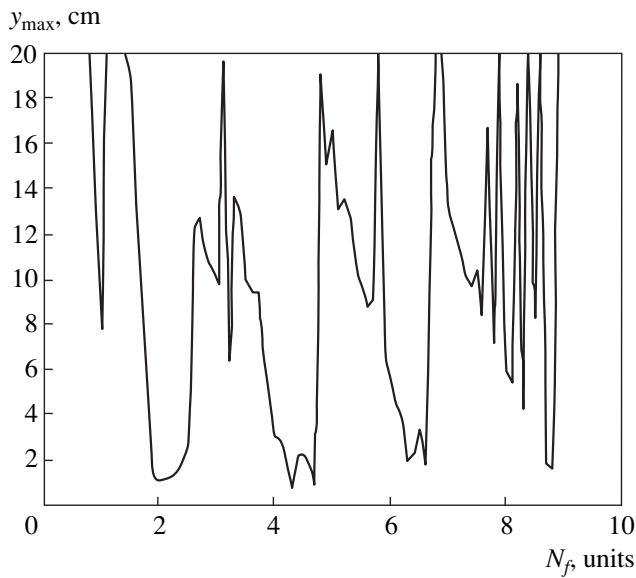
y_{max}, cm

Fig. 2. A plot of the MSSW trajectory length versus spatial modulation frequency.

multiple of the modulation period, the most pronounced minima corresponding to even integers (2, 4, 6, 8). For example, the MSSW trajectory length is 7.5 cm for $N_f = 1$, 1.5 cm for $N_f = 2$, 6.8 cm for $N_f = 3$, 1.2 cm for $N_f = 4$, 12.2 cm for $N_f = 5$, and 4 cm for $N_f = 6$. Between these points, the trajectory may be as

long as ≈ 20 cm, crossing the bank profile top only four–five times. For $N_f > 8$ (and up to $N_f = 15$), no minima in y_{max} were observed.

Similar patterns of stochastic instability in the MSSW trajectories were observed for modulation of the bank profile height or position.

REFERENCES

1. J. D. Adam, Proc. IEEE **76** (2), 159 (1988).
2. V. L. Preobrazhenskiĭ and Yu. K. Fetisov, Izv. Vyssh. Uchebn. Zaved., Fiz. **31** (11), 54 (1988).
3. V. Yu. Korovkin, Zh. Tekh. Fiz. **63** (9), 115 (1993) [Tech. Phys. **38**, 795 (1993)].
4. Yu. K. Fetisov, Zh. Tekh. Fiz. **64** (8), 76 (1994) [Tech. Phys. **39**, 787 (1994)].
5. A. V. Voronenko, S. V. Gerus, and V. D. Kharitonov, Izv. Vyssh. Uchebn. Zaved., Fiz. **31** (11), 76 (1988).
6. A. Yu. Annenkov, S. V. Gerus, and I. V. Sotnikov, Radiotekh. Élektron. (Moscow) **37** (8), 1371 (1992).
7. V. S. Anishchenko, A. B. Neĭman, F. Moss, and L. Schimansky-Geier, Usp. Fiz. Nauk **169** (1), 7 (1999).
8. V. I. Zubkov, É. G. Lokk, and V. I. Shcheglov, Radiotekh. Élektron. (Moscow) **35** (8), 1617 (1990).
9. A. V. Vashkovskiĭ, V. I. Zubkov, É. G. Lokk, and V. I. Shcheglov, Radiotekh. Élektron. (Moscow) **40** (2), 313 (1995).

Translated by P. Pozdeev